

Journal of Materials Chemistry B

Accepted Manuscript



This is an *Accepted Manuscript*, which has been through the Royal Society of Chemistry peer review process and has been accepted for publication.

Accepted Manuscripts are published online shortly after acceptance, before technical editing, formatting and proof reading. Using this free service, authors can make their results available to the community, in citable form, before we publish the edited article. We will replace this *Accepted Manuscript* with the edited and formatted *Advance Article* as soon as it is available.

You can find more information about *Accepted Manuscripts* in the [Information for Authors](#).

Please note that technical editing may introduce minor changes to the text and/or graphics, which may alter content. The journal's standard [Terms & Conditions](#) and the [Ethical guidelines](#) still apply. In no event shall the Royal Society of Chemistry be held responsible for any errors or omissions in this *Accepted Manuscript* or any consequences arising from the use of any information it contains.

Nanostructured Magnetic Nanocomposites as MRI Contrast Agents

Cite this: DOI: 10.1039/x0xx00000x

Erwin Peng,^{*a} Fenghe Wang,^a and Jun Min Xue^{*a}

Received 00th January 2012,
Accepted 00th January 2012

DOI: 10.1039/x0xx00000x

www.rsc.org/

Magnetic resonance imaging (MRI) has become an integral part of modern clinical imaging due to its non-invasiveness and versatility in providing tissue and organ images with high spatial resolution. With the current MRI advancement, MRI imaging probe with suitable biocompatibility, good colloidal stability, enhanced relaxometric properties and advanced functionalities are highly demanded. As such, MRI contrast agents (CAs) have been an extensive research and development area. In the recent years, different inorganic-based nanoprobe comprising of inorganic magnetic nanoparticles (MNPs) with organic functional coating have been engineered to obtain suitable contrast enhancement effect. For biomedical application, the organic functional coating is critical to improve the colloidal stability and biocompatibility. Simultaneously, it also provides building block for generating higher dimensional secondary structure. In this review, the combinatorial design approach by self-assembling pre-formed hydrophobic inorganic MNPs core (from non-polar thermolysis synthesis) into various functional organic coating (*e.g.* ligands, amphiphilic polymers and graphene oxide) to form water soluble nanocomposites will be discussed. The resultant magnetic ensembles were classified based on its dimensionality, namely 0-D, 1-D, 2-D and 3-D structures. This classification provides further insight into their subsequent potential use as MRI CA. A special attention will be dedicated on the correlation between the spatial distribution and its associated MRI applications, which include (i) coating optimization-induced MR relaxivity enhancement, (ii) aggregation-induced MR relaxivity enhancement, (iii) off-resonance saturation imaging (ORS), (iv) magnetically-induced off-resonance imaging (ORI), (v) dual-modalities MR imaging and (vi) multifunctional nanoprobe.

1. Introduction

Cancer as one of the most-feared diseases steadily evolved over time and was hardly resolved due to the complexity in the diagnostic and therapeutic approaches. For an effective treatment, an accurate molecular imaging during cancer preclinical stages as well as precise real-time monitoring during clinical state, are highly demanded before therapeutic techniques can be applied. To address this issue, the development of functional molecular imaging techniques in the past few decades has put forward major improvement over the effective clinical diagnostic. The prevalent state of the art in emerging molecular diagnostic imaging techniques include conventional x-ray radiographs, ultrasonography, positron emission tomography (PET), computed x-ray tomography (CT), single photon emission computed tomography (SPECT), magnetic resonance imaging (MRI) have been assisting clinicians to diagnose various types of injuries and diseases with high accuracy¹⁻⁹. Each molecular imaging technique relies on distinct contrast generation mechanism, and thus different CA is required for each imaging technique in order to enhance the detection resolution and capabilities. As x-ray radiography, PET, CT and SPECT scans involve ionizing radiation, MRI is

typically preferred due to its (i) non-invasiveness, (ii) high magnetic field penetration depth to human body without significant attenuation, (iii) real-time 3D tomographic image acquisition capabilities, (iv) good anatomical contrast differentiation and (v) the use of non-ionizing CAs.

To this end, MRI diagnostic platform allows real-time human tissues and organs visualization to achieve better medical diagnosis, especially in cancers-related, cardiovascular, liver and neurodegenerative diseases. In terms of detection, MRI offers tissue differentiation to identify malignant cells, ranging from breast cancer¹⁰, prostate cancer¹¹ to brain tumors and plaques of multiple sclerosis¹². In addition, whole-body MRI is also clinically safe for detecting metastatic tumor. Besides that, MRI is also useful in visualizing diseases associated with central nervous system such as Alzheimer as well as cardiovascular-related problems such as human atherosclerotic plaque, myocardial injuries and coronary artery disease¹³⁻¹⁶. Because of its ability to produce sophisticated 3D tomographic images of virtually all internal body structures, MRI is also useful to diagnose musculoskeletal-related diseases, *e.g.* arthritis and fractures^{17,18}.

In general, MRI is a non-invasive imaging technique that involves externally applied strong magnetic field,

radiofrequency (RF) electromagnetic pulses and free-induction decay to detect signals from the spatially localized magnetic nuclei in human tissues and organs. As hydrogen protons (^1H) are abundant in water and fat molecules, it is widely utilized for MR imaging. MRI becomes very useful to image the human body and biological tissues that are mainly comprised of water and fat molecules. Basic contrast can be obtained from the local water content differences as well as the localized differences in the water proton intrinsic relaxation times. However, by relying on such non-informative image, detection and diagnosis are often limited and inaccurate. In order to enhance MRI diagnostic sensitivity and detection capabilities, supplementary exogenous substance known as MRI CA is introduced. By selectively enhancing water proton relaxation times at the site of interest, precise discrimination of similar close tissue types can be realized. Currently, there are two types of commercially available MRI CAs: (i) negative T_2 and (ii) positive T_1 CAs¹⁹. As MRI CAs play a vital role in MR imaging, the exploration for improved MRI CAs for more accurate diagnostic imaging has propelled the advancement in the biomedical science research. Recently, there has been remarkable progress in the functional inorganic MNPs development for biomedicine applications, particularly in the field of diseases diagnosis and therapy. These MNPs ranging from 1–100 nm, can be either paramagnetic, superparamagnetic (SPM) or even ferromagnetic in behaviors that are capable of shortening bulk water protons relaxation times. Thus, inorganic-based MNPs are highly attractive as MRI CAs^{20, 21}. Besides as MRI imaging probes, over the last several years, MNPs have been extensively explored for other nanomedicine applications due to its unique magnetic behaviors, *e.g.* for (i) controlled drug delivery^{22–25}, (ii) magnetofection^{26, 27}, (iii) bio-separation^{28–30}, (iv) magnetic fluidic hyperthermia (MFH)³¹ and (v) cellular fate control agent^{32–34}. These applications enabled inorganic MNPs not only to be used as MRI CAs, but also potentially as theranostic (diagnostic and therapeutic) agents³⁵.

To this end, non-hydrolytic classical thermal decomposition synthesis is superior as compared to any other synthetic method (*e.g.* co-precipitation, hydrothermal, solvothermal, polyol method) in fabricating various inorganic MNPs with high precision control, in term of size, shape and monodispersity^{36, 37}. As the resultant MNPs are mostly hydrophobic in nature and not suitable for biomedical applications due to its potential toxicity, post-synthetic coupling of inorganic nanomaterials with functional organic materials becomes critical and inevitable in order to impart hydrophilicity and improve biocompatibility. The separation of MNPs synthesis and the post-synthetic self-assembly coupling with functional organic coatings process gives rise to higher degree of freedom that allows low-cost formation of higher-dimensional assemblies in a controllable manner. In this article, several significant non-covalent strategies to assemble MNPs into functional organic coating to yield higher-dimensional functional magnetic nanocomposites will be elaborated. Based on its dimensionality, MNPs assemblies can be classified into four categories, namely: (i) 0-D (*i.e.* individually coated MNPs), (ii) 1-D (*e.g.* rod-like or chain-like MNPs arrangement), (iii) 2-D (*e.g.* sheet-like MNPs arrangement) and lastly (iv) 3-D assemblies (*e.g.* MNPs-containing micelles and vesicles).

The combinatorial relationships between the superstructure forming organic materials (*e.g.* amphiphilic polymeric materials, graphene oxide, etc) with hydrophobic MNPs are able to produce magnetic nanocomposites with unique coating- and size-dependent properties that can be very useful in MRI

CAs application. Several structure-induced MRI functionalities will be discussed. In 0-D assemblies, suitable functional coating which optimized water diffusions helped to improve MRI relaxivities³⁸. In higher-dimensional assemblies, aggregation-induced MRI relaxivity enhancements were observed^{39–41}. In both cases, the enhanced relaxivity implicated that less amount of MRI CA will be required to generate meaningful contrast. The 3-D aggregates of MNPs within polymeric matrix were also useful for (i) off-resonance saturation⁴² and (ii) magnetically-induced off-resonance imaging⁴³ in which the background noise can be suppressed, allowing a more accurate imaging with high signal-to-noise ratio. The self-assembly into higher-dimensional structure also potential for the development of “smart” multifunctional nanocomposites which allowed the combination of various imaging modalities (*e.g.* dual MRI T_1 and T_2 imaging)⁴⁴ as well as the theranostic applications⁴⁵.

2. Nanoparticulate-based CAs Development

Up to date, the MRI CAs development has its research focus entirely shifted towards the use of magnetic nanocomposites. Various artificially engineered magnetic nanoprobe have been proposed so far²¹. In general, nano-sized MRI CAs refers to the use of inorganic MNPs of comparable or even smaller size (10–100 nm) than cell and tissue structures (10–100 μm), protein (5–50 μm), and gene (2 nm wide and 10–100 nm long) in human body. As such, inorganic MNPs can be engineered with various biomolecules to promote interaction with various biological entities of interest. Higher nanoprobe penetrability to human body vascular system and tissue pores is possible due to its comparable size. The nano-size characteristic also promotes enhanced permeability and retention (EPR) effect with suppressed reticuloendothelial system (RES) uptake which results in prolonged circulation half-lives inside human body. Based on these factors, inorganic nanoparticulate system becomes critical in MRI CAs development.

A. Magnetic Nanoparticles Synthesis Techniques

Currently, bottom-up chemical-based synthesis methods have been widely employed to prepare inorganic nanoparticles for biomedical applications. Using this approach, small atoms and molecules were assembled chemically through nucleation and growth processes to form larger aggregates and finally nanoparticles. The bottom-up techniques can be further divided based on the solvent nature, into hydrolytic and non-hydrolytic synthetic routes. Hydrolytic synthetic routes were typically carried out in aqueous solvent and mostly based on the hydrolysis of metal ions precursors. These include co-precipitation^{19, 46–55}, hydrothermal^{56–64} and water-in-oil micro-emulsion^{65–67} techniques. The use of aqueous solvent enabled cost-effective hydrolytic techniques to be employed for directly preparing water-soluble magnetic nanoparticles. However, because of the synthesis limitation (*e.g.* limited size and morphology control as well as poor crystallinity), hydrolytic techniques were discouraged for preparing sample for biomedicine application⁶⁸.

To address the challenge in producing inorganic MNPs with very narrow size distributions, non-hydrolytic synthetic routes in organic solvents such as thermal decomposition (or thermolysis) of organometallic precursors in non-polar^{69–77} and polar solvents^{78–82} as well as solvothermal reaction^{83–90} were established. Among these synthetic techniques, thermolysis of metal-organic precursors in various high boiling-point non-polar solvent with the presence of hydrophobic surface capping

agents was the most suitable method for preparing uniform inorganic MNPs with high quality and excellent physical properties^{69-74,75-77, 91-95}. Through this method, a wide range of MNPs with different size, size distribution, morphology and compositional tuning (as illustrated in **Fig. 1**) can be prepared simply by changing the metal-precursors, surfactants, heating temperature, heating duration as well as the precursors to surfactant/solvent ratio. For example, extreme size control up to 1 nm resolution of monodisperse iron oxide MNPs have been reported previously by Park *et al.*⁹⁶.

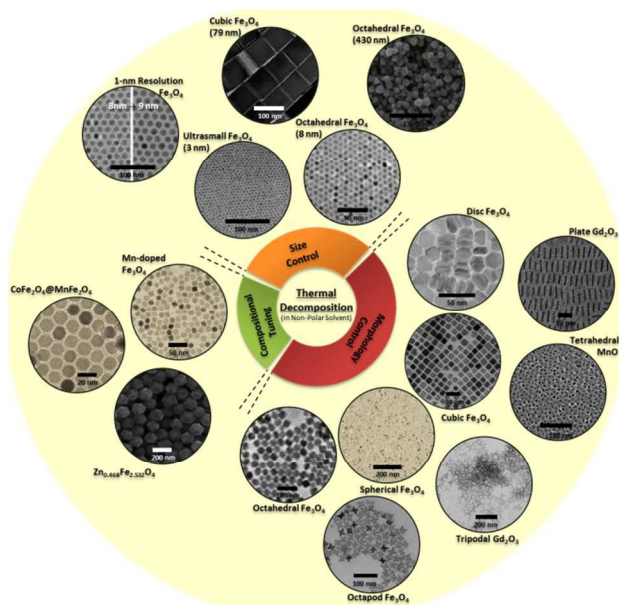


Fig. 1 Thermolysis Synthesis. TEM images of MNPs illustrating the size, shape and compositional control during thermolysis synthesis. [Adapted by permission from Macmillan Publishers Ltd: Nature Materials, Ref⁷⁵, Copyright (2004)]. [Adapted by permission from Macmillan Publishers Ltd: Nature Communications, Ref⁹⁷, Copyright (2013)]. [Adapted by permission from Macmillan Publishers Ltd: Nature Nanotechnology, Ref³¹, Copyright (2011)]. [Adapted with permission from Ref^{74, 98-103}. Copyright (2004), (2008), (2010), (2011) and (2013) American Chemical Society.]. [Adapted from Ref^{104, 105} with permission from the Royal Society of Chemistry.]. [Adapted from Ref^{96, 106}. Copyright (2005) and (2012) Wiley-VCH.]

Various shapes including spherical, cubic, octahedral and disc-like structures have been synthesized previously^{74, 99, 100, 103, 107-114}. Different types of MNPs such as MFe_2O_4 (where $M = Mn, Fe, Co, Ni$)^{21, 115, 116}, $SmCO_5$ ^{117, 118}, $FePt$ ^{119, 120}, Ln_2O_3 (where $Ln = Eu, Gd, Dy, Ho, Er$)^{98, 102, 121-126}, MnO/Mn_3O_4 ^{106, 127-138}, $FePd$ ¹³⁹, $CoPt$ ^{140, 141}, Fe_5C_2 ¹⁴²⁻¹⁴⁴, Mn-doped ZnS ¹⁴⁵ nanoparticles as well as hybrid dumbbell structures¹⁴⁶, trimer structures¹⁴⁷, flower-like structures¹⁴⁸ and core-shell structures^{31, 149-151} have been reported so far for either MRI T_1 - or T_2 -weighted imaging application. Other materials such as magnetic/up-conversion rare-earth fluorides nanoparticles ($NaLnF_4$) have been also developed for both MRI T_1 - or T_2 -weighted imaging application, depending on its luminescent lanthanide dopants (*e.g.* Eu, Tb, Er, Tm and Yb) and its structural configuration¹⁵²⁻¹⁶⁰. More recently, dysprosium-based (Dy^{3+}) MNPs such as Dy_2O_3 , $NaLnF_4:Dy$ and $NaDyF_4$ were also reported to be suitable for high field MR imaging due to its high magnetic moments and large spin-orbit interaction^{161-165, 166}. Extremely ultra-small (<4nm) MNPs which possessed high surface-to-volume ratio with large unpaired electrons and large surface spin disorders (such as

extremely small Fe_3O_4 , Gd_2O_3 and $NaGdF_4$) were also of interest, especially for MRI T_1 -weighted imaging application^{101, 155, 167-169}. As the thermolysis route were capable of fabricating various types of inorganic nanoparticles (apart from magnetic nanoparticles), the previous list mentioned was far from exhaustive. In general, the key ideas to obtain high degree of size, shape and uniformity controls during the thermolysis included: (i) successful nucleation growth process separation, as proposed by LaMer^{87, 138, 143, 144}, (ii) controlled heating rate, (iii) surfactant nature and its molar ratio against the organometallic precursors as well as (iv) reaction dwelling temperatures^{170-176 138}.

B. The Need for Coupling with Organic Functional Coating

For various advanced biomedicine applications, inclusive of MRI, the synthesized inorganic MNPs have to fulfil the following requirements: (i) high quality and monodisperse, (ii) water soluble with excellent colloidal and chemical stability, (iii) suitable and tunable hydrodynamic size, (iv) low toxicity and good biocompatibility and (v) bio-functionalizable. As the intrinsic properties of inorganic MNPs was highly dependent on the physical and chemical properties of the MNPs itself such as size, shape, surface-to-volume ratio, crystallinity and surface functionalities, suitable synthesis method with high controlling degree became very critical. To achieve this, thermolysis in non-polar solvent was still preferred to fabricate a wide-range of inorganic MNPs due to the excellent physical properties and high crystallinity as well as tunable size, size distribution and morphology of the resultant inorganic MNPs that were not reproducible from any other techniques. Despite such reliability, hydrophobic long-carbon chain surface capping agent such as oleic acid and/or oleylamine was usually employed to ensure size and shape uniformity. This capping agent protective monolayer was strongly bonded to the MNPs surfaces, causing the MNPs to exhibit hydrophobic characteristic which limited its biomedicine application¹⁷⁷⁻¹⁸⁰. Thus, extensive efforts have been dedicated to develop appropriate post-synthetic chemical surface modification to improve the surface functional coating, with the aim to impart water solubility and transfer these hydrophobic MNPs from the hydrophobic environment to the aqueous solvents

Since aqueous dispersion and biocompatibility are the essential prerequisites for MNPs usage in biomedicine application, organic carbon-based functional coating is more suitable as compared to inorganic coatings (*e.g.* silica or noble metal gold/silver coating) due to its close nature to various organic biomolecules^{181, 182}. In this article, functional organic coating refers to wide range of carbon-based materials such as small molecules, amphiphilic surfactant, amphiphilic brush and block copolymers, 2-D graphene oxide (GO) materials and so on. These functional surface coatings can provide aqueous stability in various biological environment and fluids (*e.g.* cellular medium, blood and serum, acidic gastric liquid) through (i) reduction of surface energy of the system, (ii) steric hindrance that creates barrier to prevent non-specific agglomeration and/or (iii) electrostatic repulsion (van der Waals) force that isolates each individual nanocomposites. At the same time, it also provides anchoring point for further bio-conjugation through the availability of various functional groups, inclusive of carboxylic acid ($-COOH$), hydroxyls ($-OH$), carbonyls ($-C=O$), epoxy ($C-O-C$), amine ($-NH_2$), sulfhydryl ($-SH$) or amine ($-NH_2$) groups. Moreover, as the resultant nanocomposites shall be low in toxicity and possess good biocompatibility, the presence of proper surface coating

helps to contain and prevent the leakage of toxic metal ions to biological fluids in the event of inorganic MNPs dissolution. Therefore it minimizes the possible adverse direct-interaction of inorganic MNPs with human cells or tissues. Lastly, during the post-synthetic surface modification, it is important to assert extra attention in controlling the resultant water-dispersible magnetic nanocomposites' hydrodynamic size. The hydrodynamic size mainly influences the passive targeting through the EPR effect of the tumor vasculature as well as the nanoparticles clearance from the body system through the RES organs system^{72, 183}. Due to its comparable size with the kidney's glomerular capillary wall pore size, typical small MNPs of less than 6 nm are excreted through renal clearance^{184, 185}. Beside the size threshold requirement, different MNPs surface coating chemistry (*i.e.* surface charges) and shape also led to different bio-distribution and clearance mechanisms¹⁸⁶. For instance, positively charged MNPs with 6–8 nm hydrodynamic size was able to pass through glomerular filtration barrier due to the charge interaction with the negatively charged glomerular capillary wall¹⁸⁷. Meanwhile, larger MNPs of 30–150 nm in hydrodynamic size may accumulate in bone marrow, heart, kidney and stomach¹⁸⁸. Lastly, MNPs within this range as well as above 150 nm to microparticles size were likely to mount up in liver and spleen, followed by the clearance through RES macrophages^{185, 189–192}. In short, the nanocomposites should not interact with any of biological proteins and ionic charges that may induce uncontrolled aggregation and lead to abrupt hydrodynamic size increase. From the aforementioned factors, proper selection of functional organic coating becomes inseparable from the fabrication of suitable inorganic MNPs for biomedical applications.

C. Suitable Inorganic Nanoparticulate MRI CAs

In general, MRI CA enhances the natural contrast of MRI signal intensity (signal-to-noise ratio) which enables differentiation of two adjoining tissues as well as human vessels and organs. Based on its contrast mechanisms, MRI CAs can be categorized into T_1 and T_2 CAs. The typical contrast mechanisms usually resulted from the interaction between the introduced MRI CA with the surrounding available water protons. Effectively, the MRI CAs should significantly reduce either the longitudinal (T_1) or transverse (T_2) relaxation times of water protons at relatively minimum concentration. Usually, r_1 or r_2 ionic relaxivities, relaxation rate slope (s^{-1}) against the influencing ions concentration (in mM), were used to quantify the MRI CAs' efficiency.

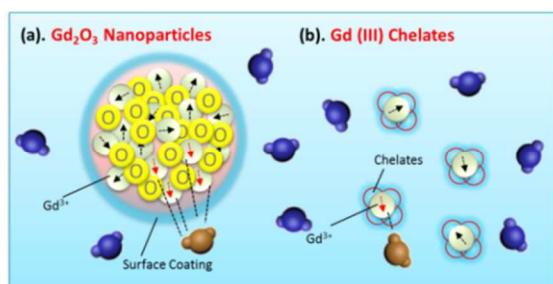


Fig. 2 Comparison between (a) Gd_2O_3 MNPs and Gd (III) chelates in terms of its interaction with water molecules. [Adapted with permission from Ref ⁷⁹. Copyright (2009) American Chemical Society.].

MRI T_1 CAs usually used paramagnetic agents with high r_1 while minimizing the magnetic anisotropy (low r_2)¹⁹³. To be an effective positive CAs, the resultant r_2/r_1 ratio has to be less than 10. The longitudinal relaxation of the water protons originated from the dipole-dipole interactions between the nuclear spins and the unpaired electron spins induces fluctuating local magnetic field. By far, various transition and lanthanide metal oxides nanoparticulate materials that possesses large number of unpaired electrons in the *d*- and *f*-orbital such as Gd-based or Mn-based oxide materials are suitable as T_1 MRI CAs due to its chemical stability as compared to metal-chelates (illustrated in **Fig. 2**)⁷. There are in total three different types of possible metal ions interaction with surrounding water protons: (i) inner-sphere (IS), (ii) outer-sphere (OS) and (iii) secondary-sphere (SS) relaxations. The IS relaxation originates from the dipolar interactions and the contact of water protons with the transition/lanthanide metal ions and the exchange of these water molecules with bulk water pool. According to the Solomon-Bloembergen-Morgan equation, the chemical exchange of the IS water molecules have to be fast in order to effectively propagate the relaxation to the bulk water¹⁹⁴. Moreover, the water molecules are also experiencing the paramagnetic influence as the water diffuses around in inhomogeneous fluctuating field created by the metal ions which contributes to the OS relaxation. Lastly, the SS contribution is contributed mainly by the relaxation of solvent molecules that are not directly bound within the inner-sphere but remained within the proximity of the paramagnetic influence for a relatively long period of time. As the magnetic field around the paramagnetic substances diminishes rapidly with the distance from the core metal-ions, several possible key-factors that affect the water proton relaxations mechanism have to be optimized in designing proper and suitable nanoparticulate MRI T_1 CAs. These includes improving residence time of bound water, core MNPs water accessibility, core MNPs separation distance with diffusing water molecules as well as water molecules mobility¹⁹⁵. Ideally, MNPs with high surface-to-volume ratio is required to expose more metal-ions on the MNPs surface to the surrounding water. However, due to the need for aqueous dispersion, surface coating is imparted, restricting the transfer of surface exchangeable protons and bulk water protons. Because of this, only OS and SS relaxation contributions are still taking place while the IS relaxation enhancement is greatly suppressed^{79, 159, 196}. Despite this drawback, the use of nanoparticulate MRI T_1 CAs implies that several metal ions can cooperatively participate in accelerating the longitudinal relaxation of water protons through the OS contribution (**Fig. 2a**). When chelates are used, the synergistic effect may diminish because of the substantial chelates separation distances (**Fig. 2b**). Overall, through a proper surface coating chemistry and optimization, enhanced MRI T_1 CAs that appropriately modulate the surrounding water protons exchange kinetics and interaction with the core MNPs surface can be attained.

For MRI T_2 CAs, superparamagnetic and ferrimagnetic MNPs have been under major scrutiny due to its high magnetic anisotropy that are capable of inducing strong magnetic susceptibility effect and inducing magnetic field inhomogeneity that accelerates de-phasing process of surrounding diffusing water protons^{35, 74, 197, 198}. To be an effective negative contrast agent, the r_2/r_1 ratio has to be over 10. SPM nanoparticles are particularly of interest because the magnetic alignment disappeared due to thermal random movement, which is beneficial to minimize adverse uncontrolled aggregation effect.

Several previously approved MRI T_2 CAs such as Feridex (r_2 of $98.3 \text{ mM}^{-1}\text{s}^{-1}$), Ferumoxtran (r_2 of $60.0 \text{ mM}^{-1}\text{s}^{-1}$) and Resovist (r_2 of $151.0 \text{ mM}^{-1}\text{s}^{-1}$) relied on the use of SPM nanomaterials and have been previously administered *in-vivo*, either during animal testing or clinical trials^{19, 199}. Unfortunately, due to the long term *in-vivo* safety concern, these MRI T_2 CAs have been withdrawn, except for the oral agent Lumirem/GastroMARK²⁰⁰.

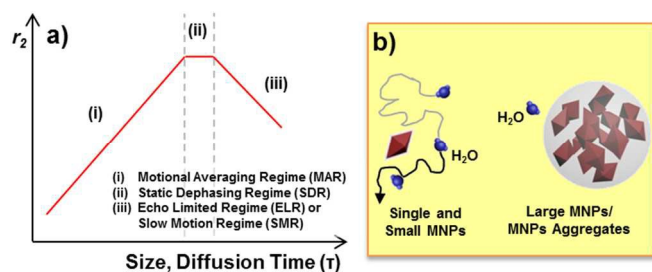


Fig. 3 (a) Size-dependence of MR relaxivity predicted by outer sphere relaxation theory. Three distinctive regimes: (i) MAR, (ii) SDR and (iii) ELR. (b) In MAR regime, fast water molecule diffusion experienced rapid-changing magnetic fields during relaxation. In SDR regime, water molecule experience negligible magnetic field fluctuations. [Adapted with permission from Ref⁴¹. Copyright (2012) American Chemical Society.].

Regardless of the MRI CAs materials, the T_2 -relaxation is primarily governed by the OS relaxation theory, in which the de-phasing of hydrogen protons diffusing into the periphery regime of the MRI CAs is influenced by the local magnetic flux. By assuming the Brownian diffusional motion of water is dominant, there are three distinct size-dependent behavioral regimes (**Fig. 3a**) based on the water protons diffusion, namely: (i) motional averaging regime (MAR), (ii) static dephasing regime (SDR) and (iii) slow motion regime (SMR)²⁰¹⁻²⁰³. In MAR, when the hydrodynamic size is sufficiently small, water molecules experienced fast changing magnetic fields as they diffuse rapidly around the CAs. Thus, the overall T_2 relaxation rate will be governed by the water molecular motions and the r_2 value increases with the CAs' hydrodynamic size. Approximately, the r_2 is proportional to the square of MNPs magnetic moment and diffusion characteristic time within MAR region. As the CAs' hydrodynamic size increases further, at certain aggregates size, water molecule will experience constant magnetic field during transverse relaxation. Within this SDR regime, the r_2 relaxivity value becomes independent of the aggregates size and water diffusion has minimal influence on the water protons relaxations (**Fig. 3b**)²⁰⁴. Maximum relaxivity is achieved and increasing aggregates size within this regime no longer translates into relaxation rates enhancement. As the aggregate size increases further, reaching ELR regime, only water molecules that are within core MNPs' close proximity are completely de-phased due to strong magnetic field, reducing the r_2 value. The OS relaxation theory dictates strong relationship between r_2 value with the core MNPs magnetic properties and interaction with the water protons. By properly engineering of the core MNPs magnetism through the control of size, shape and crystallinity, coupled with advanced surface coating to enhance water penetrability and retention, enhanced MRI T_2 CAs can be obtained.

3. Nanostructures Dimensional Classification

A. Importance of Building Blocks and Architecture

The necessity for hydrophobic MNPs phase transfer using organic functional coating results in a greater freedom to form higher-dimensional structures through MNPs assemblies. Moreover, the separation of the MNPs synthesis and assembly allows the abilities of custom-designing each individual entity separately. Although discrete inorganic MNPs with well-controlled size, shape and compositions can be readily obtained from the thermolysis in non-polar solvent, the MNPs assembly into a well-defined and controlled superstructures for practical biomedicine use is still a demanding task²⁰⁵. The bottom-up self-assembly of MNPs building blocks into more complex structural array have been gaining interest recently²⁰⁶. To achieve well controlled self-assembly and desired architecture, MNPs core have to be uniform in shape and monodisperse in size. Since magnetic nanomaterials synthesis techniques have been well established, current research effort focused on the MNPs assemblies' influence on the resultant physical properties. Similar to MNPs' physical properties (1–100nm) that differs significantly from the bulk material, the collective properties of MNPs ensembles can be different as compared to individual MNPs and bulk materials. Therefore, the hierarchical multi-dimensional MNPs assembly with controlled morphology and spatial distribution into higher ordered nanostructures is critical for designing new nanostructures for biomedical applications. Over recent years, the opportunity to form MNPs ensembles has been considered for MRI application and will be discussed in the last section of this article.

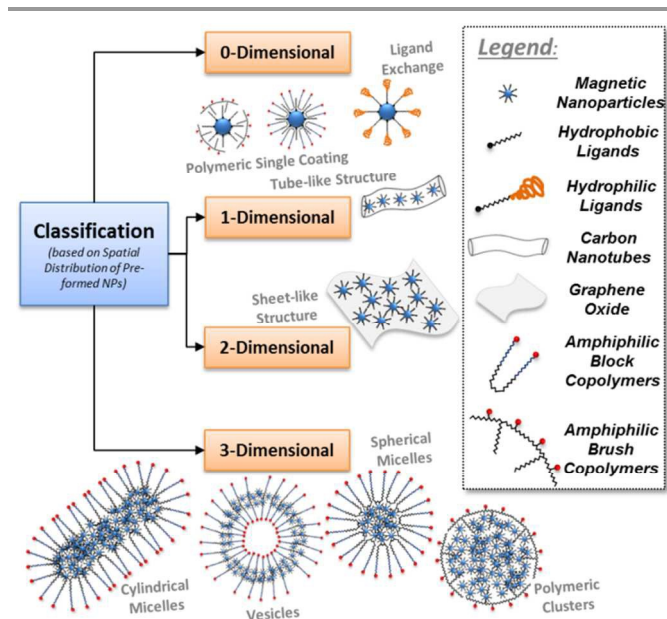


Fig. 4 Nanocomposites classification based on hydrophobic MNPs ensemble.

In this section, the overview of hydrophobic MNPs phase-transfer and assembly techniques using organic functional coating to generate water-dispersible magnetic nanocomposites of different morphology will be discussed. Based on the hydrophobic MNPs' spatial distribution of the within the functional coating, the overall assembly can be classified into four different categories: zero-dimensional (0-D), one-dimensional (1-D), two-dimensional (2-D) and three-dimensional (3-D) systems. In most cases, the non-covalent interactions simply allow higher freedom to modulate the MNPs into higher dimensional nanostructures with greater complexity without the need for complex chemical reactions. 0-

D structure simply refers to individually coated MNPs with organic materials; while higher dimensional structures simply refer to the MNPs collective encapsulation. Apart from the symmetrical 3-D assemblies, the 1-D and 2-D assemblies are highly asymmetric in shape that can be possibly achieved by selecting suitable functional organic host with asymmetric dimensions such as 1-D nanotubes or 2-D nanosheets.

B. Zero-dimensional Nanostructures

The 0-D nanostructures, in which hydrophobic MNPs are individually encased within functional organic coating, mimicked the original characteristic of monodisperse hydrophobic MNPs obtained from the thermolysis in non-polar solvent. The formation of 0-D nanostructures can be simply seen as an attempt to water-solubilize the hydrophobic MNPs through chemical surface modification and functionalization. The individual surface coating per MNPs is expected to provide suitable protections against harsh environmental condition as well as good colloidal stability required by many biomedical applications. Ideally, 0-D nanostructures can be represented by core-shell structure (see Fig. 4) with inner MNPs core and outer organic shells layer. To date, 0-D nanostructures was practically difficult to be achieved and certain degree of MNPs aggregation was often reported²⁰⁷. Proper experimental control is therefore required to achieve single coating process. In principle, the hydrophilic nanocomposites' hydrodynamic size has to be as close as possible to the original hydrophobic MNPs' hydrodynamic size in non-polar solvent. Several notable surface modification strategies to achieve the aforementioned 0-D architectural design have been summarized in Fig. 5, such as (i) ligand exchange, (ii) ligand modification, (iii) micelle formation and (iv) polymeric encapsulation.

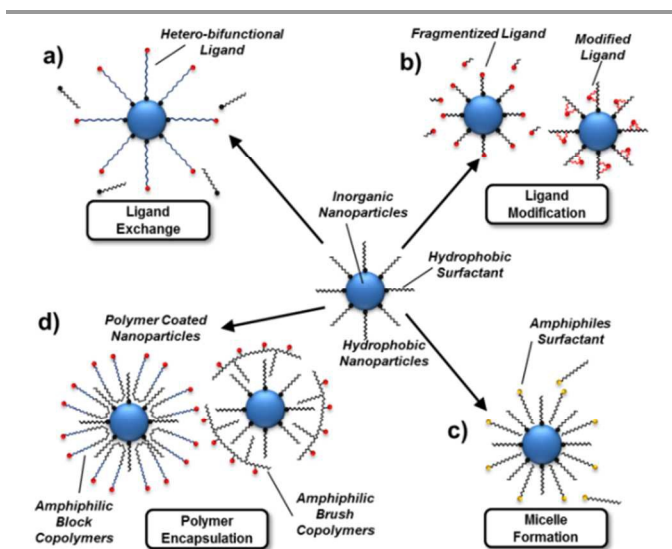


Fig. 5 Hydrophobic ligand-capped MNPs surface modification strategies: (a) ligand exchange, (b) ligand modification, (c) micelle formation and (d) polymer encapsulation.

Ligand Exchange

Ligand exchange is the simplest and most direct method that allowed the replacement of the original hydrophobic ligands (e.g. oleic acid or oleylamine) with another ligand bearing hydrophilic functional groups. To date, ligand exchange was commonly reported in the literatures to water-solubilize wide range of hydrophobic MNPs obtained from thermolysis process^{32, 91, 118, 208-212}. To enable successful ligand

exchange process, appropriate phase-transfer agents, usually short molecules ligands with at least one anchoring point that has high affinity towards the MNPs surface in one end to displace the existing hydrophobic ligands and suitable hydrophilicity in the other end to impart water-solubility, have to be carefully selected. The anchoring point towards MNPs can be in the form of mono-dentate, bi-dentate or multi-dentate. Unfortunately, specific hydrophilic ligands have to be selected for different types of inorganic MNPs. For typical metal-oxide surface (e.g. Fe, Mn, Gd), hydrophilic ligands with oxygen-containing functional groups that promoted binding towards metal-oxide surface were favored. Currently, there are few types of ligand exchange agents (Fig. 6b): (i) cationic surfactant, (ii) catechol and its derivatives, (iii) phosphonate-based, (iv) carboxyl-based and (v) silane-based ligands.

Cationic surfactants including tetramethylammonium hydroxide (TMAOH)²¹³ and nitrosonium tetrafluoroborate (NOBF₄)²¹⁴ have been reported to quickly displace the original alkenoic ligands from hydrophobic oxide-based MNPs surface. Inconveniently, the resultant hydrophilic MNPs were capped with negatively charged ions and thus not dispersible in any ionic solution due to the potential interaction with various positively charged metal ions in the solution. Such interaction normally caused MNPs agglomeration which compromised the overall MNPs colloidal stability in aqueous solvent. To resolve this, further surface modification with silica or polymeric coating was still needed after the ligand exchange process with cationic surfactants²¹³⁻²¹⁵. Alternatively, polyol-based ligands with multiple hydroxyl functional groups were capable of binding various transition metal ions and oxides. Within this category, catechol-based surfactant such as dopamine and its derivatives were relatively popular to water-solubilize metal-oxide MNPs^{91, 118, 210, 211, 216-219}. The two hydroxyl functional groups (1,2-benzenediol) were capable of coordinating with the metal oxide surface through M–O bonds formation while displacing the original hydrophobic ligands. Polyethylene glycol chain was commonly conjugated to the dopamine-based ligands either before or after ligand exchange process through multi-phase processes^{91, 217, 218}. Besides the conventional bidentate ligands, multidentate catechol- and PEG-derivatized oligomers (or OligoPEG-DOPA) was demonstrated to possess high affinity towards the iron oxide MNPs²¹⁶.

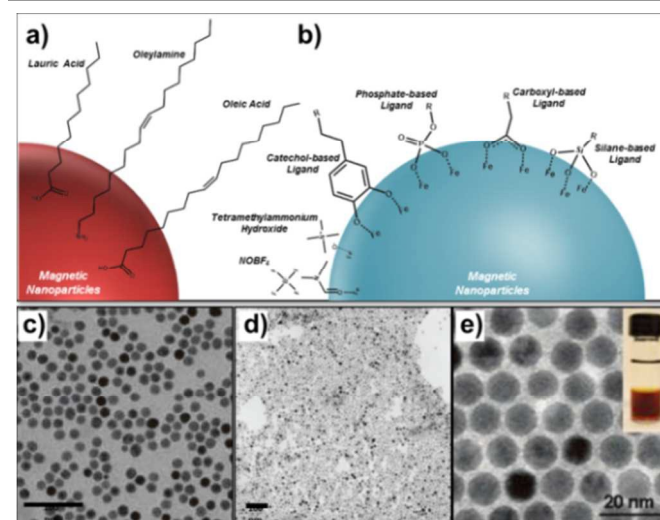


Fig. 6 Ligand Exchange. Stabilizing single hydrophobic MNPs (a) in aqueous solvent through ligand replacement process, in order to yield (b) water soluble

MNPs. TEM images of IONPs (c) stabilized by catechol-based ligand, (d) stabilized by DMSA and (e) capped with NOBF₄. [Reprinted with permission from Ref ^{214, 216}, Copyright (2010) and (2011) American Chemical Society.]. [Reprinted from Ref ⁷², with permission from Elsevier].

Hydrophilic ligands that carried single or multiple carboxylic acid (–COOH) groups also provided strong affinity towards the metal-oxide MNPs surface. Carboxyl-based ligands coordinated with the metal-oxides nanoparticles through M–O bonds and four-member chelating ring, similar to the original hydrophobic oleic acid ligand. One of the commonly used carboxyl-based ligands was dimercaptosuccinic acid (DMSA) ^{31, 32, 34, 72, 76, 103}. Bearing two carboxyl and two sulfhydryl groups, DMSA-coated MNPs may exhibit certain degree of agglomeration after the ligand-exchange process ⁷². To date, DMSA have been successfully used to water-solubilize hydrophobic MNPs of different size, shape and composition ^{21, 103}. Other carboxyl-based ligands such as carboxymethylated PVA ²¹³, polyaspartic acid ¹³⁶ and citric acid ²²⁰ have been similarly demonstrated for successful ligand-exchange process. In addition, a more stable hydroxamic-acid based ligands also served as a suitable replacement for the carboxyl-based ligands ²²¹. Several good examples on ligand exchange using catechol-based ligands, DMSA and NOBF₄ were given in **Figure 6c-e**.

Since phosphonate or R–PO(OH)₂ group was capable of forming strong binding with the metal oxide surface, organophosphorus-based ligands were valuable for ligand-exchange process. As a result of this binding, stable M–O–P phosphate-metal coordinative bonding was formed. In contrary to the typical bi-dentate coordination bonds of diols or carboxyl with metal-oxide surface, phosphoric acid groups can form either bi-dentate or tri-dentate M–O–P coordination bonds which provided stronger bridging geometry ⁷³. In addition, organosilanes-based ligands were also reported as phase-transfer by replacing the typical bidentate oleic acid anchoring on metal-oxide surface with silane anchoring group ^{208, 222, 223}. Unlike organophosphorus-based ligands, organosilane-based ligands were prone to homocondensation which resulted in Si–O–Si bridges network. As a result, MNPs agglomeration can be resulted, impairing the MNPs colloidal stability.

Despite its simplicity, surface sensitive ligand exchange technique often complicated the phase-transfer process and prevented one type of ligand to be widely applicable to different MNPs. Thus, different ligand chemistries were required for various MNPs in order to promote strong affinity of the anchoring agent towards the MNPs surface. Moreover, the binding of the newly exchanged ligand to the MNPs surface was normally weaker and more labile than the original hydrophobic surfactant to the MNPs surface, leading to potential uncontrolled aggregates formation. In some cases, ligand-exchange disturbed the MNPs' surface spins and impaired the magnetic properties.

Ligand Modification

For thermolysis synthesis, hydrophobic surfactant (*e.g.* oleic acid, oleylamine) was commonly used as nucleation and growth control agent. The presence of unsaturated alkenyl (–CH₂=CH₂–) group within the carbon chain allowed several classical reactions such as maleinization ²²⁴ and epoxidation ^{225, 226} to be performed. From **Fig. 7a** illustrated the maleinization reaction involved the grafting of succinic anhydride group onto the hydrophobic ligand backbone in the allylic position at high temperature ²²⁷⁻²³². Such maleinization can be incorporated during the thermolysis synthesis of Fe₃O₄ MNPs (IONPs). The

resultant hydrophobic MNPs with embedded succinic anhydride groups was readily converted into the hydrophilic analogue through a simple hydrolysis using NaOH. The succinic acid formed after the hydrolysis helped to stabilize MNPs in aqueous medium. **Fig. 7b,c** showed the maleinized oleic acid-capped IONPs before and after the hydrolysis. Alternatively, epoxidation can be performed using peroxide reagents. Similar to the maleinization, epoxide group will be grafted to the oleic acid backbone afterwards. The amine-reactive epoxide group was capable of binding with amine-containing molecules through the amide linkage formation. By choosing suitable amine-containing hydrophilic ligand, epoxidized MNPs can be converted to hydrophilic MNPs ²²⁶.

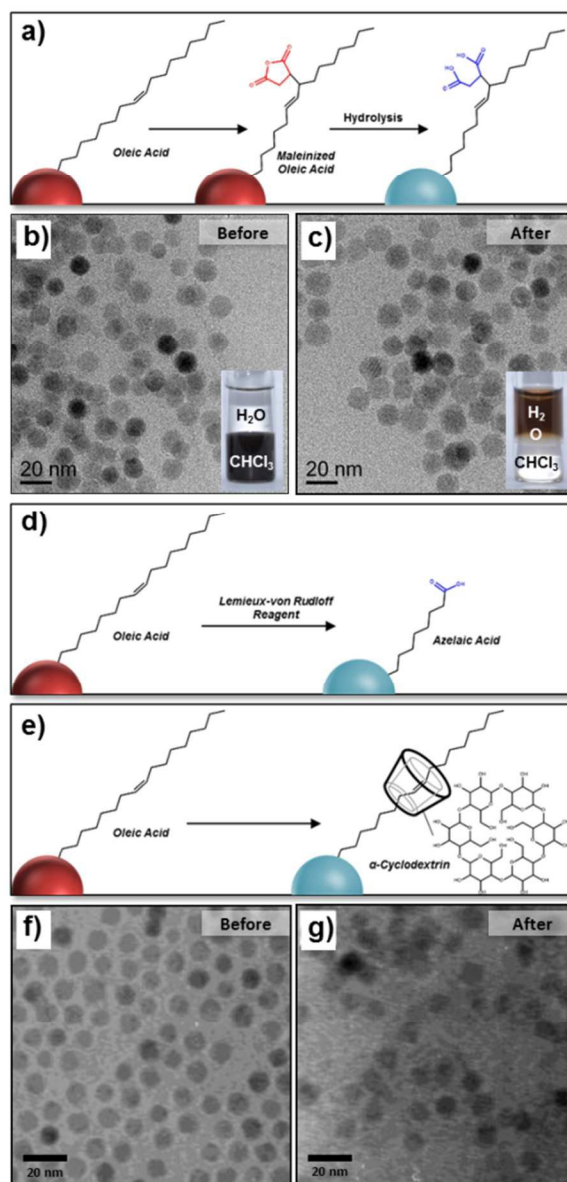


Fig. 7 Ligand Modification. (a) Oleic-acid coated MNPs maleinization; IONPs TEM images before (b) and after (c) hydrolysis. (d) Oleic acid coated MNPs oxidation with Lemieux-von Rudloff reagent; IONPs TEM images before (e) and after (f) oxidation. (g) Modification of oleic-acid coated MNPs with α -CD; IONPs TEM image before (h) and after (i) addition of α -CD. [Reproduced from Ref ²²⁴ with permission from the Royal Society of Chemistry.]. [Reprinted with permission from Ref ²³³. Copyright (2003) American Chemical Society.]

Post treatment involving fragmentation of alkenyl functional groups through controlled oxidation have also been proposed to directly convert the hydrophobic MNPs to the hydrophilic analogue. Strong oxidant such as Lemieux-von Rudloff reagent²³⁴⁻²³⁶, ozone²³⁷, potassium permanganate²³⁸, sodium periodate^{239, 240} were capable to oxidatively cleaved double bond at C9 position. As a result of this oxidative cleavage, oleic acid fragmented into azelaic acid (intact with the MNPs) and pelargonic acids (fragmented ligand), as shown in **Fig. 7d**. After the oxidation, the newly formed azelaic acid was capable to stabilize the inorganic MNPs in aqueous solution. Lastly, host-guest complex formation (**Fig. 7e**) between the MNPs hydrophobic ligands and hydrophilic polycyclic ring-like macromolecules helped to increase hydrophobic MNPs dispersity in aqueous solvent. With the hydrophobic cavity and hydrophilic perimeter, α -cyclodextrin (α -CD) was demonstrated to form an inclusion complex and stabilized IONPs²³³. **Fig 7f,g** showed IONPs TEM images before and after α -CD inclusion. Recently, Hu *et al.* also introduced a general protocol to directly fabricate functionalized MNPs from protected metal-organic precursors²⁴¹. Similar to the idea of incorporating maleinization or epoxidation reaction, the proposed one-step thermolysis protocols using protected metal-organic precursors in non-polar solvent. The post-synthesis de-protection step then revealed the protected functional groups. As a result, amine-functionalized MNPs were directly obtained.

Typical ligands modification strategies presented in this section commonly involved prolonged reaction time and harsh oxidizing reaction condition which can be detrimental to the water-soluble MNPs' physical properties. However, by strictly optimizing the reaction conditions, these strategies have been shown to successfully water-solubilize hydrophobic MNPs without compromising the MNPs' morphology and physical properties. Similar to ligand exchange, ligand modification strategies was also a ligand-specific technique.

Micelle Formation and Polymer Encapsulation

The state-of-the-art surfactant technology allowed the use of various amphiphilic surfactant molecules to render hydrophobic MNPs water soluble post-synthetically^{181, 242}. The hydrophobic capping agent on MNPs' surface normally existed in brush-like configuration. Based on this, both micelle formation and polymer encapsulation strategies have been employed to water solubilize hydrophobic MNPs by forming interdigitated bilayer structure between the hydrophobic ligands and the encapsulation agent's hydrophobic segment. Meanwhile, the hydrophilic polar segment of the encapsulation agent helped to enhance MNPs aqueous solubility. The hydrophobic-hydrophobic interaction and ligands intercalation helped to maintain the nanocomposites integrity. **Fig. 8a** depicted the typical single-encapsulated MNPs with amphiphilic brush copolymer. In the earlier hydrophobic MNPs development for biomedical applications, phospholipid micelles had been proposed to impart aqueous solubility^{243, 244}. Recently, the original oleic acid ligands also can be used for water-solubilizing hydrophobic MNPs by forming small, stable and non-aggregated MNPs in water with fatty acid bilayer structure²⁴⁵. Ionic surfactants inclusive of tetramethylammonium 11-aminoundecanoate⁷⁰, n-lauroyl sarcosine sodium²⁴⁴, cetyltrimethylammonium bromide (CTAB)²⁴⁶⁻²⁵⁰ and hexadecyltrimethylammonium bromide²⁰⁹ have been employed previously to stabilize hydrophobic MNPs in aqueous solution through micelle structure formation. **Fig.**

8b showed the typical water-dispersible CTAB-stabilized iron oxide MNPs^{248, 251}. The drawbacks of ionic surfactants were (i) the functional group in-availability for further bio-conjugation and (ii) poor colloidal solubility in ionic solution due to the anionic polar segment of the surfactant interaction with the positively charged metal ions, leading to severe aggregation.

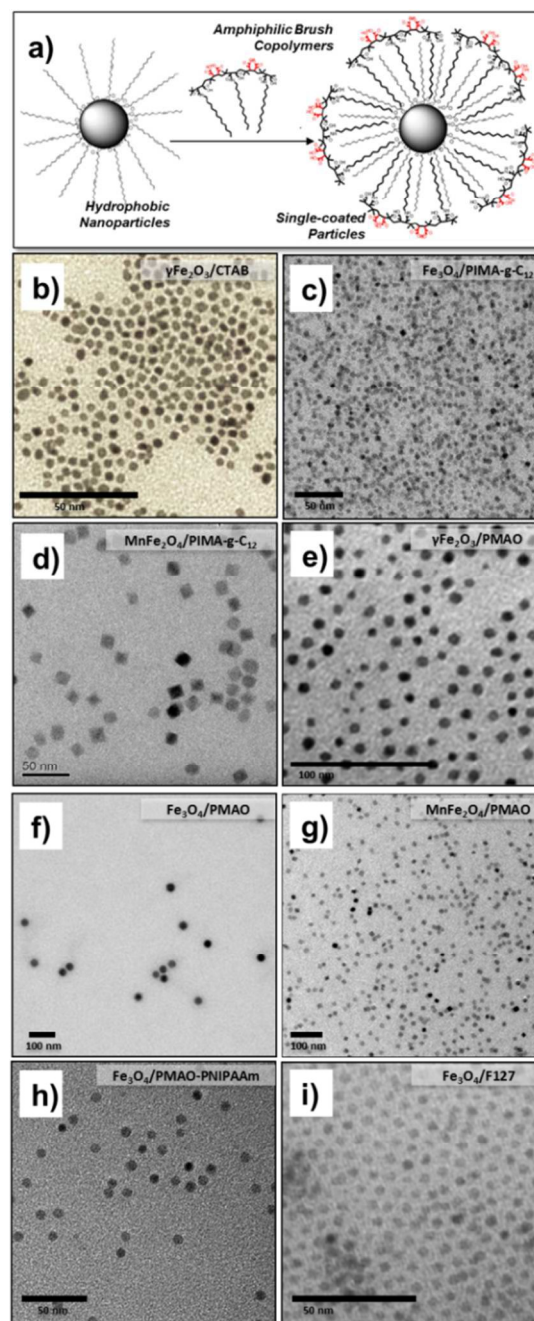


Fig. 8 Polymer Encapsulation. (a) Schematic diagram of single-encapsulated hydrophobic MNPs using amphiphilic brush copolymers. (b-j) TEM images of hydrophilic polymer-coated MNPs. [Reproduced from Ref^{39, 105, 248, 252} with permission from the Royal Society of Chemistry.]. [Reprinted with permission from Ref²⁵³. Copyright (2008) American Chemical Society.]. [Reprinted from Ref²⁵⁴. Copyright (2009) Wiley-VCH.]. [Reprinted from Ref²⁵⁵, with permission from Elsevier].

To resolve the poor colloidal solubility issue, amphiphilic brush and block copolymers materials have been applied to coat

a wide range of hydrophobic MNPs. Among different copolymers, maleic anhydride-based amphiphilic brush copolymers were commonly exploited due to its inexpensive cost and wide-commercial availability which inclusive of alkylamine modified poly (isobutylene-*alt*-maleic anhydride) or PIMA-*g*-C₁₂, poly (maleic anhydride-*alt*-1-tetradecene) or PMAT and poly (maleic anhydride-*alt*-1-octadecene) or PMAO were of interest^{105, 252, 256-259}. These polymaleic anhydrides possessed abundant hydrophobic aliphatic side chain which promoted intercalation with the MNPs hydrophobic ligands. As maleic anhydride groups also can be easily hydrolyzed into hydrophilic succinic acid group, the hydrolyzed polymaleic anhydrides was able to provide electrostatic repulsion in aqueous solvent that stabilize the hydrophobic core MNPs.

The use of alkyl-polymaleic anhydrides to transfer hydrophobic MNPs into aqueous solvent was demonstrated as early as 2004 by Pellegrino *et al.* to transfer various types of hydrophobic nanoparticles (*e.g.* CoPt, Au, CdSe/ZnS and Fe₂O₃) into aqueous solvent²⁵⁸. Later on, such technique was extended to other types of polymaleic anhydrides such as PMAO^{252, 253, 260, 261}. In some of the earlier literatures, bifunctional cross-linker agent such as bis(6-aminohexyl)amine was used to promote cross-linking between the amphiphilic brush copolymers. However, such cross-linker was found to be redundant later on^{105, 260}. To allow higher degree of of the polymaleic anhydrides' hydrophobicity tuning, Lin *et al.* engineered different amphiphilic brush copolymers simply by reacting PIMA with 1-dodecylamine at different molar ratio²⁵⁶. Other alkylamine with different aliphatic chain length such as *n*-octylamine can also be used^{262, 263}. The fine-tuning of the hydrophobic side chain length and the brush density allowed the encapsulation optimization of different hydrophobic inorganic nanoparticles. Some other commercially available polymaleic anhydrides with different hydrophobic pendant group such as ethanolamine-modified poly (styrene-co-maleic anhydride) and poly (maleic anhydride-*alt*-1-decene) possessed similar capabilities^{257, 264}. Moreover, the amine-reactive maleic anhydride group allowed the polymaleic anhydrides to be pre-modified with (i) fluorescence dye, (ii) antibiofouling agent (*e.g.* PEG) or even (iii) thermo-responsive ligand (*e.g.* PNIPAAm)^{39, 254, 259, 265-268}. Few examples of polymaleic anhydrides coated MNPs were summarized in **Fig. 8c-h**. Inexpensive and commercially available amphiphilic block copolymers such as pluronic F127 has also been reported to aid the phase transfer process (**Fig. 8i**)^{255, 269}. Besides polymaleic anhydrides, other amphiphilic polymers have been investigated for its water-solubilization capabilities such as (i) poly amino-acid such as poly (2-hydroxyethyl aspartamide) and oleylamine-reacted polysuccinimide (PSI)^{270, 271}.

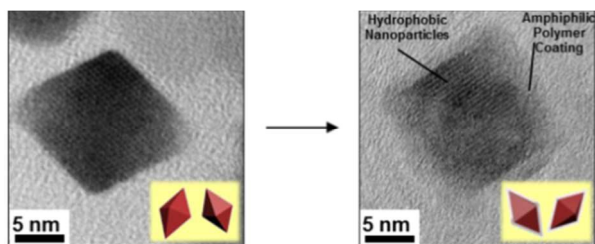


Fig. 9 High magnification MNPs TEM images: before (left) and after (right) polymeric encapsulation using PIMA-*g*-C₁₂. [Adapted from Ref¹⁰⁵ with permission from the Royal Society of Chemistry.]

Without proper control, the 0-D assembly process was often associated with the risk of uncontrolled collective MNPs

coating within the envelope of the phase-transfer agent²⁷²⁻²⁷⁴. Such collective coating can disrupt the benefits of the original monodisperse MNPs. So far, several optimization to achieve hydrophobic MNPs' single-encapsulation using polymaleic anhydride based have been investigated^{105, 260}. The ideal core-shell structure was confirmed from the observation of thin layer polymeric coating around the hydrophobic MNPs (**Fig. 9**). Moreover, the polymer-coated MNPs' hydrodynamic sizes were relatively close to the original hydrophobic MNPs in the organic solvents. Of the three possible techniques to achieve 0-D assembly, amphiphilic polymeric coating were the most suitable method as it offered a straightforward procedures with high repeatability and applicable to a wide range of hydrophobic nanoparticles. The coating also offered better colloidal stability and protection with less risk of impairing the encapsulated core nanoparticles' physical properties.

C. One-dimensional Nanostructures

Typical 1-D magnetic nanostructures in the form of rod-like structure or chain-like assemblies were commonly reported^{275, 276}. However, hydrophobic MNPs 1-D assembly was the least reported, especially for biomedical applications. The solution-based bottom-up 1-D MNPs assembly can be typically constructed through either (i) field-assisted assemblies or (ii) template-assisted assemblies. Field-assisted assemblies approach was generally weak as the magnetic field removal and exposure to rigorous agitation will compromise structural stability of the assemblies^{100, 277, 278}. For template-assisted assemblies, inorganic-based 1-D template (*e.g.* tellurium or gold nanorods) can be employed^{279, 280}. In terms of the template, organic polymeric material was more popular to assemble pre-formed hydrophobic MNPs²⁸¹⁻²⁸³. For example, Lee *et al.* devised bioinspired hyaluronic acid-graft-catechol (or HA-Catechol) with multiple ene-diol groups to assembly different nanoparticles (IONPs, Au and QDs) onto 1-D alignment (**Fig. 10a,b**). Alternatively, the template-assisted assembly can be performed using organic template with 1-D morphology such as carbon nanotubes (CNTs). To combine hydrophobic MNPs with CNTs structure, various methods have been proposed: (i) electrostatic complexation²⁸⁴ and (ii) in-situ thermolysis in the presence of single wall CNTs²⁸⁵ or multi-walled CNTs²⁸⁶⁻²⁸⁸. Although CNTs were a good carrier for several, well-controlled integration of hydrophobic MNPs into CNT structure was difficult to be achieved.

Recently, Baaziz *et al.* reported the formation of high density spherical iron oxide MNPs with narrow MNPs size distributions inside the multi-walled CNTs (MWCNTs) channels through direct thermolysis of Fe-stearate complex in 1-octadecene solvent with the presence of oleic acid and MWCNTs²⁸⁹. The original 1-D MWCNTs template (**Fig. 10c**) with open-ended channel (40–60 nm cavity diameter) was pre-treated at high temperature prior to the MNPs synthesis. After the in-situ synthesis, the MWCNTs channel was selectively filled with monodisperse IONPs (**Fig. 10d**). Interestingly, selective localization of the MNPs occurred in the outer surface of the MWCNTs when un-treated MWCNTs were used. On top of the in-situ synthesis, post-synthetic decoration of MWCNTs' outer surface with IONPs have been reported using two different approaches: (i) ligand exchange and (ii) 'click chemistry'²⁹⁰. The residual carboxylic acid of the oxidized MWCNTs surface provided a good anchor for the hydrophobic IONPs. Using the conventional ligand exchange method, hydrophobic MNPs can be water-solubilized by the MWCNTs (**Fig. 10e**). Alternatively, the hydrophobic IONPs can be firstly

ligand-exchanged to form azide-dendron capped MNPs while the alkyne-modified MWCNTs were prepared separately. Subsequently, through 'click chemistry', the azide-dendron capped MNPs were simply reacted with alkyne group of functionalized MWCNTs to form the 1-D nanocomposites (Fig. 10f). Generally, the template assisted assembly using 1-D CNTs nanostructure resulted in 1-D nanocomposites with better colloidal integrity as compared to the field-assisted assembly. However, due to its fabrication limitation and difficulties, 1-D assembly of hydrophobic MNPs was rarely considered for biomedical application.

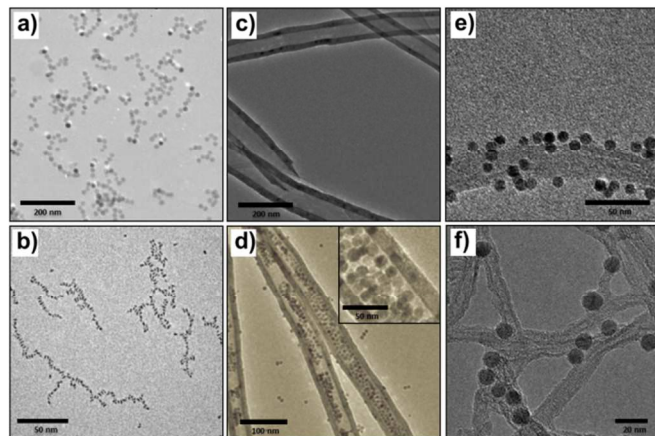


Fig. 10 Template-assisted MNPs 1-D assembly. TEM images of 1-D assembly of HA-catechol with (a) IONPs and (b) QDs. (c) MWCNTs and (d) MWCNTs selectively filled with IONPs. IONPs decorated MWCNTs through (e) direct ligand exchange and (f) 'click chemistry'. [Reprinted from Ref ²⁸². Copyright (2010) Wiley-VCH.]. [Reproduced from Ref ^{289, 290} with permission from the Royal Society of Chemistry.]

D. Two-dimensional Nanostructures

In the recent years, there has been a massive 2-D materials development for biomedical, energy storage and catalyst applications^{291, 292}. These included graphene and graphene oxide (GO)^{293, 294}, transition metal dichalcogenides such as molybdenum disulphide (MoS₂) and tungsten disulphide (WS₂)^{295, 296} as well as the hexagonal boron nitride (*h*-BN)^{297, 298}. Of all sheet-like materials, GO-based materials especially those that were chemically exfoliated from oxidized graphite were the most suitable materials for biomedical applications due its hydrophilicity with slight amphiphilic characteristics, functionalizable surface and easy processability²⁹⁹. Typically, GO was chemically exfoliated using modified Hummer's method^{294, 300}. The exfoliated GO sheets surface was dominated by: (i) hydrophobic sp³ carbon domains in the basal region and (ii) oxygen containing hydrophilic functional groups such as epoxy, carbonyl, carboxyl and hydroxyl. Due to their similar characteristic, GO-based materials can serve as a replacement for polymeric coating that was commonly used to prepare water-dispersible nanocomposites. Recently, GO nanosheets were also favoured over the conventional GO sheets due to higher surface activity and enhanced colloidal stability³⁰¹.

Several attempts to incorporate MNPs into GO to form GO-based magnetic nanocomposites have been reported in the literature^{40, 302-309}. Because of GO hydrophilicity, these nanocomposites were expected possess good aqueous colloidal stability and suitable biocompatibilities³¹⁰⁻³¹⁵, as required for biomedical applications. The decoration of graphene-based materials with hydrophobic MNPs can proceed through: (i)

direct synthesis using graphene-based materials template, (ii) chemical covalent conjugation, and (iii) post-synthetic non-covalent MNPs conjugation. Direct thermolysis of metal-organic precursors with the presence of graphene-based materials was the simplest method in forming the magnetic nanocomposites. For example, Cong *et al.* reported the one-step in-situ decoration of reduced GO sheets (rGO) with magnetite MNPs using thermolysis in polyol solvent (Fig. 11a)³⁰². The MNPs loading on rGO sheets were simply adjusted by varying precursors and rGO sheets molar ratio. Similarly, several other groups also reported MNPs decoration on rGO sheets through one-pot thermolysis synthesis in non-polar solvent^{303, 305}. Recently, Pang *et al.* proposed direct method of combining various inorganic nanoparticles (metal oxide and semiconductor) onto rGO sheets through the simultaneous thermolysis in non-polar solvent with the presence of oleylamine binder, stabilizer and reducing agents (Fig. 11b)³⁰⁴.

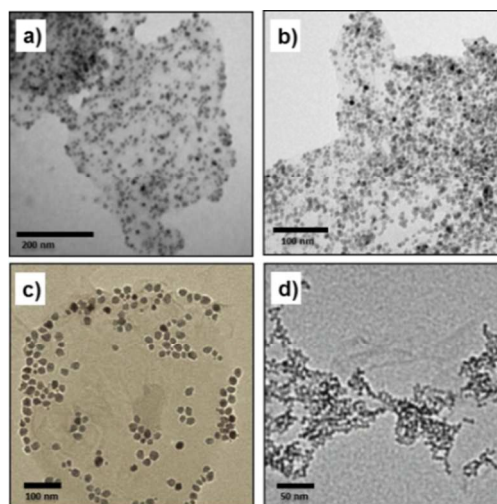


Fig. 11 Formation of 2-D sheet-like assembly. Direct in-situ MNPs synthesis using (a) rGO and (b) oleylamine/GO complex. Post-synthetic modification of pre-formed MNPs through covalent integration of: (c) ligand-exchanged MNPs with PEI-modified GO or (d) dextran-coated MNPs with GO. [Reprinted from Ref ³⁰². Copyright (2010) Wiley-VCH.]. [Reproduced from Ref ^{304, 306} with permission from The Royal Society of Chemistry.]. [Reprinted with permission from Ref ³⁰⁷. Copyright (2011) American Chemical Society.]

Alternatively, hydrophobic MNPs obtained from the thermal decomposition can undergo chemical surface modification, followed by the covalent integration with the GO sheets. This method required well-established hydrophobic MNPs surface modification strategies. For example, Zhang *et al.* presented the formation of hybrid Fe₃O₄-rGO nanocomposites through multi-step processes. Hydrophobic IONPs (Fe₃O₄) were ligand exchanged with DMSA while the GO was reacted and reduced with polyethyleneimine (PEI). The DMSA-modified IONPs were then conjugated covalently through carbodiimide chemistry (Fig. 11c)³⁰⁶. As the covalent conjugation proceeded through the hydrophilic functional groups of rGO, majority of the Fe₃O₄ were residing in the rGO sheets outer perimeter. Similarly, Chen *et al.* anchored aminodextran-coated IONPs onto GO by using carbodiimide chemistry (Fig. 11d)³⁰⁷. In terms of complexity, the covalent integration was unfavorable as the chemical surface modification often involved surface sensitive reaction. So far, by using either the direct synthesis or covalent integration, there was no good control over MNPs' size, size distribution and spatial distribution within the GO layer. Thus, separating the

hydrophobic MNPs synthesis and the post-synthetic coupling with graphene-based materials without the need of surface modification was a challenge.

Taking the advantage of the thinnest GO surfactant properties with its amphiphilic behaviors³¹⁶, and inspired by the hydrophobic MNPs water-solubilization using amphiphilic polymers³¹⁷, our group assembled hydrophobic MNPs onto GO using oleylamine binder to form water-dispersible nanocomposites⁴⁰. In the demonstration, MFNPs were loaded onto the oleylamine-modified GO (GO-*g*-OAM) through modified MESE technique (Fig. 12a). Oleylamine was initially intercalated onto GO surface to render GO slightly hydrophobic³¹⁸⁻³²⁰. As opposed to the expected spherical morphology, the resultant nanocomposites adopted 2-D sheet-like structure with hydrophobic MNPs organized on top of GO. The oleylamine binder helped to stabilize the hydrophobic MNPs on GO surface and majority of the MNPs were evenly distributed on the GO hydrophobic basal planes. The magnetic nanocomposites' loading was easily tuned by adjusting the GO and hydrophobic MNPs' mass ratio. Meanwhile, the hydrodynamic size of the MNPs/GO nanocomposites can be controlled by adjusting the sonication time³⁰⁸. Prolonged sonication duration fragmented GO sheets into much finer and smaller pieces. Several examples of the 2-D MNPs/GO nanocomposites were given in Fig. 12b,c. This non-covalent conjugation method was non-surface sensitive and therefore applicable to other hydrophobic inorganic nanoparticles. As a proof of concept, Yang *et al.* extended the method to water-solubilize Zn-doped AgInS₂ (AIZS) QDs³²¹. Lastly, because GO itself was unstable in ionic solution due to potential ionic-induced aggregation³¹³, simple additional surface modification such as PEGylation have to be carried out^{311, 322, 323}.

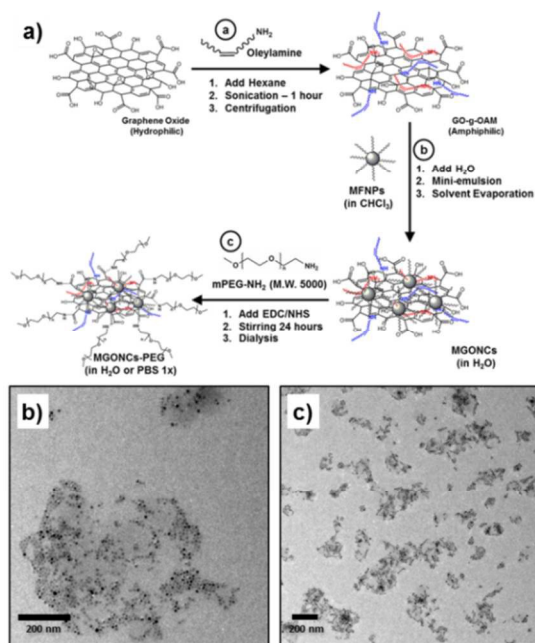


Fig. 12 (a) Formation of water-dispersible magnetic nanocomposites using GO-*g*-OAM [Reprinted from Ref⁴⁰. Copyright (2012) Wiley-VCH.]. (b,c) TEM images of MNPs/GO-*g*-OAM 2-D assemblies.

From all coupling strategies presented in this section, MNPs can be selectively decorated on the basal plane or the edges, depending on the coupling method used. Besides using GO template, other 2-D MNPs ensembles have also been reported.

For instance, hydrophobic iron-oxide MNPs can be decorated onto MoS₂ sheets³²⁴. Alternatively, Hyeon's group successfully synthesized 2-D neat arrangement of cubic MNPs embedded inside sheet-like carbon structures using thermolysis³²⁵. Although interesting, the biomedical applications of these nanocomposites have not been explored.

E. Three-dimensional Nanostructures

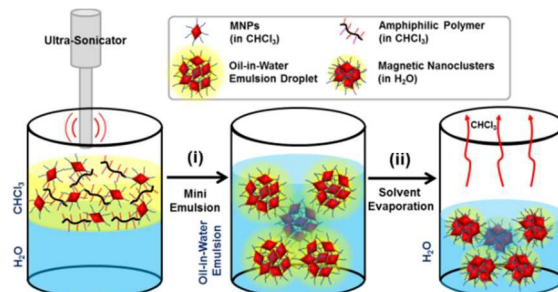


Fig. 13 Illustration of MESE process [Adapted from Ref³²⁶ with permission from The Royal Society of Chemistry.].

Inorganic MNPs 3-D ensembles usually referred to the collective MNPs encapsulation within continuous organic matrix, either within the whole matrix (*e.g.* micelle) or just partially distributed on the shell (*e.g.* vesicle). Conveniently, hydrophobic MNPs can be loaded onto amphiphilic coating materials to form stable 3-D secondary structure through similar non-covalent integration required to form 0-D polymeric encapsulation, mainly involving hydrophobic-hydrophobic and interdigitation interaction between the building block components. Through meticulous design, the overall nanostructures can be tuned from vesicles to micelles structures. In this section, two commonly used solution-based techniques to form MNPs 3-D assemblies will be of interest, namely: (i) oil-in-water MESE and (ii) direct solvent exchange (DSE) method. Amphiphilic brush and block copolymers were commonly employed to form water-soluble nanocomposites. The hydrophilic segments of the amphiphilic polymer, mainly comprises of oxygen-containing functional groups, provides electrostatic repulsion that stabilizes the nanocomposites in aqueous solvent. Meanwhile, the hydrophobic segment helps to provide steric hindrance to prevent unnecessary intercomposites agglomeration. Such chemical-based MNPs self-assembly offer controllable MNPs spatial distribution within the polymeric matrix and nanocomposites hydrodynamic size which influences the assembly magnetic behaviors.

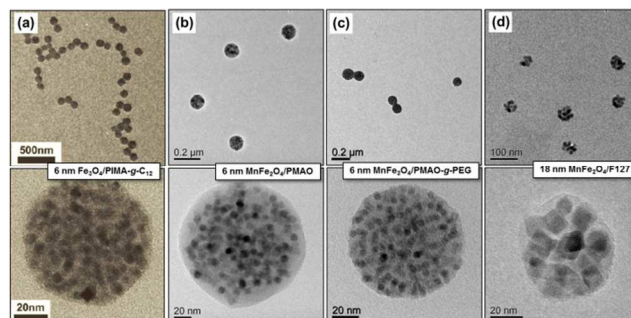


Fig. 14 Typical magnetic nanoclusters formed using: (a) 6 nm IONPs with PIMA-*g*-C₁₂/fluoresceinamine, 6 nm MFNPs with PMAO (b) and PMAO-*g*-PEG (c), (d) 18 nm MFNPs with F127. [Reproduced from Ref^{39, 326} with permission from The Royal Society of Chemistry.].

In the typical MESE process (Fig. 13), hydrophobic MNPs and amphiphilic polymers are simultaneously dissolved in water immiscible solvent (*e.g.* chloroform) and subsequently emulsifies with aqueous solution containing stabilizer such as polyvinyl alcohol using high power sonication or rigorous stirring process. The homogenization process breaks-up the organic oil phase in aqueous solvent, forming stable oil-in-water droplet. The volatile oil-phase is then evaporated under mild heating condition in which the droplet collapses and spherical magnetic nanocomposites are resulted. Based on MESE, our group devised several magnetic nanocomposites using different amphiphilic brush copolymers^{39, 43, 326, 327}. To simplify the synthetic process, the earlier inexpensive and commercially available amphiphilic brush copolymers such as alkylamine-modified PIMA as well as PMAO can be conveniently used. With the presence of amine-reactive maleic anhydride group, amphiphilic brush copolymers can be engineered beforehand to impart additional functionalities such as fluoresceinamine dye^{39, 327} or polyethylene glycol (PEG). Fig. 14a-c showed the typical uniform MNPs distribution within the different amphiphilic brush copolymers matrix (hydrodynamic size < 150 nm). Due to the nature of MESE process, the resultant nanocomposites assumed spherical micelle structure^{326, 328}. On top of that, inexpensive amphiphilic block copolymers Pluronic F127 can also be employed to host hydrophobic MNPs (unpublished results; Fig. 14d)³²⁹.

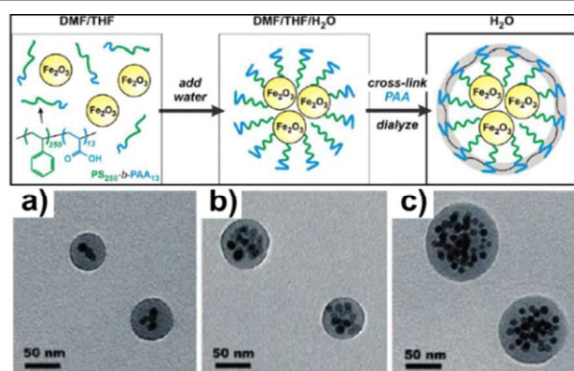


Fig. 15 (Top) Self-assembly of hydrophobic Fe_2O_3 MNPs using $\text{PS}_{250}\text{-}b\text{-PAA}_{13}$. (Bottom) TEM images of micelles loaded with 10.9 nm $\gamma\text{-Fe}_2\text{O}_3$ MNPs at different initial MNPs concentration. [Reprinted with permission from Ref³³⁰. Copyright (2005) American Chemical Society.]

Unfortunately, the formation of the 3-D MNPs ensembles using MESE method relied on the emulsion droplet formation. Thus, only spherical micelle structure can be fabricated. To enable more advanced structure fabrication (polymersomes or vesicles), either DSE or dialysis technique can be opted. Typical amphiphilic block copolymers (*e.g.* $\text{PS-}b\text{-PAA}$) can self-assemble into vesicles or rod-like structure proper solvent-polymer interactions³³¹. However, earlier attempt using DSE method to self-assemble hydrophobic MNPs into amphiphilic block copolymers often resulted in spherical micelle structure^{330, 332, 333}. The micelle formation was ascribed to the simultaneous de-solvation process of the MNPs and block copolymer during the coupling process. As depicted in Fig. 15, the loading of the hydrophobic MNPs was simply controlled by varying initial MNPs precursor concentration at fixed polymer concentration. Moreover, different core MNPs size can be encapsulated within individually segregated micelle without significant necking and different $\text{PS-}b\text{-PAA}$ chain length can be used as building block to form magnetic micelles³³⁴. The

resultant micelles can be further cross-linked to prevent micelle dissociation below the critical micelle concentration condition.

As opposed to micelle structure, incorporating hydrophobic MNPs into well-controlled vesicles or polymersomes structure were rather complicated³³⁵. Hickey *et al.* developed $\text{PAA}_{38}\text{-}b\text{-PS}_{154}$ to demonstrate the formation of controlled MNPs assemblies³³⁶. The structural control was obtained by changing the solvent/MNPs and polymer/MNPs interactions. Overall, three distinct structures (see Fig. 16a) were obtained, namely (i) magneto-core shell (MNPs radial distribution within the polymeric core and shell interface), (ii) magneto-micelles (uniform MNPs loading within polymeric matrix) and lastly (iii) magneto-polymersomes (hollow structure with surface-decorated MNPs). Three different solvents such as dimethylformamide (DMF), dioxane and tetrahydrofuran (THF) were employed to dissolve the $\text{PAA}_{38}\text{-}b\text{-PS}_{154}$. When DMF/THF (96.8% DMF) was employed, magneto-core shell structure was obtained. When 100% THF was used, the typical magneto-micelles similar to Taton's work were resulted³³⁰. Lastly, when dioxane/THF (96.8% dioxane) solvent was employed, both magneto-polymersomes and magneto-micelles co-exist simultaneously (see Fig. 16b,c).

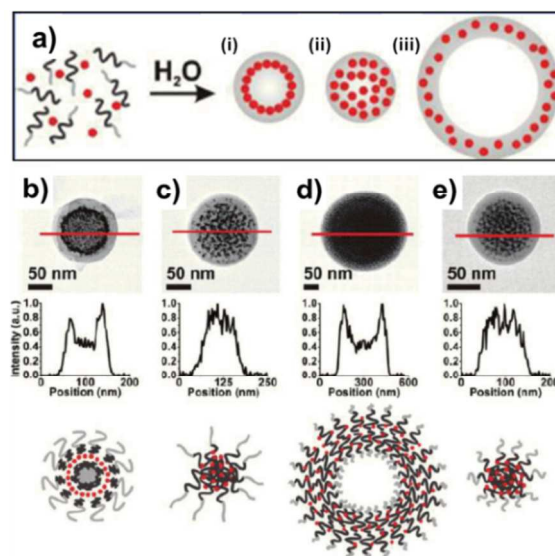


Fig. 16 (a) Self-assembly of hydrophobic MNPs and amphiphilic block copolymers: (i) magneto-core shell, (ii) magneto-micelles and (iii) magneto-polymersomes assemblies. Structural characterization of 5.6 nm IONPs into self-assembly: (b) magneto-core shell, (c) magneto-micelles, (d) magneto-polymersomes and (e) magneto-micelles assemblies. [Reprinted with permission from Ref³³⁶. Copyright (2011) American Chemical Society.]

The transition from micelle to vesicle (magneto-micelles to magneto-polymersomes) structure was driven by the need to balance both hydrophobic and hydrophilic segments of the block copolymers with the MNPs. The effective volume taken up by PS segment increased with the MNPs mass-percentage. Vesicle formations occurred when the relative hydrophilic/hydrophobic volume ratio became symmetrical. From the reported work, two critical factors affected the micelle-to-vesicle structure: (i) PS length within $\text{PAA-}b\text{-PS}$ and (ii) MNPs mass percentages. With the decrease in the hydrophobic PS length ($\text{PAA}_{38}\text{-}b\text{-PS}_{189} > \text{PAA}_{38}\text{-}b\text{-PS}_{154} > \text{PAA}_{38}\text{-}b\text{-PS}_{73}$), the percentage of magneto-polymersomes population over the magneto-micelles increased. This can be ascribed to the PS capability to solubilize hydrophobic MNPs. Longer PS length led to the higher hydrophobic MNPs solubilization.

Therefore, as the PS length increased, more MNPs were demanded to balance the relative volume ratio, to reach the threshold for the magneto-polymersomes formation. Regardless of the PS length, MNPs solutes were solubilized within the core of the polymeric vesicles at low mass percentages, forming the magneto-micelles. Increasing MNPs amount resulted in the increase of magneto-polymersomes population while reducing the magneto-micelles population. Thus, high MNPs loading density was favored to form magneto-polymersomes. Besides the magneto-micelle and magneto-polymersomes, magneto-core shell structure with unique radial MNPs arrangement emerged when DMF solvent was employed. As opposed to its good dissolution in THF, PS assumed compact structure in DMF and therefore PS lost its capability to accommodate hydrophobic MNPs. As a result, hydrophobic MNPs monolayer assembly took place in between the spherical interface between the polymer core and shell.

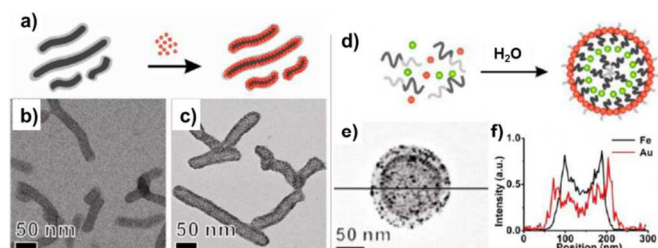


Fig. 17 (a) Formation of rod-like micelles decorated with AuNPs. TEM images comparison of rod-like micelles of PS₉₆-PAA₄₈ before (b) and after (c) the assembly. (d) Schematic illustration of the formation of multicomponent layered assemblies of both AuNPs and iron oxide MNPs. (e) TEM image and (f) EDS profile of micelle loaded with 4.5 nm iron oxide nanoparticles arranged in between the polymer core/polymer shell and AuNPs at the PS-PAA interface. [Reprinted with permission from Ref³³⁷. Copyright (2013) American Chemical Society.]

By using similar assembly technique that empowered the solvent/MNPs interaction, MNPs location within block-copolymer assemblies can be controlled³³⁷. Depending on the interfacial energy, Au nanoparticles (AuNPs) capped with different ligand induced different structure when assembled with PS-*b*-PAA. Dodecanethiol-capped AuNPs ligand preferred to form micelle structure while mercaptoundecanol-capped AuNPs preferred radial assemblies. The nanoparticles decorated polymeric assemblies can be formed on the preformed pure polymeric assemblies. Through this protocol, a non-spherical rod-like micelles assembly can be formed using rod-like PS₉₆-*b*-PAA₄₈ (**Fig. 17a-c**). In addition, multi-component assemblies were possible. For example, AuNPs can be decorated on the PS-PAA interface of the magneto-core shell comprised of iron oxide MNPs within the PS-PS interface (**Fig. 17 d-f**).

In the subsequent magneto-polymersomes development, Park's group focused on the fabrication of size-controlled densely packed magneto-polymersomes³³⁸. A great control over the MNPs distribution and polymersomes size control were demonstrated. With the increase in MNPs size, the resultant magneto-polymersomes diameter and the radial MNPs size distribution within the polymersome shell decreased. Recent work by Park's group demonstrated for the first time using solution phase assembly, the formation of 3-D magnetic nanocomposites with low dimensional MNPs assemblies of within the block copolymers PAA₃₈-*b*-PS₂₄₇ matrix³³⁹. As illustrated in **Fig. 18a**, instead of the typical isotropic 3-D arrangement of MNPs aggregates, anisotropic MNPs 1-D and

2-D arrays configurations were formed by varying the organic-solvent quality. The segregation of MNPs into low-dimensional assemblies was promoted by controlling MNPs-MNPs interaction as opposed to the MNPs-polymer interaction during the bottom-up self-assembly process. MNPs with strong interparticles interaction will assume 3-D assemblies within the polymeric matrix. Meanwhile, 1-D string assembly in magneto-micelles and 2-D sheet assembly in magneto core-shell assembly were obtained when the interparticle interaction was fine-tuned by introducing co-solvent during the self-assembly process. 2-D sheet assembly was resulted when normal solvent (*e.g.* DMF) was employed. When good-solvent (*e.g.* THF) was employed, 1-D string assembly was resulted. Overall, the nanocomposite size increased with the increase in MNPs core size, as well as PAA₃₈-*b*-PS₂₄₇ and MNPs concentration. The array structures were confirmed by electron tomography (see **Fig. 18e-f**). Such preferential interaction indicated that the solvent effect and its interaction of the MNPs building block and the polymeric coating materials were critical³⁴⁰.

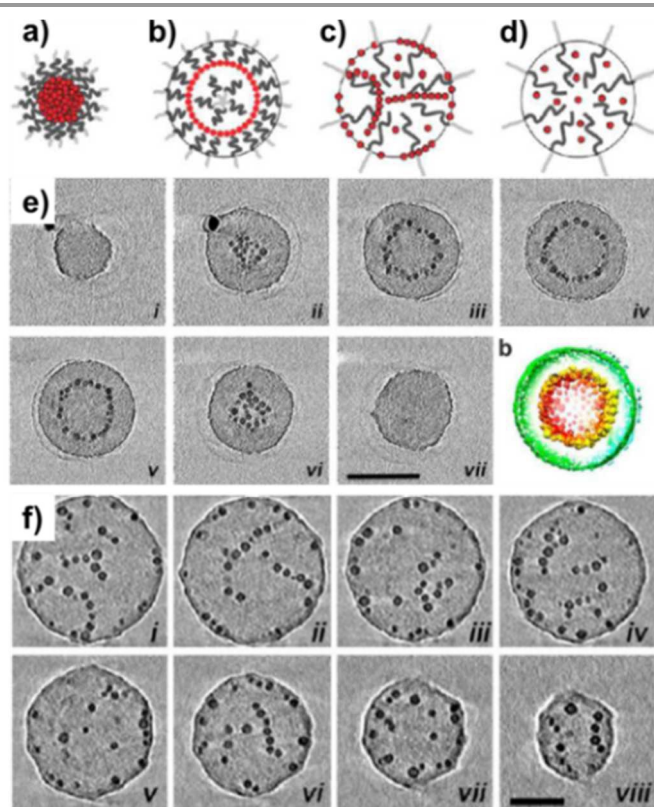


Fig. 18 Illustrations of four different MNPs arrangement within the 3-D polymeric matrix: (a) 3-D aggregates, (b) 2-D sheets, (c) 1-D string and (d) well-dispersed MNPs. 3-D structural analysis of (e) magneto-core/shell MNPs 2-D assembly and (f) magneto-micelle MNPs 1-D assembly by electron tomography. [Reprinted with permission from Ref³³⁹. Copyright (2013) American Chemical Society.]

4. MRI Applications of MNPs Ensembles

In this section, the design of hydrophobic MNPs assembly into organic functional coating will be discussed with regards to its MRI relaxometric performance. These include: (i) surface coating optimization of individual hydrophobic MNPs; (ii) collective encapsulation of hydrophobic MNPs to form magnetic nanoclusters; (iii) well-controlled hydrophobic MNPs spatial distribution within the organic matrix for off-resonance

imaging; (iv) dual-modalities MRI CAs development; and lastly (v) multifunctional magnetic nanocomposites development.

A. Coating-optimization for MR Relaxivities Enhancement

Surface functionalization to form 0-D nanostructures is essential to improve hydrophobic MNPs aqueous solubility. However, the presence of additional coating layer (e.g. polymer encapsulation) results in a 'dead-layer' which separates the core MNPs and surrounding waters. Depending on the coating chemistry, such configuration may be detrimental towards MRI relaxometric properties. Ideally, the surface coating of individual MNPs has to be optimized to boost the core MNPs potential through synergistic effect with the surface coating. For instance, the surface coating thickness and hydrophilicity can be enhanced to promote better MNPs/waters interaction and thus inducing faster water protons relaxation. The task to engineer single-encapsulated MNPs' was colossal as (i) the core MNPs has to possess excellent magnetic properties and (ii) the surface has to be tailored to enhance water accessibility, in terms of diffusion and retention. **Table 1** summarized some of notable works on obtaining the core-shell 0-D assembly and its related r_2 relaxivity values.

Table 1 r_2 relaxivities of various 0-D assemblies nanocomposites

Core MNPs/ Core Size [nm]	Organic Coating	Hydrodynamic Size [nm]	r_2 Relaxivity [mM ⁻¹ s ⁻¹]
Manganese Ferrite/6nm ^[341]	mPEG-g-PEI	30.6	331.8
Manganese Ferrite/6nm ^[341]	mPEG	11.2	75.7
Iron Oxide/10nm ^[342]	Pluronic F127	71	71.3
Iron Oxide/6nm ^[270]	PHEA-g-C ₁₈ -COOH	18.9	116
Iron Oxide/8nm ^[270]	PHEA-g-C ₁₈ -COOH	20.8	147
Iron Oxide/11nm ^[270]	PHEA-g-C ₁₈ -COOH	22.2	190
Manganese Ferrite/6nm ^[204]	PMAT	-	53
Pt3Co/6nm ^[268]	PMAO-g-PEG	50	451.2
Iron Oxide/8nm ^[168]	PMAO	43.7	43
Iron Oxide/6nm ^[39]	PIMA-g-C ₁₂ /Fluorescein	20.2	101
Iron Oxide/6nm ^[343]	DSPE-PEG (0.55 kDa)	16.6	201
Iron Oxide/6nm ^[343]	DSPE-PEG (5 kDa)	28.9	108
Iron Oxide/5nm ^[38]	DSPE-mPEG1000	14.8	130
Iron Oxide/14nm ^[38]	DSPE-mPEG1000	28.6	385
Iron Oxide/20nm ^[97]	1-Hexadecylamine Dendron	49	209.03
Iron Oxide/30nm ^[97]	1-Hexadecylamine Dendron	58	679.25
Iron Oxide/22nm ^[197]	PEG-phospholipid	44	761
Iron Oxide/12nm ^[212]	DMSA	-	218
Iron Oxide/10.9nm ^[344]	Diphosphate-PEG	-	79.1
Iron Oxide/10.9nm ^[344]	Hydroxamate-PEG	-	92.1
Iron Oxide/10.9nm ^[344]	Catechol-PEG	-	89.7
Iron Oxide/12nm ^[219]	Protocatechuic acid	14	220
Iron Oxide/11nm ^[216]	OligoPEG-DOPA	19	181
Iron Oxide/17nm ^[216]	OligoPEG-DOPA	-	234
Iron Oxide/23nm ^[216]	OligoPEG-DOPA	-	254
NaDyF ₄ /5.4nm ^[165]	PMAO-g-PEG	18.6	32
NaDyF ₄ /9.8nm ^[165]	PMAO-g-PEG	26.3	51
NaDyF ₄ /20.3nm ^[165]	PMAO-g-PEG	33.7	101
Fe ₃ C ₂ /20nm ^[142]	DSPE-PEG-NH ₂	50	312
Fe ₃ C ₂ /23nm ^[144]	DSPE-PEG-COOH	35	464

Based on outer-sphere relaxation theory, the r_2 value of individually-coated hydrophobic MNPs is proportional to the square of core MNPs magnetization in the motional averaging regime²⁰¹⁻²⁰³. Therefore, the selection of the hydrophobic MNPs

core with superior magnetic properties is important to improve the local magnetic field inhomogeneities. In order to achieve this, core MNPs magnetic properties can be improved by either: (i) increasing core MNPs sizes^{97, 165, 204, 270}, (ii) selecting different core MNPs with better intrinsic magnetic properties^{119, 140, 142, 144, 268} (e.g. FePt, Fe₃C₂, etc) or (iii) doping with other metals (e.g. metal-ferrites MFe₂O₄ where M = Ni, Fe, Co, Mn)^{21, 212, 216}¹¹⁵. In addition to this, increasing the geometric volume of the generated magnetic field by changing MNPs morphology from spherical into cubic or octapod shape also effectively led to significant improvement over the r_2 values^{97, 197}. Certain core MNPs also allowed more specific application. For instance, Dy-based MNPs can be used as the next generation ultrahigh field MRI CAs^{163, 165}. For example, 5–20 nm PMAO-g-PEG coated β -NaDyF₄ were more suitable for high field measurement¹⁶⁵. The measured r_2 relaxivity value increased with the increase in β -NaDyF₄ MNPs core size. Moreover, when measured at 9.4T, relaxivity enhancement as high as ~9 fold ($r_2 = 101 \text{ mM}^{-1}\text{s}^{-1}$ for 20.3 nm β -NaDyF₄ with r_2/r_1 ratio over ~300) was observed as compared to the measurement done at 3T.

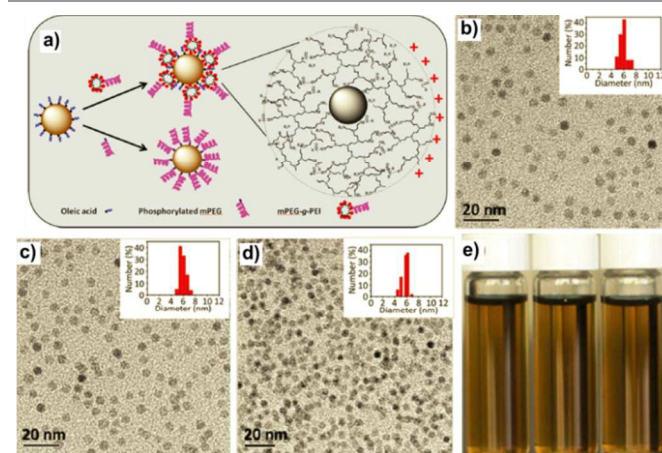


Fig. 19 (a) Coating of MNPs with mPEG-g-PEI and mPEG. TEM images of 6 nm MFNPs coated with (b) phosphorylated mPEG, (c) 50% mPEG-g-PEI and (d) 25% mPEG-g-PEI. (e) Digital photograph of MNPs coated with mPEG (left), 50% mPEG-g-PEI (center) and 25% mPEG-g-PEI (right). [Reprinted from Ref³⁴¹. Copyright (2014) Wiley-VCH.]

Besides core MNPs selection, independent surface coating engineering also improved relaxometric properties. Among 0-D nanostructures, ligand exchanged MNPs have been demonstrated to be particularly useful as MRI CAs, as long as the original MNPs physical properties was preserved and undesirable agglomeration was prevented. Recently, Liu *et al.* reported 6-fold r_2 value increase for mPEG-g-PEI coated manganese-doped ferrite MNPs (MFNPs) prepared via ligand-exchange, in comparison to the typical phosphorylated mPEG-coated MFNPs (**Fig. 19**). With hyper-branched mPEG-g-PEI coating, r_2 relaxivity up to 331.8 mM⁻¹s⁻¹ was recorded using 3T MRI system. Meanwhile, with mPEG coating, relatively low r_2 relaxivity of 75.7 mM⁻¹s⁻¹ was obtained. This significant MNPs relaxivity improvement was ascribed to the mPEG-g-PEI coating network ability to confine and trap water, therefore weakening the localized water diffusion coefficient. Because of confinement effect, diffusing water passing through the mPEG-g-PEI coating will experience tortuous path which allowed prolonged interaction within the magnetic field inhomogeneities proximity. The presence of PEG also allowed

fast water exchange with the bulk water proton. Both effects synergistically increased the water protons relaxivity greatly. Another similar work by Tong *et al.* whereby the MNPs' r_2 values reduced significantly with the increase in PEG chain length, suggested that the immobilized water molecules have to be within the MNPs core proximity in order to be affected by the local magnetic field inhomogeneities³⁸. Besides the hydrophilic end of the ligands, the recent work by Zeng *et al.* also emphasized the importance of ligand affinity to MNPs surface (in case of ligand exchanged MNPs) as it affected the surface spin disorder degree³⁴⁴.

In general, to engineer proper MRI T_2 CAs, core MNPs and surface coating have to be independently improved. Core MNPs with excellent magnetic properties will be more beneficial to accelerate water protons relaxation process. In addition to this, outer surface coating layer that was responsible to facilitate core MNPs interaction with surrounding water molecules have to be capable of promoting water accessibility and retention. When all these factors were taken into account, extremely high r_2 relaxivity value can be attained. For example, Hyeon's group fabricated water-dispersible cubic 22nm ferromagnetic Fe_3O_4 MNPs encapsulated with PEG-phospholipids that satisfied the aforementioned core MNPs and surface coating criterion; thus r_2 value as high as $761 \text{ mM}^{-1}\text{s}^{-1}$ was obtained.

On the other hand, to engineer proper MRI T_1 CAs, much attention must be directed into the surface coating engineering. To simply put, both core MNPs and surface coating have to be optimized all together. Recently, ultra-small as well as extremely small metal-oxide, lanthanide-oxide and lanthanide-fluoride MNPs were of interest as MRI T_1 CAs due to (i) high surface-to-volume ratio with large unpaired electrons and (ii) large surface spin disorders on the MNPs surface^{101, 160, 168, 248, 345, 346}. To demonstrate this effect, Kim *et al.* fabricated extremely small Fe_3O_4 MNPs (ESIONs) down to 1.5nm through the thermolysis of iron-oleate precursors in the presence of oleyl alcohol and oleic acid surfactant¹⁰¹. The oleyl alcohol surfactant played a critical role of mild reducing agent in order to form MNPs with size less than 3 nm. In order to prepare such ESIONs for T1-weighted MR imaging, the hydrophobic ESIONs was then stabilized through ligand exchange with PEG-derivatized phosphine oxide (PO-PEG). From the relaxivity measurement performed with 3T clinical MR scanner, 2.2 nm and 3 nm ESIONs exhibited r_1 of $4.78 \text{ mM}^{-1}\text{s}^{-1}$ and $4.77 \text{ mM}^{-1}\text{s}^{-1}$ respectively. The r_2 value of both 2.2 nm and 3 nm ESIONs were $17.5 \text{ mM}^{-1}\text{s}^{-1}$ and $29.2 \text{ mM}^{-1}\text{s}^{-1}$ respectively. Meanwhile, 12 nm Fe_3O_4 MNPs was also fabricated and measured as a comparison; in which r_1 value of $2.37 \text{ mM}^{-1}\text{s}^{-1}$ and high r_2 value of $58.8 \text{ mM}^{-1}\text{s}^{-1}$ were recorded. The smaller ESIONs exhibited low transverse relaxivity as compared to the larger MNPs due to the weak magnetic inhomogeneities. The calculated r_2/r_1 ratios of 2.2, 3, and 12 nm Fe_3O_4 MNPs were 3.67, 6.12, and 24.8 respectively. Thus, it can be concluded that ESIONs that comprised of ultra-small core MNPs can be used as efficient MRI T_1 CAs as compared to larger MNPs that has stronger susceptibility effect.

More recently, Fang *et al.* also demonstrated the PVP-coated ultra-small Gd_2O_3 (*ca.* 2.9 nm) fabricated through the combination between thermolysis and ligand exchange with PVP agent¹⁶⁸. With small hydrodynamic size of 15.7 nm in water, high r_1 value of $12.1 \text{ mM}^{-1}\text{s}^{-1}$ and low r_2 value of $33.2 \text{ mM}^{-1}\text{s}^{-1}$ (r_2/r_1 ratio = 2.7) were recorded at 7T MRI scanner. In a control experiment, when CTAB surfactant was used to encase the Gd_2O_3 through micelles formation instead of PVP

ligand exchange, relatively low r_1 value of $0.54 \text{ mM}^{-1}\text{s}^{-1}$ was obtained with high r_2/r_1 ratio of 22.1 for Gd_2O_3 -OA-CTAB sample ($r_2 = 11.92 \text{ mM}^{-1}\text{s}^{-1}$). The low r_1 value of Gd_2O_3 -OA-CTAB was due to the bi-layer long hydrophobic chains that effectively prevent the surrounding water protons from interacting with the gadolinium ions within the MNPs surface. For Gd_2O_3 -PVP, the hydrophilic functional group of PVP facilitated the surrounding water molecules to pass through the coating layer and therefore promoting the interaction with the Gd_2O_3 MNPs surface. As a result of this configuration, the T_1 relaxation time can be significantly reduced. Due to its ultra-small size, the Gd_2O_3 -PVP MNPs also (i) produced considerable signal enhancement in both liver and kidney, (ii) possessed long blood circulation time and (iii) accumulated in different organs such as liver, kidney and tumor during the *in-vivo* MR imaging study. Similarly, extremely small lanthanide fluoride MNPs (*ca.* 2 nm) NaGdF_4 obtained from the thermolysis and subsequent ligand-exchange with DSPE-PEG ligands has also been effectively demonstrated as MRI T_1 CAs¹⁶⁰. Due to the excellent uniformity and dispersity as well as its extremely small size (hydrodynamic size of 16 nm), the DSPE-PEG coated NaGdF_4 exhibited relatively high r_1 longitudinal relaxivity of $8.93 \text{ mM}^{-1}\text{s}^{-1}$ and low r_2 transverse relaxivity of $26.59 \text{ mM}^{-1}\text{s}^{-1}$ when measured using 3T clinical MRI scanner. The low r_2/r_1 value (2.98) indicated that DSPE-PEG coated NaGdF_4 MNPs was indeed suitable for T_1 -weighted MRI imaging.

Most of the investigations using extremely small MNPs as potential MRI T_1 CAs re-iterated similar significant findings in which the longitudinal relaxivity was indeed sensitive to coating and surface chemistry of the resultant magnetic nanocomposites. As such, surface coating optimization must be mandatorily considered during the MRI T_1 CAs development, especially to promote coating/MNPs interaction. Other unique nanostructures such as hollow core MNPs can also be considered to improve the surface availability and accessibility³⁴⁷.

B. Aggregation-induced MR Relaxivities Enhancement

From outer-sphere relaxation theory, transverse relaxivity increased with the MNPs' aggregate size within the molecular averaging regime.^{202, 203, 348} While increasing MNPs size can be achieved through thermolysis synthesis process, the use of large MNPs was limited by SPM critical size limit required to ensure colloidal stability. In order to retain the SPM behaviors, hydrophobic MNPs can be controllably aggregated into larger nanocomposites. Under strong external magnetic field, the assembly can be viewed as a giant magnetized sphere with enhanced local magnetic field inhomogeneities interaction volume. Thus, more nuclear spins perturbation occurs and the de-phasing rates increases. Although in several phase-transfer techniques, uncontrolled aggregation was not favored as it jeopardized the colloidal stability; MNPs clustering has positive impact on the MRI contrast enhancement effect. For instance, clinically used T_2 CAs such as Resovist[®] inherently exhibited certain degree of MNPs aggregation^{19, 199}. Currently, precise aggregate sizes control becomes a substantial challenge in the bottom-up synthesis of MRI T_2 CAs materials. To address this challenge, hierarchical assembly of primary hydrophobic MNPs core into secondary 1-D, 2-D and 3-D nanostructures using organic coating provides suitable platform to fabricate water-nanocomposites with controllable aggregates size. Several noteworthy results were summarized in **Table 2** and **Table 3**.

Table 2 r_2 relaxivities of various higher dimensional MNPs assemblies

Core MNPs/ Core Size [nm]	Organic Coating	Hydrodynamic Size [nm]	r_2 Relaxivity [mM ⁻¹ s ⁻¹]
Iron Oxide/6nm (35.4% loading) [39]	PIMA-g-C ₁₂ /Fluorescein	157	335
Iron Oxide/6nm (37.4% loading) [39]	PIMA-g-C ₁₂ /Fluorescein	158	439
Manganese Ferrite/6nm [326]	PMAO-g-PEG	104.7	246.0
Manganese Ferrite/11nm [326]	PMAO-g-PEG	106.2	280.2
Manganese Ferrite/11nm (w/QDs) [326]	PMAO-g-PEG	119.8	263.5
Manganese Ferrite/18nm [43]	PIMA-g-C ₁₂	132	632.6
Iron Oxide/6nm [334]	PS ₈₈ -b-PAA ₉	50*	319.5
Iron Oxide/6nm [334]	PS ₈₈ -b-PAA ₉	70*	381.5
Iron Oxide/6nm [334]	PS ₈₈ -b-PAA ₉	110*	400.1
Iron Oxide/15.5nm [338]	PAA ₃₈ -b-PS ₇₃	241	555
Iron Oxide/2.3nm [339]	PAA ₃₈ -b-PS ₂₄₇	-	63
Iron Oxide/3.2nm [339]	PAA ₃₈ -b-PS ₂₄₇	-	144
Iron Oxide/6.4nm [339]	PAA ₃₈ -b-PS ₂₄₇	160	278
Iron Oxide/7.5nm [339]	PAA ₃₈ -b-PS ₂₄₇	-	301
Manganese Ferrite/6nm [40]	GO-g-OAM	56.8/81.0	71.5/105.8
Manganese Ferrite/11nm [40]	GO-g-OAM	55.0/89.7	206.9/227.9
Manganese Ferrite/14nm [40]	GO-g-OAM	56.2/82.0	230.7/256.2
Iron Oxide/9nm (cubic)	GO-g-OAM	58.3/95.9	79.2/105.2
Iron Oxide/5nm [307]	Aminodextran/GO	174.4	76

* TEM average size.

Our group previously reported the loading of 6nm IONPs into PIMA-g-C₁₂ amphiphilic brush copolymers to form spherical IONCs with relatively small hydrodynamic size (< 250 nm) using MESE method³⁹. From the TEM images in **Fig. 20a-f**, the resultant hydrophilic IONCs loading can be varied by changing polymer to MNPs mass ratio. With the increase in IONPs loading, the resultant IONCs' saturation magnetization (M_s) increased. From the MR relaxivity study (**Fig. 20g**), the IONCs' r_2 relaxivities increased with the IONPs loading and linear relationship between r_2 and M_s value was observed. The IONCs can be considered as a large magnetized sphere that significantly enhanced the local magnetic field inhomogeneities interaction volume. Therefore, r_2 value as high as 439 mM⁻¹s⁻¹ was achieved with highest IONPs loading (*i.e.* 37.4wt%), more than 4-fold increase from the r_2 value of the single-coated IONPs (101 mM⁻¹s⁻¹) using similar polymer. Similarly, when core MNPs was replaced with MNPs with better magnetic properties such as 18 nm MFNPs⁴³, the r_2 value of the magnetic nanoclusters increased to 632.6 mM⁻¹s⁻¹. Several other spherical magnetic nanoclusters formed using emulsion-based technique and different types of organic matrix (*e.g.* CTAB, PMAO-g-PEG, PS-*b*-PAA) showed similar aggregation-induced MR relaxivities enhancement^{204, 326, 334, 349}. In addition, a series of complete comparative study was conducted by Weller's group using hydrophobic IONPs assembly in PEI-*b*-PCL-*b*-PEG amphiphilic block copolymers⁴¹. The experimental results highlighted the dependency of the clustered IONPs' r_2 values as a function of its hydrodynamic sizes (aggregate sizes) which confirmed the size-dependent transverse relaxivity model predicted by outer-sphere relaxation theory²⁰¹.

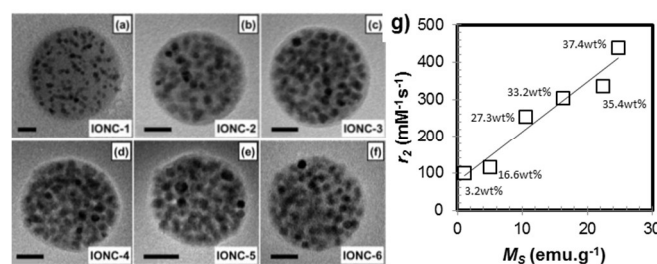


Fig. 20 (a-f) TEM images of superparamagnetic Fe₃O₄ nanoclusters with increasing loading from IONC-1 to IONC-6. (g) Plot of MR relaxivities measured in MRI 3T magnet against the IONC M_s values. [Reproduced from Ref³⁹ with permission from The Royal Society of Chemistry.]

Recently, aggregation-induced relaxometric properties was not only observed in spherical 3-D assemblies but also reported in non-isotropic low dimensional MNPs assemblies^{40, 302}. By decorating MFNPs on hydrophilic 2-D GO-g-OAM sheets, our group demonstrated similar size-dependent r_2 values. **Fig. 21** summarized the 2-D nanocomposites r_2 values fabricated using different sonication time against the MFNPs core size. Prolonged sonication time to 60 minutes during MESE process broken-up the GO sheets and therefore resulted in smaller nanocomposites, down to 50–60 nm hydrodynamic size range as opposed to the 80–90nm hydrodynamic size range when 12 minutes sonication time was used³⁰⁸. When the nanocomposites size was relatively large, the r_2 value increased with the core MFNPs size. However, when the size of these nanocomposites became comparable with the core MFNPs size, the aggregation effect gradually diminished with the increase in MFNPs core size. Thus, the overall aggregation-induced r_2 value enhancement depended heavily on the aggregation number.

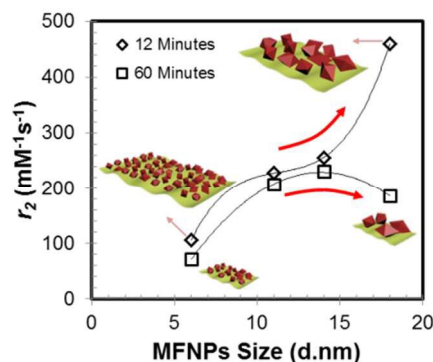


Fig. 21 Plot of r_2 relaxivities of MFNPs/GO assembly against the MFNPs core size. The assembly size decreased with prolonged sonication time. [Reprinted from Ref⁴⁰. Copyright (2012) Wiley-VCH.]

Other aggregation-induced MR relaxivities enhancement was also demonstrated by Park's group using low-dimensional assembly within 3-D magneto-polymerosomes structure (see **Fig. 16** and **Fig. 18**)^{336, 338, 339}. The size-controlled cooperative self-assembly of IONPs in PAA₃₈-*b*-PS₇₃ resulted in IONPs 2-D arrangement within the magneto-polymerosomes' shell. The magneto-polymerosomes' hydrodynamic size decreased while the r_2 value increased with the IONPs size. This phenomenon indicated that for polymerosomes structure, the core MNPs magnetic properties played a more vital role as compared to its hydrodynamic size. The highest r_2 value of 555 mM⁻¹s⁻¹ was reported for polymerosomes loaded with 15.5 nm IONPs.

Lastly, the controlled clustering effect was also observed in

paramagnetic Gd₂O₃ nanoparticulate T_1 CAs. Yuan *et al.* investigated the clustering effect of 10 nm Gd₂O₃ nanoplates assembled onto PMAO-*g*-PEG³²⁸. The Gd₂O₃ nanoplates clustering were controlled by tuning the Gd₂O₃ MNPs and polymer mass ratio. The nanoclusters with 27.9 wt% Gd₂O₃ loading exhibited the highest r_1 value of 7.948 mM⁻¹s⁻¹ in clinical 3T magnet, ~5.2 times higher than single-encapsulated Gd₂O₃ nanoplates (1.53 mM⁻¹s⁻¹) formed using CTAB micelle. Unexpectedly, the Gd₂O₃ MNPs aggregation also increased the r_2 values. In addition to this, recent work presented by Colvin's group using 2nm Gd₂O₃ nanoplates collectively encapsulated with either oleic acid bilayer structure or PAA-*g*-Oct brush copolymers suggested that surface coating was critical for paramagnetic MRI T_1 CAs¹⁶⁹. High r_1 value of 47.2 mM⁻¹s⁻¹ for PAA-*g*-Oct coated Gd₂O₃ (~6-times higher than the bilayer coated Gd₂O₃) can be ascribed to the PAA coating capability in modulating water molecules diffusion to the Gd³⁺ ions (Gd₂O₃ surface) as compared to the dense oleic acid bilayer coating.

Table 3 r_1 relaxivities of several paramagnetic MNPs assemblies.

Core MNPs/ Core Size [nm]	Organic Coating	Hydrodynamic Size [nm]	r_1 Relaxivity [mM ⁻¹ s ⁻¹]
Gd ₂ O ₃ nanoplates/10 nm [328]	PMAO- <i>g</i> -PEG	203.1	7.95
Gd ₂ O ₃ /2 nm [169]	Oleic Acid Bilayer	31.6	8.0
Gd ₂ O ₃ /2 nm [169]	PAA- <i>g</i> -Octylamine	27.8	47.2

Overall, aggregation-induced MR relaxivities enhancement are rigorously dependent on several factors: (i) the nature of the aggregated core MNPs; (ii) the functional organic coating chemistry; and lastly (iii) the aggregation number (aggregates size). The selection of high quality core MNPs is critical to determine contrast enhancement mechanism and performance. Meanwhile, surface coating is important to promote water diffusion and facilitate water exchange between the core MNPs and surrounding water molecules. Precise control over the aggregation behavior is important to achieve desirable MR relaxivities enhancement. While increasing the aggregate size improves the MR relaxivities, the colloidal stability of the resultant large nanocomposites might be at risk. Thus, a balance between aggregates size, stability and relaxometric properties must be considered when designing suitable MRI CAs.

C. Off-Resonance Saturation (ORS) Contrast Enhancement

Although T_2 -weighted imaging using nanoparticulate T_2 CAs was successful for various *in-vivo* studies; the negative contrast effects limited CAs detection and quantification during MR imaging. The darkened contrast became disadvantageous due to similar contrast from naturally occurring susceptibility-induced artifacts which led to the inconclusive data analysis, especially at high magnetic fields imaging³⁵⁰. To address this, Zurkiya *et al.* proposed an alternative approach by employing small SPM iron-oxide MNPs CAs for positive contrast generation based on the diffusion-mediated off-resonance saturation (ORS imaging)^{351, 352}. Typical SPM nanoparticles caused local magnetic field inhomogeneities which can be exploited to produce alternative contrast mechanism by applying off-resonance pulse to excite the water protons. The off-resonance terminology referred to the frequency that was different from the main bulk water peak on-resonance frequency. ORS relied on the water molecules diffusion within core MNPs proximity and thus it has high sensitivity towards the MNPs' local microscopic effects on the water diffusion.

When an off-resonance irradiation was applied, surrounding water protons (resonated at specific off-resonance frequency) saturated partially, depending on the frequency offset and water diffusion rate during the irradiation. The saturation at the corresponding off-resonance frequency caused main water peak reduction (Fig. 22). Moreover, the continuous rapid water diffusion to the MNPs proximity resulted in the constant incoming water protons saturation and therefore amplifying the ORS signal. The ORS effect was quantified by ORS ratio $[1 - (M_{sat}/M_0)]$; with M_{sat} and M_0 referred to the image amplitude with and without off-resonance irradiation respectively. As the ORS ratio increased linearly with the CAs concentration, MNPs real-time quantification can be performed.

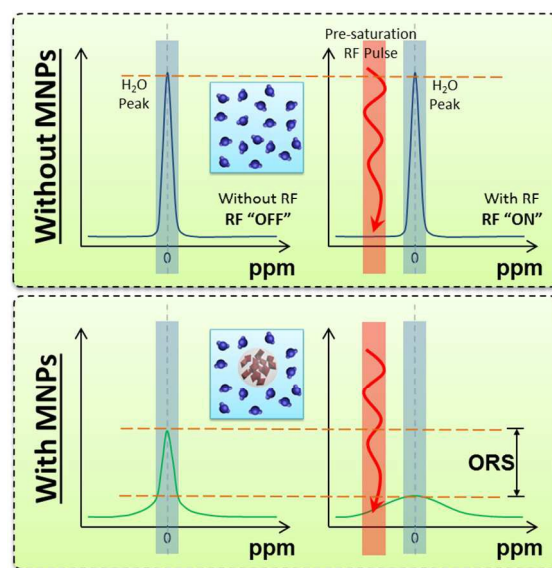


Fig. 22 Off-Resonance Saturation Imaging (ORS). Schematic illustration of MNPs-induced ORS contrast. With the presence of MNPs, the pre-saturation RF pulse decreased the signal intensity of water protons.

Based on the ORS method, Khemtong *et al.* demonstrated ultrasensitive MRI imaging to enhance the imaging efficacy of tumor biomarkers *in-vivo*, by using SPM nanoparticles loaded PEG-PLA block copolymers micelles (SPPM)⁴². The SPPM surface was functionalized by targeting agent for the integrin receptors on tumor endothelial cells which facilitated receptor-mediated endocytosis. With the presence of the SPPM that strongly enhanced water protons relaxation, the off-resonance irradiation allowed the saturation of larger volume fraction of diffusing water protons. From the reported *in-vivo* image acquisition of animals with A549 lung tumor xenografts with and without the presence of the ORS pulse as well as before and after SPPM injection, the ORS contrast in the injected tumors was observed. Although the typical T_2 -weighted images were not informative due to its similar signal intensity changes as compared to the control tumors and background tissues, the positive ORS contrast images (obtained by taking signal intensities differences between the acquired images) showed successful clear identification of the A549 tumors using cRGD-encoded SPPM probes. The ORS imaging significantly enhanced the contrast sensitivity and picomolar detection limit (10⁻¹² mol.L⁻¹) of the SPPM nanoprobe in the tumor tissues over the conventional T_2 -weighted imaging. Additional targeting agent also can be incorporated to improve the ORS imaging contrast, offering better opportunity for ultra-sensitive tumor detection in their early development. Unlike the

conventional T_2 -weighted imaging, the absent of pre-contrast scanning and the subsequent “on” (with pre-saturation) and “off” (without pre-saturation) contrast comparison were the advantages of ORS technique³⁵³.

Later on, Khemtong *et al.* explored the structure-property relationship between the 3-D MNPs assembly and ORS sensitivity using SPPM (6nm DSPE-PEG coated IONPs)³⁴³. The SPPM hydrodynamic size increased while the ORS sensitivity decreased with the increased in PEG chain length (0.55, 1, 2 and 5 kDa). Therefore, it was important to balance and improve the blood half-life and circulation while still maintaining the ORS sensitivity. One alternative proposed in their study was to increase the T_2 relaxivity of the ORS CAs which enhanced ORS detection while maintaining the required PEG length. From the theory, the ORS intensity was proportionally correlated closely to the nanoparticulate CAs longitudinal and transverse relaxivity (r_2/r_1 ratio)³⁴³. Thus, the development of strongly magnetized SPM nanoparticles (*e.g.* FeCo, FePt, MnFe₂O₄) and the controlled SPM nanoparticles assembly onto the organic coating that helped to improve the water protons transverse relaxations, will be beneficial to enhance the ORS detection sensitivity. The off-resonance frequencies of the applied pulse can be manipulated based on the on-resonance water-peak broadening window. As ORS favored positive signal generation and highly dependent on the water protons diffusion; this ultrasensitive imaging technique is suitable for positive MR imaging. Such desirable technique opens up new opportunities in the molecular imaging applications where both ultrasensitive and accurate detections are needed. It is foreseen that future efforts in ORS imaging CAs development will be comprehensively dependent on the water soluble magnetic superstructures development.

D. Magnetically-induced Off-Resonance Imaging (ORI)

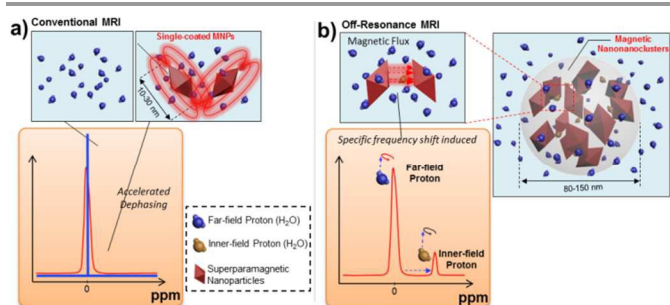


Fig. 23. Comparison between (a) typical MR imaging CAs mechanism and (b) magnetically-induced off-resonance MR imaging (ORI). [Reprinted from Ref⁴³. Copyright (2013) Wiley-VCH.]

The current clinical MRI technique are heavily dependent on the monochromatic effect due to its dependency on the local image brightening (T_1) and darkening (T_2) in producing its contrast effects (Fig. 23a). A new challenge rises due to the need of obtaining high resolution MRI images with improved detection sensitivities, while eliminating the background noise (improved contrast-to-noise ratio). To address this challenge, magnetically induced off-resonance imaging (ORI) was proposed by Zabow *et al.*³⁵⁴. In the early demonstration, uniform double-discs micro-engineered structures were used to create homogeneously localized magnetic field in the microscopic level. The usual spins de-phasing process due to local magnetic field inhomogeneities caused random shifts in the nuclear spins precession frequencies. However, because of

the newly-created uniform magnetic field by geometrical confinement, unique focused shift in the Larmor precession resonant frequencies was induced. Water molecules that diffused through the space in-between the double-discs exhibited discrete NMR frequency shift. The magnetically-induced water protons NMR spectral shift by magnetic nanostructures can be color-coded and thus used to enhance the multispectral MRI images acquisition. Unfortunately, the micro-engineered structure presented by Zabow's group was unlikely to be used clinically due to its large structural size.

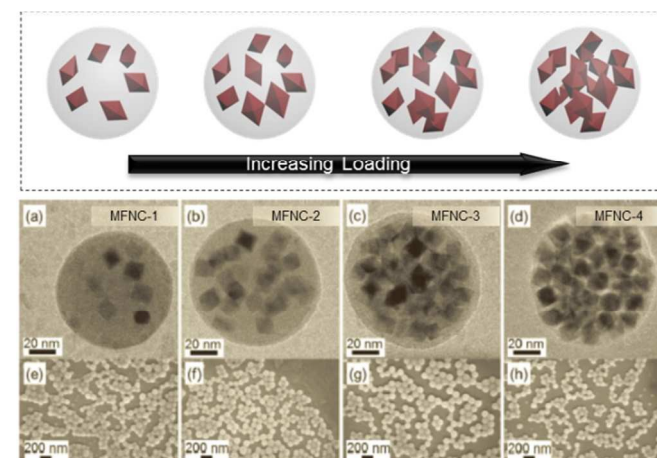


Fig. 24 TEM images of nanogels formed using PIMA-g-C₁₂ loaded with 18 nm octahedral shaped MFNPs with different loading. [Reprinted from Ref⁴³. Copyright (2013) Wiley-VCH.]

The challenge to create a suitable well-ordered structure nanoscopically inspired our group to devise a new method to generate positive MRI contrast⁴³. In order to emulate the idea of two parallel magnetic plates, well-controlled MNPs ensembles within polymeric matrix (Fig. 23b) were considered. The protons of the trapped water molecules inside the magnetic ensembles were focused to resonate at a distinct frequency from the typical bulk water protons. To realize this design, octahedral-shaped 18 nm MFNPs with faceted surfaces and high saturation magnetization (>100 emu.g⁻¹) were assembled onto PIMA-g-C₁₂ by using the bottom-up emulsion technique. Within the geometrical confinement, the resultant MFNCs loading tuning were accomplished to create MFNPs separation distance, simply by varying the MFNPs and PIMA-g-C₁₂ mass ratio (Fig. 24). In Fig. 25, the spectral shift of water protons induced by MFNCs was studied by NMR spectroscopy at different MFNPs loading. For four different MFNPs loading, distinct secondary peak occurred at approximately 3.2 ppm away from the on-resonance water proton peak which was attributed to the proton spectral shift induced by MFNCs. The secondary peak was not observed for single-coated MFNPs and for blank polymeric nanospheres. MFNCs with the lowest loading and larger MFNPs separation distance induced the most intense peak. The MFNCs exhibited certain degree of water absorption capability, allowing water molecules diffusion into the nanospheres inner-region while the hydrophobic segments of PIMA-g-C₁₂ significantly slowed the water diffusion through MFNCs and its exchanged with the bulk water pool. This effectively increased the interaction time between the absorbed water and the inner-field generated by MFNPs. When MFNCs loading was too high, the nanospheres interior of was dominated by hydrophobic MFNPs; diminishing the frequency-shifting capability because of water inaccessibility.

From the inset of **Fig. 25 (top-left)**, the typical darkening effect was observed with increasing MFNPs loading at 0Hz. At +2kHz, the expected signals were absence for all samples. Meanwhile, at -2kHz, MFNCs showed positive contrast with increasing signal intensity with the decrease in MFNCs loading. Both T_1 and T_2 of the secondary peak were found to be independent of the MFNCs loading density and very short ($T_1=270\text{ms}$ and $T_2=6\text{ms}$). The short relaxation time indicated that the water protons in the secondary peak underwent strong magnetic inhomogeneities influence within the MFNCs polymeric spheres which allowed rapid relaxation process.

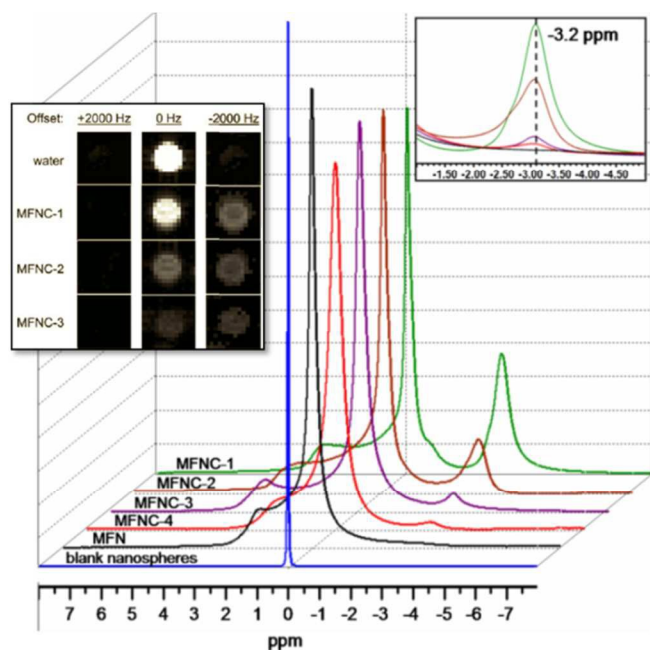


Fig. 25 (a) ^1H -NMR spectra of blank nanospheres, MFNPs and MFNCs samples with different loading. (Inset on the left: off-resonance MR spectroscopic images of pure water and MFNCs dispersed in water at +2kHz, 0Hz and -2kHz offset.) [Reprinted from Ref ⁴³. Copyright (2013) Wiley-VCH.]

In the proposed ORI method, the imaging and detection can be focused on the discrete NMR spectroscopic signal shift. Similar to chemical exchange saturation transfer (CEST) technique, ORI could effectively eliminate the background noise signals, allowing positive contrast generation. Currently, the basis of magnetically-induced ORI work was inconclusive, especially in terms of the origin of the peak-shift, peak intensity and the magnitude of the peak shift. However, based on Zabow's and Choo's works, the spatial distance between faceted surfaces was essential in designing proper ORI agents. The current MESE fabrication technique resulted in rather small nanocomposites structures, limiting the variation of MNPs' spatial distribution and separation distance. Other chemical-based MNPs assemblies techniques to produce nanocomposites with greater separation distance variation and water penetrability (*e.g.* magnetic-polymersomes) is indeed needed for fabricating ORI agents^{336-339, 355, 356}. Future efforts on engineering the precise MNPs distribution within the 3-D polymeric matrix may shed some light on the ORI mechanisms.

E. Dual-modalities MR Imaging

Typical MRI CAs were distinguished by its contrast mechanism (T_1 or T_2) in which each individual mechanism has

its prevailing drawbacks that limited its clinical application. For instance, T_2 CAs usually induced magnetic susceptibility artifacts with inherent negative contrast effects, complicating the MRI images analysis. In contrary, T_1 CAs produced high positive signal intensity that enabled better resolution to discern different tissue types. However, high T_1 CAs concentration was needed to yield meaningful results. Generally, single MRI modality was insufficient for high sensitivity diagnostic purposes. Recently, the increasing demand for sensitive MRI CAs has prompted the attempt to synergistically harness both T_1 and T_2 imaging benefits simultaneously to eliminate possible MRI artifacts and produce accurate information³⁵⁰. However, blatantly combining T_2 CAs with T_1 CAs through direct contact will result in the perturbation of paramagnetic T_1 CAs electronic spins due to local magnetic field inhomogeneities generated by T_2 CAs through strong magnetic coupling and high susceptibility effect. This process caused undesirable T_1 signal quenching, causing suppressed relaxometric properties. To design an efficient T_1 and T_2 dual-modalities nanoparticulate CAs (or DMCA), three possible rational concept to achieve dual-contrast imaging have been reported in literatures: (i) using inorganic MNPs that inherently exhibited both T_1 and T_2 relaxometric properties; (ii) complexation of T_2 MNPs CAs with T_1 CAs within organic functional coating; (iii) hybrid nanostructures formation to combine both T_1 and T_2 modalities.

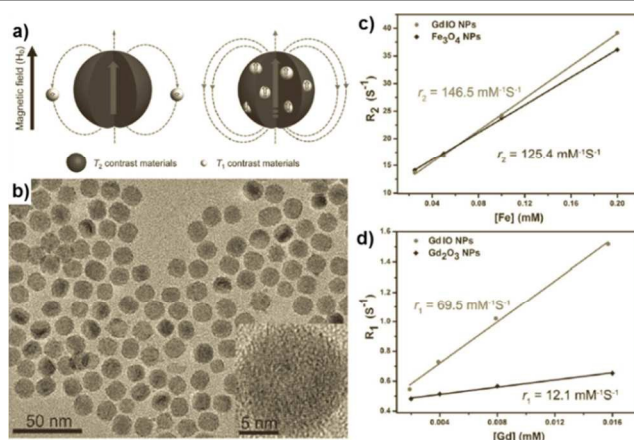


Fig. 26 Dual-modality MRI T_1 and T_2 imaging. (a) Spin phenomena between T_1 and T_2 CAs with different spatial arrangement. (b) TEM images of monodisperse GdIO. Plot of (c) T_2 and (d) T_1 relaxation rates against the metal ions concentration for GdIO, Fe_3O_4 and Gd_2O_3 MNPs in water. [Reprinted from Ref ³⁵⁷. Copyright (2012) Wiley-VCH.]

The simplest DMCA design relies on the use of MNPs that inherently allowed dual-contrast T_1 and T_2 weighted imaging capability. By tuning the MNPs core size, relatively small Fe_3O_4 and metal-doped (*e.g.* Zn or Mn) ferrites MNPs were potentially used as DMCA due to different MRI contrasting effect^{52, 193, 248, 345, 346}. For example, large manganese-doped iron oxide MNPs or MnIO ($\sim 12\text{nm}$) exhibited high r_2 value while small ($\sim 5\text{nm}$) MnIO exhibited high r_1 ³⁵⁸. Inherently, smaller MNPs possessed higher surface-to-volume ratio as compared to larger MNPs, exposing more spin disorders surface that promoted the MNPs interaction with the surrounding water protons which resulted in longitudinal relaxivity improvement¹⁰¹. Based on this MNPs nanosize-effect, the intermediate MnIO size ($\sim 7\text{nm}$) will then exhibited moderate r_2/r_1 ratio and better sensitivity, suitable as DMCA. However, such DMCA material was limited by its low relaxometric properties as compared to single-mode CAs.

Similarly, to improve the relaxometric properties, decent T_2 CAs can be combined with T_1 CAs through post-synthetic coupling. Conventionally “core-shell” structure can be adopted, with the nanoparticulate T_2 CAs core and T_1 CAs shell^{359, 360}. For examples, Park’s group synthesized Gd-labelled IONPs or GMNPs³⁵⁹ by modifying IONPs surface with multiple chelating ligands that were capable for complexing Gd^{3+} -ions. Because of the simultaneous presence of both MRI CAs, both positive ($r_1 = 11.17 \text{ mM}^{-1}\text{s}^{-1}$) and negative ($r_2 = 30.32 \text{ mM}^{-1}\text{s}^{-1}$) contrast enhancement were observed at 3T MRI scanner. Recently, similar DMCA was also obtained by using MFNPs coated with Gd-labeled DIB-PEG-NH₂ ligand³⁶¹. By using 0.55T MRI scanner, the resultant nanocomposites r_1 and r_2 values were $20.59 \text{ mM}^{-1}\text{s}^{-1}$ and $68.48 \text{ mM}^{-1}\text{s}^{-1}$ respectively. Apart from using the metal-oxide MNPs, “core-shell” structure involving Gd-labelled lanthanide-fluoride NaDyF₄ MNPs (stabilized by α -cyclodextrin) was also reportedly useful for both T_1 - and T_2 -weighted MRI imaging with r_2 relaxivity of $7.68 \text{ mM}^{-1}\text{s}^{-1}$ and r_1 relaxivity of $4.65 \text{ mM}^{-1}\text{s}^{-1}$ when measured at 0.5T MRI scanner¹⁶⁶.

The “core-shell” structure can also be attained through the seed-mediated epitaxial growth nanocomposites synthesis. For instance, Zhang *et al.* grown a shell of NaGdF₄:Yb³⁺,Er³⁺ (MRI T_1 CAs) on top of the NaDyF₄:Yb³⁺ (rod-like; MRI T_2 CAs) seed MNPs³⁶². The resultant hydrophobic NaDyF₄:Yb³⁺/NaGdF₄:Yb³⁺,Er³⁺ core-shell structure was then coated with PMAO-g-PEG to impart the water solubility property. The resultant r_1 and r_2 relaxivity values were measured to be $0.321 \text{ mM}^{-1}\text{s}^{-1}$ and $437.97 \text{ mM}^{-1}\text{s}^{-1}$ respectively. The high r_2 value was contributed by the presence of Dy-based core MNPs. Unfortunately, the outer shell paramagnetic Gd-based T_1 CAs materials ability to shorten longitudinal relaxation time was quenched by the presence of Dy³⁺ ions within the inner core.

As an alternative to alleviate the quenching effect, separating layer (or spacer) can be introduced to distance the T_1 CAs material from the T_2 CAs material and therefore reducing the possible magnetic coupling interaction. Based on this strategy, Cheng *et al.* fabricated dual T_1 - and T_2 -weighted MRI CAs by simply fusing different MNPs through a solid-state interfaces, creating a hybrid nanotrimer structure in dumbbell-like configuration¹⁴⁷. The hetero-nanotrimers (DB-HNTs) consisted of Fe₃O₄ MNPs, Pt and Au nanoparticles in dumbbell-like arrangement was synthesized through seed-mediated epitaxial growth. The presence of Pt nanocubes helped to distant Fe₃O₄ T_2 CAs material with Au nanoparticles. Subsequently, the surface of Au nanoparticles was functionalized with Gd-DOTA chelates to introduce the T_1 CAs material. With hydrodynamic size of $\sim 24.6 \text{ nm}$, Gd-functionalized DB-HNTs experienced r_1 of $3.88 \text{ mM} [\text{Fe} + \text{Gd}]^{-1}\text{s}^{-1}$ and r_2 of $128 \text{ mM} [\text{Fe}]^{-1}\text{s}^{-1}$ respectively. Without the presence of the Pt nanocubes spacer, Gd-functionalized HNTs experienced r_1 of $1.65 \text{ mM} [\text{Fe} + \text{Gd}]^{-1}\text{s}^{-1}$ and r_2 of $123 \text{ mM} [\text{Fe}]^{-1}\text{s}^{-1}$ respectively. Although the improvement on the r_1 longitudinal relaxivity was not significantly high, these comparative results indicated that heteronanostructures that combined both T_1 - and T_2 -weighted MRI CAs material with suitable spacer length helped to alleviate the quenching effect.

Despite the attempt to segregate T_2 CAs with T_1 CAs using spacer, provided that T_1 CAs was situated outside the T_2 CAs, quenching effect because of the opposing local magnetic field against the paramagnetic CAs spin alignment will always occur^{362, 363}. To alleviate T_1 signal weakening, engineered hybrid MNPs core with T_1 paramagnetic agents located within the T_2 CAs (see Fig. 26a)^{357, 364, 365}. With this configuration,

paramagnetic T_1 CAs exhibited similar parallel spin direction and ordering as the local magnetic field induced by the T_2 CAs; thus improving the T_1 contrast enhancement effect. In one of the early study, $\sim 14\text{nm}$ ultrasmall Gd₂O₃ clusters embedded within IONPs (GdIO) prepared from thermolysis synthesis was demonstrated for its synergistic T_1 - T_2 dual imaging properties (see Fig. 26b)³⁵⁷. Since the Gd₂O₃ MNPs were located within IONPs, the spin order of the Gd³⁺-ions was forced to align in the same direction as the local magnetic field induced by the IONPs, improving the T_1 contrast effect enhancement. Meanwhile, the simultaneous alignment of these Gd³⁺-ions also improved the local magnetic inhomogeneities and enhanced T_2 contrast effect. From the assessment using 0.5T MRI scanner, GdIO were suitable as DMCA (Fig. 26c,d) as compared to $\sim 14 \text{ nm}$ IONPs and $\sim 2 \text{ nm}$ Gd₂O₃ MNPs. The r_2 value of GdIO was $146.5 \text{ mM} [\text{Fe}]^{-1}\text{s}^{-1}$, relatively close to the magnetite nanoparticles ($125.4 \text{ mM} [\text{Fe}]^{-1}\text{s}^{-1}$). Meanwhile, the r_1 value of GdIO was $69.5 \text{ mM} [\text{Gd}]^{-1}\text{s}^{-1}$, almost 5.7 times of the ultrasmall Gd₂O₃ MNPs ($12.1 [\text{Gd}] \text{ mM}^{-1}\text{s}^{-1}$). The mutually enhanced local magnetic field of GdIO hybrid structures offered significant improvement in MRI relaxometric properties especially the T_1 -related effect. Following the pioneer work, Wang *et al.* fabricated $\sim 13.5\text{nm}$ GdIO contrast materials. Instead of single 0-D assembly, the GdIO sample was self-assembled using stearic acid modified polyethyleneimine into 3-D nanoclusters forming GdIO-stPEI³⁶⁵. When measured using 0.5T MRI scanner, GdIO-stPEI nanocomposites exhibited rather high r_2 ($181.49 \text{ mM}^{-1}\text{s}^{-1}$) and r_1 ($61.67 \text{ mM}^{-1}\text{s}^{-1}$) values with low r_2/r_1 ratio. Recently, Zhou *et al.* also successfully reduced the size of GdIO down to $\sim 2.8\text{nm}$ ³⁶⁴. Apart from this, $\sim 3.5\text{nm}$ and $\sim 4.8\text{nm}$ GdIO were also successfully synthesized and coated with zwitterionic dopamine sulfonate (ZDS) through ligand exchange process. Under 7T MRI scanner, ultrasmall $\sim 4.8\text{nm}$ GdIO exhibited r_1 relaxivity as high as $7.85 \text{ mM}^{-1}\text{s}^{-1}$ with r_2/r_1 as low as 5.24 ($r_2 = 41.14 \text{ mM}^{-1}\text{s}^{-1}$).

To sum-up the current DMCA development, ideal DMCA nanocomposites should produce significant dual-contrast effect (both T_1 and T_2 imaging capabilities)³⁵⁰. From several available DMCA designs, currently only engineered hybrid MNPs in which the paramagnetic species is embedded directly within the T_2 CAs that serves as a more suitable DMCA candidate.

F. Multifunctional Magnetic Nanocomposites

Lately, water soluble magnetic nanocomposites are also of interest, not only for its MRI application, but also for its advanced theranostic application^{366, 367}. In this section, multifunctional magnetic nanocomposites terminology referred to the engineered hybrid nanocomposites which promoted the imaging or therapy functionalities in combination with MRI functionality. For therapeutics, the presence of SPM nanoparticles inherently can be exploited for MFH applications under influence of alternating magnetic field^{40, 69, 368}. Therefore, regardless of the MNPs assembly, magnetic nanocomposites with SPM nanoparticles inherently carried therapeutic functionality and therefore satisfied the earlier multifunctional description. For example, the earlier 3-D MNPs assemblies with aggregation-induced relaxometric enhancement effect and magnetically-induced ORI potential were useful for MFH application. To demonstrate this, Liu *et al.* assessed the MFNPs loaded polymeric PIMA-g-C₁₂ nanospheres with different loading for its SAR values and related MFH application³²⁷. With concentration as low as $0.3 \text{ mg}\cdot\text{mL}^{-1}$ MFNPs, 18 nm MFNPs loaded nanoclusters was capable to exhibit SAR value of $332 \text{ W}\cdot\text{g}^{-1}$ at $4 \text{ kA}\cdot\text{m}^{-1}$ (435 kHz). In a similar way, the 2-D

assemblies of MFNPs and GO/oleylamine complex developed earlier (Fig. 21) was a good candidate as MFH heating agents on top of its potential as MRI T_2 CAs⁴⁰. For 14 nm MFNPs/GO-g-OAM 2-D assembly, besides the substantial T_2 contrast enhancement effect ($r_2 = 256.2 \text{ mM}^{-1}\text{s}^{-1}$), it was also suitable for MFH given its high SAR value of $1588.8 \text{ W}\cdot\text{g}^{-1}$. Relatively higher SAR value of $1988.1 \text{ W}\cdot\text{g}^{-1}$ can be achieved with 18 nm MFNPs assembly at $60 \text{ kA}\cdot\text{m}^{-1}$ (240 kHz)³⁰⁸. Similar to any other assembly, the collective encapsulation of MNPs produced relatively high r_2 value while the 2-D GO layer allowed fast heat dissipation to the surrounding medium.

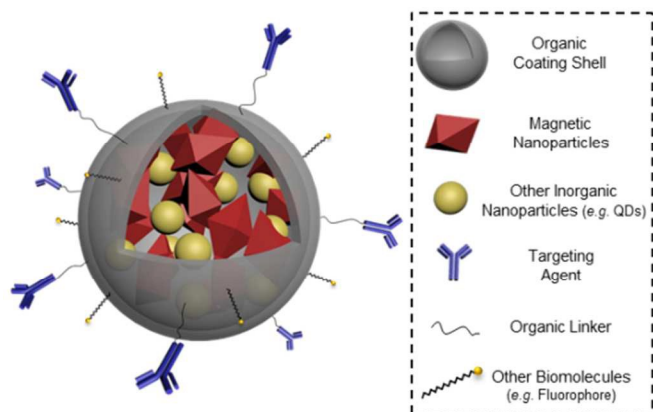


Fig. 27 Illustration of multifunctional nanocomposites, consisted of multiple inorganic nanoparticles cores, organic functional coating shell and various biomolecules conjugated to the surface of the nanocomposites such as targeting agent, fluorophores, antibiofouling agent and etc. The hydrophobic core region should be able to accommodate therapeutic payloads (e.g. drugs and genes).

In addition to MFH, multifunctional nanocomposites bearing SPM component will be responsive towards external magnetic field and therefore can be remotely manipulated, especially for guided drug and gene delivery as well as advanced cellular manipulation^{26, 32, 33, 369}. For targeted imaging and therapy, active surface functional group within the magnetic nanocomposites periphery can be further functionalized with specific targeting ligands with suitable affinity towards the desired cellular receptor of interest^{370, 371}. Moreover, various biomolecules such as drug or other sensing agent can also be incorporated through proper bio-conjugation techniques. Fig. 27 illustrated the ideal multifunctional magnetic nanocomposites design that accommodated hydrophobic inorganic nanoparticles within the hydrophobic inner cavity of the polymeric spheres. Meanwhile, the hydrophilic outer surface of the polymeric matrix can be conjugated with various specific functional ligands.

Of all various hydrophobic MNPs assembly methods, non-covalent integration water-solubilization technique used to prepare 3-D MNPs assembly provided a suitable platform for engineering multifunctional magnetic nanocomposites due to the possibility of simultaneous hydrophobic inorganic nanoparticles co-loading^{28, 271, 326, 372-374}. The polymeric coating materials diversity^{181, 207, 259, 317, 375} and the massive hydrophobic inorganic nanoparticles libraries from versatile thermolysis synthesis^{366, 376-379}, inclusive of up-/down-conversion nanoparticles (UCNPs), metallic nanoparticles, luminescent semiconductor QDs and wide range of metal oxides MNPs, offered indefinite combination in forming multifunctional nanocomposites. In this section, several magnetic nanocomposites by incorporating fluorescence dye or inorganic luminescence nanoparticles will be highlighted.

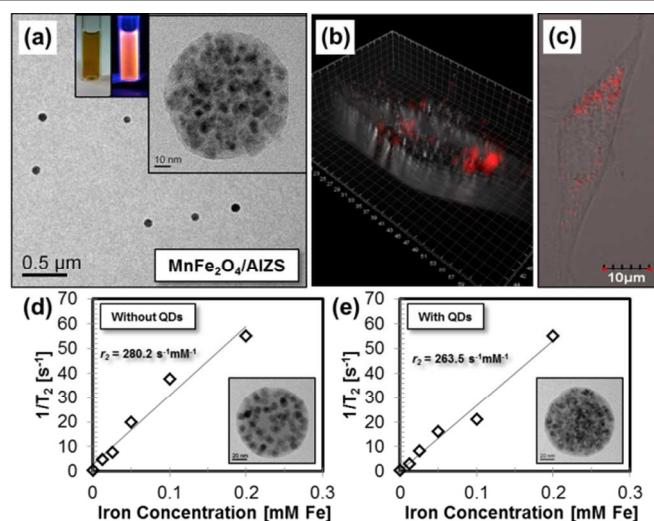


Fig. 28 (a,b) TEM images of A-MFNCs prepared by co-loading both MFNPs and AIZS QDs within PMAO-g-PEG matrix. (c,d) Confocal images of NIH/3T3 cells incubated with A-MFNCs. (e,f) Plot of T_2 relaxation rates against the iron concentration for MFNCs with and without AIZS QDs. [Reproduced from Ref³²⁶ with permission from The Royal Society of Chemistry.]

Through the covalent integration involving chemical conjugation using cross-linking agent, second modality such as fluorophore materials can be incorporated into the amphiphilic polymers prior to the nanocomposites formation. Based on this strategy, fluoresceinamine dye and oligothiopene have been pre-reacted with the amine-reactive amphiphilic polymaleic anhydrides to impart additional imaging functionality^{39, 380}. Although the addition of fluorophore material did not influence the magnetic nanocomposites morphology, the use of such pre-formed polymaleic anhydrides was discouraged due to its potential photo-bleaching risk. As an alternative, luminescence nanoparticles can be used to replace the labile fluorophore materials. Recently, our group demonstrated simultaneous loading of AIZS QDs and 11nm MFNPs onto the PMAO-g-PEG matrix to form magnetic fluorescent nanoclusters (A-MFNCs) using MESE method³²⁶. The TEM image in Fig. 28a portrayed the simultaneous existence of AIZS QDs and MFNPs within the spherical matrix structure. The resultant water-dispersible and biocompatible A-MFNCs sample was highly stable in PBS 1x solution, various pH conditions (pH 1.0–14.0) and temperature (25–45°C). The A-MFNCs sample was successfully demonstrated for cellular imaging using confocal microscopy (Fig. 28b,c). Conveniently, A-MFNCs were readily up-taken by NIH/3T3 cells after 24 hours incubation. From the MRI relaxivity measurement using 7T MRI scanner (Fig. 28d,e), the r_2 value of the MFNCs without AIZS QDs loading ($280.2 \text{ mM}^{-1}\text{s}^{-1}$) was comparable with the r_2 value of A-MFNCs sample ($263.5 \text{ mM}^{-1}\text{s}^{-1}$). From such comparison, the coupling of MNPs core with other inorganic non-magnetic nanoparticles has insignificant influence towards the MRI contrast enhancement effect. Using similar MESE method, several other multifunctional nanocomposites have been fabricated, either using hydrophilic poly(amino acid)-based or poly(lactic-co-glycolic acid) (PLGA) coating agents^{271, 381}. Such bifunctional nanocomposites were demonstrated for successful cellular uptake and imaging, MRI imaging, and drug delivery.

Apart from the MESE fabrication process, solvent destabilization method can be employed to form hybrid magneto-micelles. For example, Pellegrino's group prepared tri-functional polymeric nanobeads (MFNBs; see Fig. 29a-c)

with 70–160 nm size range through mixture destabilization, consisting of MFNPs, CdSe/ZnS QDs, and amphiphilic PMAO, followed by post-synthetic conjugation with folic acid molecules to form folic acid functionalized MFNBs (FA-MFNBS)²⁸. The choice of destabilizing solvent influenced both MFNBs size and morphology while the MFNBs' fluorescence and magnetic properties highly dependent on the QDs:MNPs mass ratio. The folic acid molecules allowed the bio-recognition towards cell lines with overexpressed folate receptors. Thus, the presence such fluorescent QDs within the FA-MFNBS allowed multiplex detection with enhanced cell separation capabilities due to uptake of the MFNBs. By using magnetic separation, specific targeting and sorting of human nasopharyngeal epidermal carcinoma cells using FA-MFNBS can be accomplished within 30–60 minutes of magnetic exposure. The estimated FA-MFNBS doped cells recovered during the trial-run showed a remarkable success in which the initial fraction of the doped cells was able to be recovered.

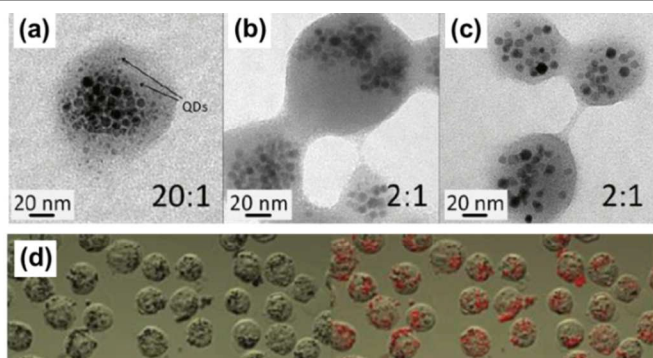


Fig. 29 TEM image of MFNBs Samples (a) and (b) were destabilized with acetonitrile at QD:MNPs ratio of 20:1 and 2:1 respectively. Sample (c) was destabilized by water at QD:MNPs ratio of 2:1. (d) Confocal images of KB cells targeted with folic acid functionalized MFNBs. [Reprinted with permission from Ref²⁸. Copyright (2011) American Chemical Society.]

Besides luminescent QDs, UCNPs can also be incorporated in a similar fashion. To demonstrate this, Xu and co-workers encapsulated both MNPs and UCNPs within PS₁₆-b-PAA₁₀ matrix to form spherical UC-IO@Polymer nanocomposites through MESE process (see Fig. 30a-b)³⁷⁴. In the process, water insoluble chemicals such as squaraine (SQ) dye and doxorubicin (DOX) can be simply one-step encapsulated during the emulsion process. Because of the presence of various imaging modalities, triple-modal imaging using up-conversion luminescence/down-conversion fluorescence luminescence/MRI or UCL/FL/MR imaging was enabled. From the T_2 -weighted images using 3T MRI scanner, the r_2 values of UC-IO@Polymer nanocomposites was $84 \text{ mM}^{-1}\text{s}^{-1}$. Despite its low relaxivity values, the multifunctional nanocomposites sample was also successfully demonstrated for its magnetic targeted drug delivery and imaging-guided therapy. Therefore, the presence of triple-modals UCL/FL/MR imaging helped to increase the overall imaging sensitivity.

On top of the post-synthetic combinatorial assembly, various single-phase multifunctional magnetic nanostructures such as engineered magnetic-QDs or magnetic/up-conversion nanoparticles have been introduced to enable multimodality imaging^{145, 163, 382, 383}. For instance, Liu *et al.* demonstrated the fabrication of hydrophobic NaGdF₄:Yb,Er magnetic/up-conversion fluorescent MNPs as dual-modal molecular imaging probes through the thermolysis process³⁸³. The resultant NaGdF₄:Yb,Er was then PEGylated through a simple ligand

exchange process. While the presence of gadolinium ions enabled the MRI T_1 contrast enhancement effect (r_1 of $3.33 \text{ mM}^{-1}\text{s}^{-1}$ at 4.7T MR scanner), the presence of the lanthanide ion dopants allowed the *in-vivo* up-conversion fluorescence imaging of tumors. Overall, in terms of the fabrication techniques and the physical properties tuning, post-synthetic assembly of different types of inorganic nanoparticles bearing different functionalities into single organic functional host can be considered to be more convenient and versatile as compared to the one-pot synthesise of single-phase multifunctional nanostructures.

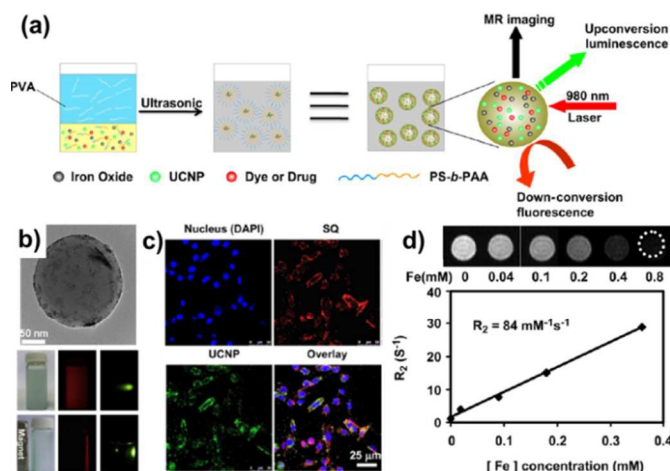


Fig. 30 (a) Synthesis and (b) TEM image of UC-IO@Polymer nanocomposite. (c) Confocal scanning microscopy images of 4T1 cells incubated with the UC-IO@Polymer loaded with squaraine (SQ) dye and (d) T_2 relaxation rates (r_2) of UC-IO@Polymer loaded with SQ dye at different iron concentrations. [Reprinted from Ref³⁷⁴, with permission from Elsevier].

To sum up this section, similar to the DMCA development, the design for suitable multifunctional magnetic nanocomposites has to accommodate few important principles. The vast libraries of hydrophobic inorganic nanoparticles³⁸⁴, especially MNPs, eases the fabrication of multifunctional magnetic nanocomposites by providing a wide range of possible combination. Apart from the fluorescence imaging functionality, multifunctional magnetic nanocomposites can also be fabricated by considering other inorganic nanoparticles with distinct theranostic functionalities (*e.g.* PET contrast agent, computed tomography contrast media, photothermal therapy heating agent and so on)^{55, 142, 150, 151, 166, 309, 385-387}. However, it is important to ensure that the co-loading of different inorganic nanoparticles have negligible adverse quenching effect towards the physical properties of each nanoparticles building block. Whether its 0-D, 1-D, 2-D and 3-D multifunctional magnetic nanostructures, proper core nanoparticles selections and proper organic functional coating design (*e.g.* functional group availability and expected colloidal stability), as well as its assembling method are very important and critical to ensure desired and optimized nanocomposites outcome.

G. Future Outlook and Perspective

Because of the increasing demand in early diagnosis and therapy at both molecular and cellular levels, efforts in nanostructured-based MRI CAs conceptualization and development have been ramped-up over the past decade. To cater for this need, this review article has covered the

significant materials and chemistry aspects in the nanoparticulate MRI CAs development. From both point of views, controlled synthesis and assembly method are critical as it determines the engineered nanocomposites' properties and characteristic. In most cases, the basic physics of MRI CAs remained unchanged regardless of the nanoparticulate system. However, since the MRI relaxometric properties required proper interaction (exchange kinetic) between the engineered MNPs and the surrounding water protons, the fundamental materials and chemistry aspects such as the MNPs synthesis and assembly became critical^{20, 159, 195, 363, 388}. Thus, significant progress has to be imparted on the nanoparticulate MRI CAs development. To achieve this, this review article focused on the two-steps nanoparticulate MRI CAs fabrication technique (covalent/non-covalent assembly of the hydrophobic MNPs into functional organic host) over the typical one-pot facile synthesis method^{20, 171, 173}. Taking the advantage of the post-synthetic water-solubilization process required; the MNPs synthesis and assembly process can therefore be segregated.

The process flow chart illustrated in **Fig. 31** highlighted the typical five stages strategy used in the nanostructured MRI CAs development involving hydrophobic MNPs obtained from the non-hydrolytic synthesis route. In stage (1), the two-steps assembly of hydrophobic MNPs into functional organic host fabrication technique enabled the substituting between different types of core MNPs and functional coating materials. In terms of hydrophobic core MNPs, various types of magnetic nanomaterials of different size, morphology (e.g. octahedral, disc-like, spherical, rod-like) and compositions (e.g. metal oxides, lanthanide oxides, metal ferrites, lanthanide fluorides) were easily fabricated with superior chemical and colloidal stability in non-polar solvent. In terms of functional organic host, various small ligands/surfactants, amphiphilic polymeric materials, carbon nanotubes and graphene-based materials were either available commercially or easily fabricated. The utmost importance in the MRI CAs development was the proper selection of suitable building block (both MNPs and surface coatings).

Apart from choosing the appropriate building blocks for the assembly, in stage (2), the MNPs assembly techniques (either covalent or non-covalent) must be properly engineered. Depending on the assembly techniques, the resultant magnetic nanocomposites may possess different architectures (e.g. different MNPs spatial distribution within the host matrix). In stage (3), these different MNPs configurations will be strongly associated with different MRI relaxometric performance or MRI potential applications. These include: (a) surface coating optimization of individual hydrophobic MNPs; (b) collective encapsulation of hydrophobic MNPs; (c,d) controlled hydrophobic MNPs spatial distribution for off-resonance imaging; (e) dual-modalities T_1/T_2 MRI CAs; and lastly (f) multifunctional magnetic nanocomposites.

In stage (4), the fabricated magnetic nanocomposites should possess suitable pH tolerance, salt tolerance and long-term *in-vitro* and *in-vivo* colloidal stability. Usually, the magnetic nanocomposites' surface zeta potential and hydrodynamic size have to be within the suitable range required. Subsequently in stage (5), *in-vitro* animal testing and optimization of the engineered magnetic nanocomposites have to be carried out before it can be translated into the human clinical trials and future clinical applications. In order to be suitable for clinical application, the aforementioned engineered MNPs should strictly satisfy several basic requirements such as possessing good biocompatibility (i.e. non-toxic with less adverse side

effects) and can be completely/safely excreted from body. In most publications, suitable cellular biocompatibility, viable delivery of MRI CAs to specific target imaging and *in-vivo* toxicity assessment through animal testing were often conducted^{101, 160, 168, 334, 388, 389353, 383}.

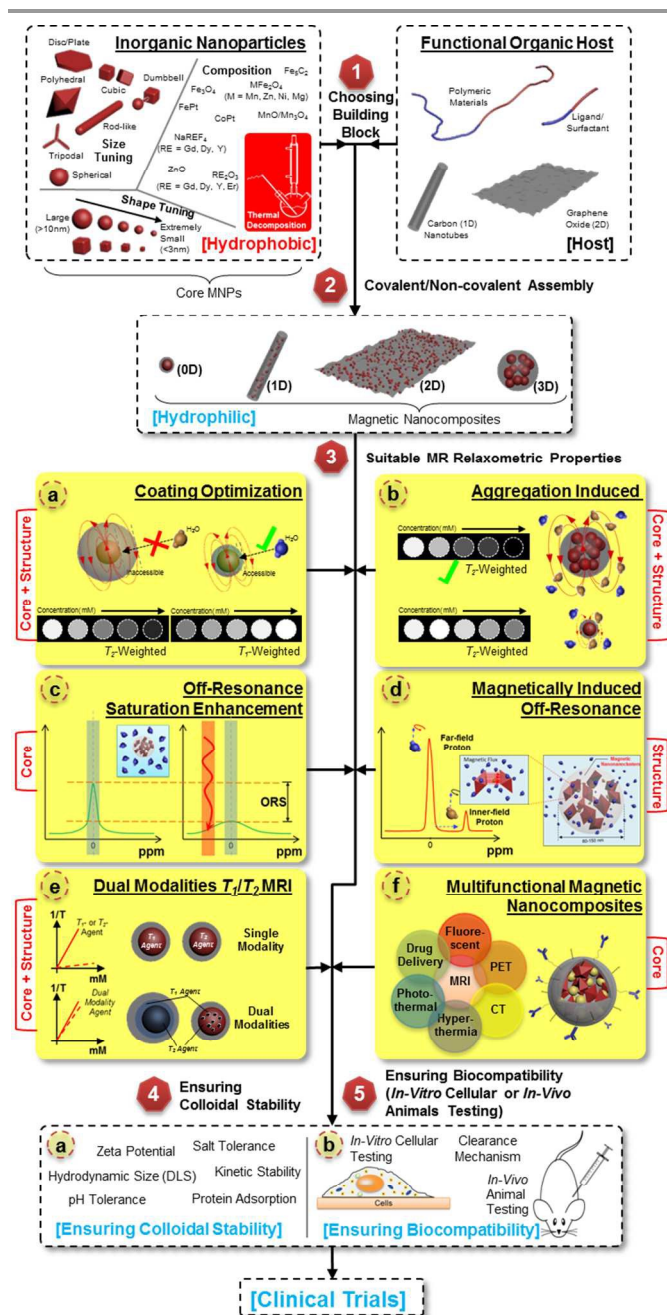


Fig. 31 Process flow in developing and designing engineered magnetic nanocomposites as MRI CAs based on MNPs prepared through non-hydrolytic route: (1) Selecting suitable building block (both core hydrophobic MNPs and the organic functional host); (2) Selecting suitable assembly technique (covalent or non-covalent bonding method); (3) Assessing the MR relaxometric properties for its specific application; (4) Colloidal stability assessment in various conditions, simulating possible *in-vivo* physiological conditions; (5) Biocompatibility assessment (*in-vitro* cellular testing and *in-vivo* animal testing). Finally, if all the comprehensive requirements were satisfied, clinical trials can be considered.

Although several promising engineered magnetic nanocomposites presented in this review article have satisfied

most of the basic pre-requisites for general biomedical application (from several *in-vitro* cellular testing or preliminary *in-vivo* animal studies)^{101, 160, 168, 334, 389, 390} and have been expected to provide suitable sensitivity for disease diagnosis; these magnetic nanocomposites does not necessarily translate into the direct clinical applications. The pathway to use these engineered MRI CAs in clinical applications can be foreseen to be very tortuous and expensive process. For most of the engineered nanoparticulate MRI CAs, the acute and chronic toxicity of each building blocks to human body still remained un-clarified^{186, 293, 315, 390, 391}.

In general, there are at least three critical pathways to be fulfilled for any clinical application of these engineered magnetic nanocomposites: (i) the safety, (ii) the medical utility and (iii) the industrialization aspects. The safety aspect of the engineered magnetic nanocomposites encompasses the nanomaterials structural-activity relationship or nano-SAR (*i.e.* the relationship between the nanoparticulate MRI CAs' structure and its inherent biological activity)^{392, 393} and the pharmacokinetics (human compatibility, bio-availability, bio-distribution, accumulation, bio-degradation and metabolism/clearance mechanisms)^{192, 394}. To fulfill the safety aspect, a more comprehensive preclinical testing (animal testing and model) on the engineered magnetic nanocomposites is required before the clinical development. Meanwhile, the medical utility or the efficacy of the engineered magnetic nanocomposites on human health must also be considered and analyzed thoroughly. Despite the presence of carbon-based organic coatings that encase the inorganic MNPs, several adverse side effects (such as sensitization and irritation) may arise due to the use and the *in-vivo* exposure or direct contact of the engineered magnetic nanocomposites to human body. Lastly, as the engineered magnetic nanocomposites have to be produced in large scale. Although small scale production to generate the required magnetic nanocomposites prototype is suffice for the clinical trials and development; standardized, scalable and reproducible mass production technique is still required for economical industrialization and its subsequent commercialization.

It is foreseen that engineered magnetic nanocomposites for biomedical application, especially for MRI CAs application, will still remain an active research area in two possible major directions: (i) the development of better and improved magnetic nanocomposites while creating the technology base, libraries and guidelines for future MRI CAs development; and (ii) the preparation of engineered magnetic nanocomposites for clinical application. One possible major MRI CAs development directions has been elaborated in this review article and covered most of the basic aspects required for future developments on more efficient and sophisticated MRI CAs with enhanced sensitivity, advanced functionalities and better biocompatibility. Interdisciplinary collaborative research is also highly recommended to both optimize the engineered magnetic nanocomposites fabrication methods as well as to gain a better understanding of the basic physicochemical properties of the nanocomposites correlation with their *in vivo* biological behaviors.

5. Conclusions

In the emerging functional inorganic nanoparticles development for biomedical applications, thermolysis of metal-organic precursors in non-polar solvent is the most suitable method in providing a wide range of inorganic nanoparticles libraries. The subset of inorganic nanoparticles libraries that

exhibits unique magnetic properties (*e.g.* paramagnetic and SPM), is suitable for MRI applications due to its capabilities of accelerating water protons de-phasing process. Despite its excellent physical properties, the resultant MNPs' hydrophobicity limits its biomedical application. To resolve this challenge, various post-synthetic water-solubilization techniques by imparting additional organic functional coating layer have been developed extensively. The separation between the hydrophobic MNPs synthesis and the post-synthetic phase transfer process unexpectedly allows controlled MNPs assemblies into four possible hierarchical architectures, namely 0-D, 1-D, 2-D and 3-D assemblies. Higher degree of freedom to form various functional nanocomposites can be achieved during phase-transfer process by choosing proper building blocks: (i) massive nanoparticles libraries selection from the thermolysis and (ii) substantial selection of the organic functional coating. Interestingly hydrophobic MNPs ensembles in organic coating exhibit different collective properties that are unattainable from bare individual MNPs or even bulk magnetic materials. Currently, hydrophobic MNPs ensembles have been exploited for MRI imaging. For instance: (i) surface coating optimization of single hydrophobic MNPs (0-D assembly) improved the MR relaxivity; (ii) controlled aggregation in 2-D and 3-D assemblies allowed significant MR relaxivity enhancement; well-ordered MNPs 3-D assembly within polymeric structures also opened-up new opportunity for either (iii) ORS imaging; (iv) magnetically-induced ORI; (v) dual MRI T_1 and T_2 imaging; or (iv) multimodality imaging and theranostic application. The improvement over magnetic behaviors and its relaxometric properties due to geometrical change within the assemblies hold a great promise to design future magnetic nanocomposites for biomedicine applications.

Abbreviation

A-MFNCs	Magnetic Fluorescent Nanoclusters
CA	Contrast Agent
DIB-PEG-NH ₂	PEG-3,4-dihydroxy benzyl amine
FA-MFNBS	Folic Acid-functionalized MFNBs
F127	Pluronic PEO-PPO-PEO Block Copolymer
GO	Graphene Oxide
GO-g-OAM	Oleylamine-modified Graphene Oxide
IONCs	Iron-oxide Nanoclusters
IONPs	Iron-oxide Nanoparticles
MFH	Magnetic Fluidic Hyperthermia
MFNBs	Magnetic Fluorescent Nanobeads
MFNCs	Manganese-doped Ferrite Nanoclusters
MFNPs	Manganese-doped Ferrite Nanoparticles
MNPs	Magnetic Nanoparticles
MRI	Magnetic Resonance Imaging
OA	Oleic Acid
OAm	Oleylamine
ORI	Off-Resonance Imaging
ORS	Off-Resonance Saturation Imaging
PAA	Poly (Acrylic Acid)
PAA-g-Oct	Octylamine-modified PAA
PEI	Poly (Ethylene Imine)
PHEA	Poly (2-hydroxyethyl aspartamide)
PEG	Poly (Ethylene Glycol)
PIMA	Poly (Isobutylene-alt-maleic anhydride)
PIMA-g-C ₁₂	Dodecylamine-grafted PIMA
PMAO	Poly (Maleic Anhydride-alt-1-Octadecene)
PMAO-g-PEG	PEGylated PMAO
PS	Poly (styrene)
PS- <i>b</i> -PAA	Poly (styrene) block Poly (Acrylic Acid)

PVP	Poly Vinyl Pyrrolidone
QDs	Quantum Dots
SAR	Specific Absorption Rate (MFH)
UCNPs	Up-converting Nanoparticles
USIONPs	Ultra-small Iron-oxide Nanoparticles

Acknowledgements

Xue Jun Min and Erwin Peng would like to acknowledge the funding support by Singapore MOE Grant WBS R-284-000-102-112.

Notes and references

^a Department of Materials Science and Engineering.
Faculty of Engineering, National University of Singapore.
9 Engineering Drive 1, Singapore 117576.
Fax : +65 6776-3604;
Tel : +65 6516-4655.

* Corresponding Authors.

Email: mseer@nus.edu.sg / msexuejm@nus.edu.sg

- S. L. Pimlott and A. Sutherland, *Chemical Society Reviews*, 2011, 40, 149-162.
- S. Gambhir, *Nature Reviews Cancer*, 2002, 2, 683 - 693.
- M. Gerd and S. K. Joel, *Physics in Medicine and Biology*, 2006, 51, R117.
- W. Kalender, *Phys Med Biol*, 2006, 51, R29 - 43.
- F. A. Gallagher, *Clinical Radiology*, 2010, 65, 557-566.
- R. B. Lauffer, *Chemical Reviews*, 1987, 87, 901-927.
- P. Caravan, J. J. Ellison, T. J. McMurphy and R. B. Lauffer, *Chemical Reviews*, 1999, 99, 2293-2352.
- D. Burstein, *NMR Biomed*, 2006, 19, 669 - 680.
- A. Kherlopian, T. Song, Q. Duan, M. Neimark, M. Po, J. Gohagan and A. Laine, *BMC Systems Biology*, 2008, 2, 74.
- W. DeMartini, C. Lehman and S. Partridge, *Academic Radiology*, 2008, 15, 408-416.
- H. Miao, H. Fukatsu and T. Ishigaki, *European Journal of Radiology*, 2007, 61, 297-302.
- M. S. Bhojani, M. Van Dort, A. Rehemtulla and B. D. Ross, *Molecular Pharmaceutics*, 2010, 7, 1921-1929.
- R. B. Rock, M. Olin, C. A. Baker, T. W. Molitor and P. K. Peterson, *Clinical Microbiology Reviews*, 2008, 21, 243-261.
- G. B. Frisoni, N. C. Fox, C. R. Jack, P. Scheltens and P. M. Thompson, *Nat Rev Neurol*, 2010, 6, 67-77.
- T. Lockie, E. Nagel, S. Redwood and S. Plein, *Circulation*, 2009, 119, 1671-1681.
- D. Sosnovik, M. Nahrendorf and R. Weissleder, *Basic Res Cardiol*, 2008, 103, 122-130.
- N. Boutry, M. Morel, R.-M. Flipo, X. Demondion and A. Cotten, *American Journal of Roentgenology*, 2007, 189, 1502-1509.
- G. E. Gold, E. Han, J. Stainsby, G. Wright, J. Brittain and C. Beaulieu, *American Journal of Roentgenology*, 2004, 183, 343-351.
- Y.-X. Wang, S. Hussain and G. Krestin, *Eur Radiol*, 2001, 11, 2319-2331.
- H. B. Na, I. C. Song and T. Hyeon, *Advanced Materials*, 2009, 21, 2133-2148.
- J.-H. Lee, Y.-M. Huh, Y.-w. Jun, J.-w. Seo, J.-t. Jang, H.-T. Song, S. Kim, E.-J. Cho, H.-G. Yoon, J.-S. Suh and J. Cheon, *Nat Med*, 2007, 13, 95-99.
- P. Bilalis, A. Chatzipavlidis, L.-A. Tziveleka, N. Boukos and G. Kordas, *Journal of Materials Chemistry*, 2012, 22, 13451-13454.
- C. Sanson, O. Diou, J. Thévenot, E. Ibarboure, A. Soum, A. Brûlet, S. Miraux, E. Thiaudière, S. Tan, A. Brisson, V. Dupuis, O. Sandre and S. Lecommandoux, *ACS Nano*, 2011, 5, 1122-1140.
- C. R. Thomas, D. P. Ferris, J.-H. Lee, E. Choi, M. H. Cho, E. S. Kim, J. F. Stoddart, J.-S. Shin, J. Cheon and J. I. Zink, *Journal of the American Chemical Society*, 2010, 132, 10623-10625.
- M. Pernia Leal, A. Torti, A. Riedinger, R. La Fleur, D. Petti, R. Cingolani, R. Bertacco and T. Pellegrino, *ACS Nano*, 2012.
- Y. Namiki, T. Namiki, H. Yoshida, Y. Ishii, A. Tsubota, S. Koido, K. Nariai, M. Mitsunaga, S. Yanagisawa, H. Kashiwagi, Y. Mabashi, Y. Yumoto, S. Hoshina, K. Fujise and N. Tada, *Nat Nano*, 2009, 4, 598-606.
- V. Sokolova and M. Epple, *Angewandte Chemie International Edition*, 2008, 47, 1382-1395.
- R. Di Corato, N. C. Bigall, A. Ragusa, D. Dorfs, A. Genovese, R. Marotta, L. Manna and T. Pellegrino, *ACS Nano*, 2011, 5, 1109-1121.
- E.-Q. Song, J. Hu, C.-Y. Wen, Z.-Q. Tian, X. Yu, Z.-L. Zhang, Y.-B. Shi and D.-W. Pang, *ACS Nano*, 2011, 5, 761-770.
- S. J. Son, J. Reichel, B. He, M. Schuchman and S. B. Lee, *Journal of the American Chemical Society*, 2005, 127, 7316-7317.
- J.-H. Lee, J.-t. Jang, J.-s. Choi, S. H. Moon, S.-h. Noh, J.-w. Kim, J.-G. Kim, I.-S. Kim, K. I. Park and J. Cheon, *Nat Nano*, 2011, 6, 418-422.
- J.-H. Lee, E. S. Kim, M. H. Cho, M. Son, S.-I. Yeon, J.-S. Shin and J. Cheon, *Angewandte Chemie International Edition*, 2010, 49, 5698-5702.
- M. H. Cho, E. J. Lee, M. Son, J.-H. Lee, D. Yoo, J.-w. Kim, S. W. Park, J.-S. Shin and J. Cheon, *Nat Mater*, 2012, advance online publication.
- H. Huang, S. Delikanli, H. Zeng, D. M. Ferkey and A. Pralle, *Nat Nano*, 2010, 5, 602-606.
- D. Yoo, J.-H. Lee, T.-H. Shin and J. Cheon, *Accounts of Chemical Research*, 2011, 44, 863-874.
- Y. Yin and A. P. Alivisatos, *Nature*, 2005, 437, 664-670.
- S. G. Kwon and T. Hyeon, *Accounts of Chemical Research*, 2008, 41, 1696-1709.
- S. Tong, S. Hou, Z. Zheng, J. Zhou and G. Bao, *Nano Letters*, 2010, 10, 4607-4613.
- E. S. Guang Choo, X. Tang, Y. Sheng, B. Shuter and J. Xue, *Journal of Materials Chemistry*, 2011, 21, 2310-2319.
- E. Peng, E. S. G. Choo, P. Chandrasekharan, C.-T. Yang, J. Ding, K.-H. Chuang and J. M. Xue, *Small*, 2012, 8, 3620-3630.
- E. Pösel, H. Kloust, U. Tromsdorf, M. Janschel, C. Hahn, C. Maßlo and H. Weller, *ACS Nano*, 2012, 6, 1619-1624.
- C. Khemtong, C. W. Kessinger, O. Togao, J. Ren, M. Takahashi, A. D. Sherry and G. Jinming, 2009.
- E. S. G. Choo, E. Peng, R. Rajendran, P. Chandrasekharan, C.-T. Yang, J. Ding, K.-H. Chuang and J. Xue, *Advanced Functional Materials*, 2013, 23, 496-505.

44. T. N. Narayanan, B. K. Gupta, S. A. Vithayathil, R. R. Aburto, S. A. Mani, J. Taha-Tijerina, B. Xie, B. A. Kaiparettu, S. V. Torti and P. M. Ajayan, *Advanced Materials*, 2012, 24, 2992-2998.
45. M. A. Phillips, M. L. Gran and N. A. Peppas, *Nano Today*, 2010, 5, 143-159.
46. C. W. Jung and P. Jacobs, *Magnetic resonance imaging*, 1995, 13, 661-674.
47. A. K. Gupta and M. Gupta, *Biomaterials*, 2005, 26, 3995-4021.
48. Y. S. Kang, S. Risbud, J. F. Rabolt and P. Stroeve, *Chemistry of Materials*, 1996, 8, 2209-2211.
49. S. Laurent, D. Forge, M. Port, A. Roch, C. Robic, L. Vander Elst and R. N. Muller, *Chemical Reviews*, 2008, 108, 2064-2110.
50. C. Pereira, A. M. Pereira, C. Fernandes, M. Rocha, R. Mendes, M. P. Fernández-García, A. Guedes, P. B. Tavares, J.-M. Grenèche, J. P. Araújo and C. Freire, *Chemistry of Materials*, 2012, 24, 1496-1504.
51. L. Zeng, W. Ren, J. Zheng, P. Cui and A. Wu, *Physical Chemistry Chemical Physics*, 2012, 14, 2631-2636.
52. G. Wang, X. Zhang, A. Skallberg, Y. Liu, Z. Hu, X. Mei and K. Uvdal, *Nanoscale*, 2014, 6, 2953-2963.
53. C. Ravikumar and R. Bandyopadhyaya, *The Journal of Physical Chemistry C*, 2011, 115, 1380-1387.
54. P. Drake, H.-J. Cho, P.-S. Shih, C.-H. Kao, K.-F. Lee, C.-H. Kuo, X.-Z. Lin and Y.-J. Lin, *Journal of Materials Chemistry*, 2007, 17, 4914-4918.
55. Q. Tian, Q. Wang, K. X. Yao, B. Teng, J. Zhang, S. Yang and Y. Han, *Small*, 2014, 10, 1063-1068.
56. S. Ge, X. Shi, K. Sun, C. Li, C. Uher, J. R. Baker, M. M. Banaszak Holl and B. G. Orr, *The Journal of Physical Chemistry C*, 2009, 113, 13593-13599.
57. X. Sun, C. Zheng, F. Zhang, Y. Yang, G. Wu, A. Yu and N. Guan, *The Journal of Physical Chemistry C*, 2009, 113, 16002-16008.
58. T. J. Daou, G. Pourroy, S. Bégin-Colin, J. M. Grenèche, C. Ulhaq-Bouillet, P. Legaré, P. Bernhardt, C. Leuvrey and G. Rogez, *Chemistry of Materials*, 2006, 18, 4399-4404.
59. M. Zhu, Y. Wang, D. Meng, X. Qin and G. Diao, *The Journal of Physical Chemistry C*, 2012, 116, 16276-16285.
60. H. Cai, X. An, J. Cui, J. Li, S. Wen, K. Li, M. Shen, L. Zheng, G. Zhang and X. Shi, *ACS Applied Materials & Interfaces*, 2013, 5, 1722-1731.
61. H.-M. Fan, J.-B. Yi, Y. Yang, K.-W. Kho, H.-R. Tan, Z.-X. Shen, J. Ding, X.-W. Sun, M. C. Olivo and Y.-P. Feng, *ACS Nano*, 2009, 3, 2798-2808.
62. H. Ni, Y. Ni, Y. Zhou and J. Hong, *Materials Letters*, 2012, 73, 206-208.
63. L. Chen, X. Yang, J. Chen, J. Liu, H. Wu, H. Zhan, C. Liang and M. Wu, *Inorganic Chemistry*, 2010, 49, 8411-8420.
64. L. Xiao, J. Li, D. F. Brougham, E. K. Fox, N. Feliu, A. Bushmelev, A. Schmidt, N. Mertens, F. Kiessling, M. Valldor, B. Fadeel and S. Mathur, *ACS Nano*, 2011, 5, 6315-6324.
65. D. Masih, S. Frank, L. Joachim, R. Nathalie, S. Biplab, K. Werner and W. Heiko, *Journal of Physics D: Applied Physics*, 2012, 45, 195001.
66. Y. Lee, J. Lee, C. J. Bae, J. G. Park, H. J. Noh, J. H. Park and T. Hyeon, *Advanced Functional Materials*, 2005, 15, 503-509.
67. J. Ahmed, T. Ahmad, K. V. Ramanujachary, S. E. Lofland and A. K. Ganguli, *Journal of Colloid and Interface Science*, 2008, 321, 434-441.
68. T. Ahn, J. H. Kim, H.-M. Yang, J. W. Lee and J.-D. Kim, *The Journal of Physical Chemistry C*, 2012, 116, 6069-6076.
69. P. Guardia, A. Riedinger, S. Nitti, G. Pugliese, S. Marras, A. Genovese, M. E. Materia, C. Lefevre, L. Manna and T. Pellegrino, *Journal of Materials Chemistry B*, 2014, 2, 4426-4434.
70. S. Sun, H. Zeng, D. B. Robinson, S. Raoux, P. M. Rice, S. X. Wang and G. Li, *Journal of the American Chemical Society*, 2003, 126, 273-279.
71. S. Sun and H. Zeng, *Journal of the American Chemical Society*, 2002, 124, 8204-8205.
72. R. Mejías, S. Pérez-Yagüe, L. Gutiérrez, L. I. Cabrera, R. Spada, P. Acedo, C. J. Serna, F. J. Lázaro, Á. Villanueva, M. d. P. Morales and D. F. Barber, *Biomaterials*, 2011, 32, 2938-2952.
73. C. Lu, L. R. Bhatt, H. Y. Jun, S. H. Park and K. Y. Chai, *Journal of Materials Chemistry*, 2012, 22, 19806-19811.
74. D. Kim, N. Lee, M. Park, B. H. Kim, K. An and T. Hyeon, *Journal of the American Chemical Society*, 2008, 131, 454-455.
75. J. Park, K. An, Y. Hwang, J.-G. Park, H.-J. Noh, J.-Y. Kim, J.-H. Park, N.-M. Hwang and T. Hyeon, *Nat Mater*, 2004, 3, 891-895.
76. M. Song, Y. Zhang, S. Hu, L. Song, J. Dong, Z. Chen and N. Gu, *Colloids and Surfaces A: Physicochemical and Engineering Aspects*, 2012, 408, 114-121.
77. G. Salas, C. Casado, F. J. Teran, R. Miranda, C. J. Serna and M. P. Morales, *Journal of Materials Chemistry*, 2012, 22, 21065-21075.
78. X. Yang, W. Jiang, L. Liu, B. Chen, S. Wu, D. Sun and F. Li, *Journal of Magnetism and Magnetic Materials*, 2012, 324, 2249-2257.
79. J. Y. Park, M. J. Baek, E. S. Choi, S. Woo, J. H. Kim, T. J. Kim, J. C. Jung, K. S. Chae, Y. Chang and G. H. Lee, *ACS Nano*, 2009, 3, 3663-3669.
80. Z. Li, L. Wei, M. Y. Gao and H. Lei, *Advanced Materials*, 2005, 17, 1001-1005.
81. F. Q. Hu, L. Wei, Z. Zhou, Y. L. Ran, Z. Li and M. Y. Gao, *Advanced Materials*, 2006, 18, 2553-2556.
82. X. Lu, M. Niu, R. Qiao and M. Gao, *The Journal of Physical Chemistry B*, 2008, 112, 14390-14394.
83. S. Xuan, F. Wang, J. M. Y. Lai, K. W. Y. Sham, Y.-X. J. Wang, S.-F. Lee, J. C. Yu, C. H. K. Cheng and K. C.-F. Leung, *ACS Applied Materials & Interfaces*, 2011, 3, 237-244.
84. M. Zhu and G. Diao, *The Journal of Physical Chemistry C*, 2011, 115, 18923-18934.
85. Y. Chen, B. Song, X. Tang, L. Lu and J. Xue, *Journal of Materials Chemistry*, 2012, 22, 17656-17662.
86. F. J. Douglas, D. A. MacLaren and M. Murrie, *RSC Advances*, 2012, 2, 8027-8035.
87. C. Li, R. Wei, Y. Xu, A. Sun and L. Wei, *Nano Res.*, 2014, 7, 1-8.
88. L. Faucher, M. Tremblay, J. Lagueux, Y. Gossuin and M.-A. Fortin, *ACS Applied Materials & Interfaces*, 2012, 4, 4506-4515.
89. Y. Zeng, R. Hao, B. Xing, Y. Hou and Z. Xu, *Chemical Communications*, 2010, 46, 3920-3922.
90. Y. Hou, H. Kondoh, M. Shimojo, E. O. Sako, N. Ozaki, T. Kogure and T. Ohta, *The Journal of Physical Chemistry B*, 2005, 109, 4845-4852.

91. S. Peng, C. Wang, J. Xie and S. Sun, *Journal of the American Chemical Society*, 2006, 128, 10676-10677.
92. X. Teng and H. Yang, *Journal of Materials Chemistry*, 2004, 14, 774-779.
93. T. Hyeon, S. S. Lee, J. Park, Y. Chung and H. B. Na, *Journal of the American Chemical Society*, 2001, 123, 12798-12801.
94. K. Woo, J. Hong, S. Choi, H.-W. Lee, J.-P. Ahn, C. S. Kim and S. W. Lee, *Chemistry of Materials*, 2004, 16, 2814-2818.
95. I. Castellanos-Rubio, M. Insausti, E. Garaio, I. Gil de Muro, F. Plazaola, T. Rojo and L. Lezama, *Nanoscale*, 2014, 6, 7542-7552.
96. J. Park, E. Lee, N.-M. Hwang, M. Kang, S. C. Kim, Y. Hwang, J.-G. Park, H.-J. Noh, J.-Y. Kim, J.-H. Park and T. Hyeon, *Angewandte Chemie International Edition*, 2005, 44, 2872-2877.
97. Z. Zhao, Z. Zhou, J. Bao, Z. Wang, J. Hu, X. Chi, K. Ni, R. Wang, X. Chen, Z. Chen and J. Gao, *Nat Commun*, 2013, 4.
98. Y. C. Cao, *Journal of the American Chemical Society*, 2004, 126, 7456-7457.
99. G. Gao, X. Liu, R. Shi, K. Zhou, Y. Shi, R. Ma, E. Takayama-Muromachi and G. Qiu, *Crystal Growth & Design*, 2010, 10, 2888-2894.
100. L. Li, Y. Yang, J. Ding and J. Xue, *Chemistry of Materials*, 2010, 22, 3183-3191.
101. B. H. Kim, N. Lee, H. Kim, K. An, Y. I. Park, Y. Choi, K. Shin, Y. Lee, S. G. Kwon, H. B. Na, J.-G. Park, T.-Y. Ahn, Y.-W. Kim, W. K. Moon, S. H. Choi and T. Hyeon, *Journal of the American Chemical Society*, 2011, 133, 12624-12631.
102. T. Paik, T. R. Gordon, A. M. Prantner, H. Yun and C. B. Murray, *ACS Nano*, 2013, 7, 2850-2859.
103. Z. Zhou, Z. Zhao, H. Zhang, Z. Wang, X. Chen, R. Wang, Z. Chen and J. Gao, *ACS Nano*, 2014.
104. Y. Yang, X. Liu, Y. Yang, W. Xiao, Z. Li, D. Xue, F. Li and J. Ding, *Journal of Materials Chemistry C*, 2013, 1, 2875-2885.
105. E. Peng, E. S. G. Choo, Y. Sheng and J. M. Xue, *New Journal of Chemistry*, 2013, 37, 2051-2060.
106. K. An, M. Park, J. H. Yu, H. B. Na, N. Lee, J. Park, S. H. Choi, I. C. Song, W. K. Moon and T. Hyeon, *European Journal of Inorganic Chemistry*, 2012, 2012, 2148-2155.
107. J. Cheon, N.-J. Kang, S.-M. Lee, J.-H. Lee, J.-H. Yoon and S. J. Oh, *Journal of the American Chemical Society*, 2004, 126, 1950-1951.
108. T. Wang, X. Wang, D. LaMontagne, Z. Wang, Z. Wang and Y. C. Cao, *Journal of the American Chemical Society*, 2012, 134, 18225-18228.
109. P. Guardia, A. Labarta and X. Batlle, *The Journal of Physical Chemistry C*, 2010, 115, 390-396.
110. B. Wang, B. Wang, P. Wei, X. Wang and W. Lou, *Dalton Transactions*, 2012, 41, 896-899.
111. G. Zhen, B. W. Muir, B. A. Moffat, P. Harbour, K. S. Murray, B. Moubarak, K. Suzuki, I. Madsen, N. Agron-Olshina, L. Waddington, P. Mulvaney and P. G. Hartley, *The Journal of Physical Chemistry C*, 2010, 115, 327-334.
112. C.-H. Ho, C.-P. Tsai, C.-C. Chung, C.-Y. Tsai, F.-R. Chen, H.-J. Lin and C.-H. Lai, *Chemistry of Materials*, 2011, 23, 1753-1760.
113. P. Guardia, N. s. Pérez, A. Labarta and X. Batlle, *Langmuir*, 2009, 26, 5843-5847.
114. L. Zhang, J. Wu, H. Liao, Y. Hou and S. Gao, *Chemical Communications*, 2009, 4378-4380.
115. H. Zhu, S. Zhang, Y.-X. Huang, L. Wu and S. Sun, *Nano Letters*, 2013, 13, 2947-2951.
116. J.-t. Jang, H. Nah, J.-H. Lee, S. H. Moon, M. G. Kim and J. Cheon, *Angewandte Chemie International Edition*, 2009, 48, 1234-1238.
117. H. Gu, B. Xu, J. Rao, R. K. Zheng, X. X. Zhang, K. K. Fung and C. Y. C. Wong, *Journal of Applied Physics*, 2003, 93, 7589-7591.
118. C. Xu, K. Xu, H. Gu, R. Zheng, H. Liu, X. Zhang, Z. Guo and B. Xu, *Journal of the American Chemical Society*, 2004, 126, 9938-9939.
119. M. Chen, J. P. Liu and S. Sun, *Journal of the American Chemical Society*, 2004, 126, 8394-8395.
120. J. Kim, C. Rong, Y. Lee, J. P. Liu and S. Sun, *Chemistry of Materials*, 2008, 20, 7242-7245.
121. G. K. Das and T. T. Y. Tan, *The Journal of Physical Chemistry C*, 2008, 112, 11211-11217.
122. K. Kattel, J. Y. Park, W. Xu, H. G. Kim, E. J. Lee, B. A. Bony, W. C. Heo, J. J. Lee, S. Jin, J. S. Baeck, Y. Chang, T. J. Kim, J. E. Bae, K. S. Chae and G. H. Lee, *ACS Applied Materials & Interfaces*, 2011, 3, 3325-3334.
123. R. Si, Y.-W. Zhang, H.-P. Zhou, L.-D. Sun and C.-H. Yan, *Chemistry of Materials*, 2006, 19, 18-27.
124. J. Paek, C. H. Lee, J. Choi, S.-Y. Choi, A. Kim, J. W. Lee and K. Lee, *Crystal Growth & Design*, 2007, 7, 1378-1380.
125. G. K. Das, B. C. Heng, S.-C. Ng, T. White, J. S. C. Loo, L. D'Silva, P. Padmanabhan, K. K. Bhakoo, S. T. Selvan and T. T. Y. Tan, *Langmuir*, 2010, 26, 8959-8965.
126. W. Xu, B. A. Bony, C. R. Kim, J. S. Baeck, Y. Chang, J. E. Bae, K. S. Chae, T. J. Kim and G. H. Lee, *Sci. Rep.*, 2013, 3.
127. M. Yin and S. O'Brien, *Journal of the American Chemical Society*, 2003, 125, 10180-10181.
128. H. B. Na, J. H. Lee, K. An, Y. I. Park, M. Park, I. S. Lee, D.-H. Nam, S. T. Kim, S.-H. Kim, S.-W. Kim, K.-H. Lim, K.-S. Kim, S.-O. Kim and T. Hyeon, *Angewandte Chemie International Edition*, 2007, 46, 5397-5401.
129. A. Puglisi, S. Mondini, S. Cenedese, A. M. Ferretti, N. Santo and A. Ponti, *Chemistry of Materials*, 2010, 22, 2804-2813.
130. T. D. Schladt, T. Graf and W. Tremel, *Chemistry of Materials*, 2009, 21, 3183-3190.
131. J. Park, E. Kang, C. J. Bae, J.-G. Park, H.-J. Noh, J.-Y. Kim, J.-H. Park, H. M. Park and T. Hyeon, *The Journal of Physical Chemistry B*, 2004, 108, 13594-13598.
132. G. H. Lee, S. H. Huh, J. W. Jeong, B. J. Choi, S. H. Kim and H.-C. Ri, *Journal of the American Chemical Society*, 2002, 124, 12094-12095.
133. W. S. Seo, H. H. Jo, K. Lee, B. Kim, S. J. Oh and J. T. Park, *Angewandte Chemie International Edition*, 2004, 43, 1115-1117.
134. X. Zhong, R. Xie, L. Sun, I. Lieberwirth and W. Knoll, *The Journal of Physical Chemistry B*, 2005, 110, 2-4.
135. F. J. Douglas, D. A. MacLaren, F. Tuna, W. M. Holmes, C. C. Berry and M. Murrie, *Nanoscale*, 2014, 6, 172-176.
136. R. Xing, F. Zhang, J. Xie, M. Aronova, G. Zhang, N. Guo, X. Huang, X. Sun, G. Liu, L. H. Bryant, A. Bhirde, A. Liang, Y. Hou, R. D. Leapman, S. Sun and X. Chen, *Nanoscale*, 2011, 3, 4943-4945.
137. H. Hu, A. Dai, J. Sun, X. Li, F. Gao, L. Wu, Y. Fang, H. Yang, L. An, H. Wu and S. Yang, *Nanoscale*, 2013, 5, 10447-10454.

138. H. Zhang, L. Jing, J. Zeng, Y. Hou, Z. Li and M. Gao, *Nanoscale*, 2014, 6, 5918-5925.
139. Y. Hou, H. Kondoh and T. Ohta, *Journal of Nanoscience and Nanotechnology*, 2009, 9, 202-208.
140. Y. Yu, W. Yang, X. Sun, W. Zhu, X. Z. Li, D. J. Sellmyer and S. Sun, *Nano Letters*, 2014, 14, 2778-2782.
141. M. Chen and D. E. Nikles, *Journal of Applied Physics*, 2002, 91, 8477-8479.
142. J. Yu, C. Yang, J. Li, Y. Ding, L. Zhang, M. Z. Yousaf, J. Lin, R. Pang, L. Wei, L. Xu, F. Sheng, C. Li, G. Li, L. Zhao and Y. Hou, *Advanced Materials*, 2014, 26, 4114-4120.
143. C. Yang, H. Zhao, Y. Hou and D. Ma, *Journal of the American Chemical Society*, 2012, 134, 15814-15821.
144. W. Tang, Z. Zhen, C. Yang, L. Wang, T. Cowger, H. Chen, T. Todd, K. Hekmatyar, Q. Zhao, Y. Hou and J. Xie, *Small*, 2014, 10, 1245-1249.
145. Z. Quan, D. Yang, C. Li, D. Kong, P. Yang, Z. Cheng and J. Lin, *Langmuir*, 2009, 25, 10259-10262.
146. J. Zhu, J. Wu, F. Liu, R. Xing, C. Zhang, C. Yang, H. Yin and Y. Hou, *Nanoscale*, 2013, 5, 9141-9149.
147. K. Cheng, M. Yang, R. Zhang, C. Qin, X. Su and Z. Cheng, *ACS Nano*, 2014, 8, 9884-9896.
148. Y. Sheng and J. Xue, *Journal of Colloid and Interface Science*, 2012, 374, 96-101.
149. Q. Song and Z. J. Zhang, *Journal of the American Chemical Society*, 2012, 134, 10182-10190.
150. Z. Zhou, Y. Sun, J. Shen, J. Wei, C. Yu, B. Kong, W. Liu, H. Yang, S. Yang and W. Wang, *Biomaterials*, 2014, 35, 7470-7478.
151. Q. Tian, J. Hu, Y. Zhu, R. Zou, Z. Chen, S. Yang, R. Li, Q. Su, Y. Han and X. Liu, *Journal of the American Chemical Society*, 2013, 135, 8571-8577.
152. S. Gai, G. Yang, X. Li, C. Li, Y. Dai, F. He and P. Yang, *Dalton Transactions*, 2012, 41, 11716-11724.
153. Y. Hou, R. Qiao, F. Fang, X. Wang, C. Dong, K. Liu, C. Liu, Z. Liu, H. Lei, F. Wang and M. Gao, *ACS Nano*, 2012, 7, 330-338.
154. H. Lian, Y. Dai, D. Yang, Z. Cheng, C. Li, Z. Hou, M. Shang and J. Lin, *Nanoscale*, 2014, 6, 9703-9712.
155. N. J. J. Johnson, W. Oakden, G. J. Stanisz, R. Scott Prosser and F. C. J. M. van Veggel, *Chemistry of Materials*, 2011, 23, 3714-3722.
156. F. Wang, R. Deng and X. Liu, *Nat. Protocols*, 2014, 9, 1634-1644.
157. P. Ramasamy, P. Chandra, S. W. Rhee and J. Kim, *Nanoscale*, 2013, 5, 8711-8717.
158. S. Zheng, W. Chen, D. Tan, J. Zhou, Q. Guo, W. Jiang, C. Xu, X. Liu and J. Qiu, *Nanoscale*, 2014, 6, 5675-5679.
159. W. Xu, K. Kattel, J. Y. Park, Y. Chang, T. J. Kim and G. H. Lee, *Physical Chemistry Chemical Physics*, 2012, 14, 12687-12700.
160. H. Xing, S. Zhang, W. Bu, X. Zheng, L. Wang, Q. Xiao, D. Ni, J. Zhang, L. Zhou, W. Peng, K. Zhao, Y. Hua and J. Shi, *Advanced Materials*, 2014, 26, 3867-3872.
161. M. Norek, E. Kampert, U. Zeidler and J. A. Peters, *Journal of the American Chemical Society*, 2008, 130, 5335-5340.
162. K. Kattel, J. Y. Park, W. Xu, H. G. Kim, E. J. Lee, B. A. Bony, W. C. Heo, S. Jin, J. S. Baeck, Y. Chang, T. J. Kim, J. E. Bae, K. S. Chae and G. H. Lee, *Biomaterials*, 2012, 33, 3254-3261.
163. G. K. Das, Y. Zhang, L. D'Silva, P. Padmanabhan, B. C. Heng, J. S. Chye Loo, S. T. Selvan, K. K. Bhakoo and T. T. Yang Tan, *Chemistry of Materials*, 2011, 23, 2439-2446.
164. R. J. Holmberg, T. Aharen and M. Murugesu, *The Journal of Physical Chemistry Letters*, 2012, 3, 3721-3733.
165. G. K. Das, N. J. J. Johnson, J. Cramen, B. Blasiak, P. Latta, B. Tomanek and F. C. J. M. van Veggel, *The Journal of Physical Chemistry Letters*, 2012, 3, 524-529.
166. J. Zhou, Z. Lu, G. Shan, S. Wang and Y. Liao, *Biomaterials*, 2014, 35, 368-377.
167. B. H. Kim, M. J. Hackett, J. Park and T. Hyeon, *Chemistry of Materials*, 2013, 26, 59-71.
168. J. Fang, P. Chandrasekharan, X.-L. Liu, Y. Yang, Y.-B. Lv, C.-T. Yang and J. Ding, *Biomaterials*, 2014, 35, 1636-1642.
169. M. Cho, R. Sethi, J. S. Ananta narayanan, S. S. Lee, D. N. Benoit, N. Taheri, P. Decuzzi and V. L. Colvin, *Nanoscale*, 2014, 6, 13637-13645.
170. Y.-w. Jun, J.-H. Lee and J. Cheon, *Angewandte Chemie International Edition*, 2008, 47, 5122-5135.
171. J. Park, J. Joo, S. G. Kwon, Y. Jang and T. Hyeon, *Angewandte Chemie International Edition*, 2007, 46, 4630-4660.
172. S. G. Kwon and T. Hyeon, *Small*, 2011, 7, 2685-2702.
173. S. G. Kwon, Y. Piao, J. Park, S. Angappane, Y. Jo, N.-M. Hwang, J.-G. Park and T. Hyeon, *Journal of the American Chemical Society*, 2007, 129, 12571-12584.
174. M. F. Casula, Y.-w. Jun, D. J. Zaziski, E. M. Chan, A. Corrias and A. P. Alivisatos, *Journal of the American Chemical Society*, 2006, 128, 1675-1682.
175. T.-D. Nguyen, *Nanoscale*, 2013, 5, 9455-9482.
176. J. V. I. Timonen, E. T. Seppälä, O. Ikkala and R. H. A. Ras, *Angewandte Chemie International Edition*, 2011, 50, 2080-2084.
177. L. Zhang, R. He and H.-C. Gu, *Applied Surface Science*, 2006, 253, 2611-2617.
178. L. Herojit singh, R. Govindaraj, G. Amarendra and C. S. Sundar, *The Journal of Physical Chemistry C*, 2013, 117, 25042-25051.
179. Z. Xu, C. Shen, Y. Hou, H. Gao and S. Sun, *Chemistry of Materials*, 2009, 21, 1778-1780.
180. V. Georgiadou, C. Kokotidou, B. Le Droumaguet, B. Carbonnier, T. Choli-Papadopoulou and C. Dendrinou-Samara, *Dalton Transactions*, 2014, 43, 6377-6388.
181. A. Quarta, A. Curcio, H. Kakwere and T. Pellegrino, *Nanoscale*, 2012, 4, 3319-3334.
182. C. Boyer, M. R. Whittaker, V. Bulmus, J. Liu and T. P. Davis, *NPG Asia Mater*, 2010, 2, 23-30.
183. C. J. Cheng and W. M. Saltzman, *Nat Nano*, 2012, 7, 346-347.
184. J. Huang, L. Bu, J. Xie, K. Chen, Z. Cheng, X. Li and X. Chen, *ACS Nano*, 2010, 4, 7151-7160.
185. H. Soo Choi, W. Liu, P. Misra, E. Tanaka, J. P. Zimmer, B. Itty Ipe, M. G. Bawendi and J. V. Frangioni, *Nat Biotech*, 2007, 25, 1165-1170.
186. J. Liu, M. Yu, C. Zhou and J. Zheng, *Materials Today*, 2013, 16, 477-486.
187. H. Kobayashi, R. Watanabe and P. L. Choyke, *Theranostics*, 2014, 4, 81-89.
188. O. Veisich, J. W. Gunn and M. Zhang, *Advanced Drug Delivery Reviews*, 2010, 62, 284-304.

189. M. Longmire, P. L. Choyke and H. Kobayashi, *Nanomedicine*, 2008, 3, 703-717.
190. J. V. Jokerst, T. Lobovkina, R. N. Zare and S. S. Gambhir, *Nanomedicine*, 2011, 6, 715-728.
191. A. Albanese, P. S. Tang and W. C. W. Chan, *Annual Review of Biomedical Engineering*, 2012, 14, 1-16.
192. A. Ruiz, Y. Hernandez, C. Cabal, E. Gonzalez, S. Veintemillas-Verdaguer, E. Martinez and M. P. Morales, *Nanoscale*, 2013, 5, 11400-11408.
193. J. Wan, X. Jiang, H. Li and K. Chen, *Journal of Materials Chemistry*, 2012, 22, 13500-13505.
194. K. N. Raymond and V. C. Pierre, *Bioconjugate Chemistry*, 2004, 16, 3-8.
195. J. S. Ananta, B. Godin, R. Sethi, L. Moriggi, X. Liu, R. E. Serda, R. Krishnamurthy, R. Muthupillai, R. D. Bolskar, L. Helm, M. Ferrari, L. J. Wilson and P. Decuzzi, *Nat Nano*, 2010, 5, 815-821.
196. M. L. Viger, J. Sankaranarayanan, C. de Gracia Lux, M. Chan and A. Almutairi, *Journal of the American Chemical Society*, 2013, 135, 7847-7850.
197. N. Lee, Y. Choi, Y. Lee, M. Park, W. K. Moon, S. H. Choi and T. Hyeon, *Nano Letters*, 2012, 12, 3127-3131.
198. R. Qiao, C. Yang and M. Gao, *Journal of Materials Chemistry*, 2009, 19, 6274-6293.
199. Y.-X. J. Wang, *Quantitative Imaging in Medicine and Surgery*, 2011, 1, 35-40.
200. C. Hoskins, Y. Min, M. Gueorgieva, C. McDougall, A. Volovick, P. Prentice, Z. Wang, A. Melzer, A. Cuschieri and L. Wang, *Journal of Nanobiotechnology*, 2012, 10, 27.
201. P. Gillis, F. Moiny and R. A. Brooks, *Magnetic Resonance in Medicine*, 2002, 47, 257-263.
202. Q. L. Vuong, P. Gillis and Y. Gossuin, *Journal of Magnetic Resonance*, 2011, 212, 139-148.
203. Y. Matsumoto and A. Jasanoff, *Magnetic resonance imaging*, 2008, 26, 994-998.
204. U. I. Tromsdorf, N. C. Bigall, M. G. Kaul, O. T. Bruns, M. S. Nikolic, B. Mollwitz, R. A. Sperling, R. Reimer, H. Hohenberg, W. J. Parak, S. Förster, U. Beisiegel, G. Adam and H. Weller, *Nano Letters*, 2007, 7, 2422-2427.
205. M. Li, H. Schnablegger and S. Mann, *Nature*, 1999, 402, 393-395.
206. S. Singamaneni, V. N. Bliznyuk, C. Binek and E. Y. Tsybal, *Journal of Materials Chemistry*, 2011, 21, 16819-16845.
207. L. Zhou, J. Yuan and Y. Wei, *Journal of Materials Chemistry*, 2011, 21, 2823-2840.
208. R. De Palma, S. Peeters, M. J. Van Bael, H. Van den Rul, K. Bonroy, W. Laureyn, J. Mullens, G. Borghs and G. Maes, *Chemistry of Materials*, 2007, 19, 1821-1831.
209. E. D. Smolensky, H.-Y. E. Park, T. S. Berquó and V. C. Pierre, *Contrast Media & Molecular Imaging*, 2011, 6, 189-199.
210. X. Wang, R. D. Tilley and J. J. Watkins, *Langmuir*, 2014, 30, 1514-1521.
211. M. D. Shultz, J. U. Reveles, S. N. Khanna and E. E. Carpenter, *Journal of the American Chemical Society*, 2007, 129, 2482-2487.
212. Y.-w. Jun, Y.-M. Huh, J.-s. Choi, J.-H. Lee, H.-T. Song, KimKim, S. Yoon, K.-S. Kim, J.-S. Shin, J.-S. Suh and J. Cheon, *Journal of the American Chemical Society*, 2005, 127, 5732-5733.
213. M. Liong, H. Shao, J. B. Haun, H. Lee and R. Weissleder, *Advanced Materials*, 2010, 22, 5168-5172.
214. A. Dong, X. Ye, J. Chen, Y. Kang, T. Gordon, J. M. Kikkawa and C. B. Murray, *Journal of the American Chemical Society*, 2010, 133, 998-1006.
215. H. Yang, Z. Tian, J. Wang and S. Yang, *Sensors and Actuators B: Chemical*, 2012, 161, 429-433.
216. H. B. Na, G. Palui, J. T. Rosenberg, X. Ji, S. C. Grant and H. Mattoussi, *ACS Nano*, 2011, 6, 389-399.
217. E. Amstad, T. Gillich, I. Bilecka, M. Textor and E. Reimhult, *Nano Letters*, 2009, 9, 4042-4048.
218. H. Wei, N. Insin, J. Lee, H.-S. Han, J. M. Cordero, W. Liu and M. G. Bawendi, *Nano Letters*, 2011, 12, 22-25.
219. R. Hao, J. Yu, Z. Ge, L. Zhao, F. Sheng, L. Xu, G. Li and Y. Hou, *Nanoscale*, 2013, 5, 11954-11963.
220. M. Hatakeyama, H. Kishi, Y. Kita, K. Imai, K. Nishio, S. Karasawa, Y. Masaie, S. Sakamoto, A. Sandhu, A. Tanimoto, T. Gomi, E. Kohda, M. Abe and H. Handa, *Journal of Materials Chemistry*, 2011, 21, 5959-5966.
221. A. Hofmann, S. Thierbach, A. Semisch, A. Hartwig, M. Taupitz, E. Ruhl and C. Graf, *Journal of Materials Chemistry*, 2010, 20, 7842-7853.
222. A. Lopez-Cruz, C. Barrera, V. L. Calero-DdelC and C. Rinaldi, *Journal of Materials Chemistry*, 2009, 19, 6870-6876.
223. E. K. U. Larsen, T. Nielsen, T. Wittenborn, H. Birkedal, T. Vorup-Jensen, M. H. Jakobsen, L. Østergaard, M. R. Horsman, F. Besenbacher, K. A. Howard and J. Kjems, *ACS Nano*, 2009, 3, 1947-1951.
224. E. Peng, J. Ding and J. M. Xue, *Journal of Materials Chemistry*, 2012, 22, 13832-13840.
225. D. Swern, T. W. Findley and J. T. Scanlan, *Journal of the American Chemical Society*, 1944, 66, 1925-1927.
226. H. Hu, M. Yu, F. Li, Z. Chen, X. Gao, L. Xiong and C. Huang, *Chemistry of Materials*, 2008, 20, 7003-7009.
227. F. Stefanoiu, L. Candy, C. Vaca-Garcia and E. Borredon, *European Journal of Lipid Science and Technology*, 2008, 110, 441-447.
228. L. Candy, C. Vaca-Garcia and E. Borredon, *Journal of the American Oil Chemists' Society*, 2005, 82, 271-277.
229. L. Candy, C. Vaca-Garcia and E. Borredon, *European Journal of Lipid Science and Technology*, 2005, 107, 3-11.
230. J. o. Metzger and U. Biermann, *Lipid / Fett*, 1994, 96, 321-323.
231. A. Behr and H. P. Handwerk, *Lipid / Fett*, 1992, 94, 204-208.
232. W. Bickford, P. Krauczunas and D. Wheeler, *Journal of the American Oil Chemists' Society*, 1942, 19, 23-27.
233. Y. Wang, J. F. Wong, X. Teng, X. Z. Lin and H. Yang, *Nano Letters*, 2003, 3, 1555-1559.
234. R. U. Lemieux and E. V. Rudloff, *Canadian Journal of Chemistry*, 1955, 33, 1701-1709.
235. G. Wang, Q. Peng and Y. Li, *Journal of the American Chemical Society*, 2009, 131, 14200-14201.
236. Z. Chen, H. Chen, H. Hu, M. Yu, F. Li, Q. Zhang, Z. Zhou, T. Yi and C. Huang, *Journal of the American Chemical Society*, 2008, 130, 3023-3029.
237. S.-Y. Lee and M. T. Harris, *Journal of Colloid and Interface Science*, 2006, 293, 401-408.

238. F. Herranz, M. P. Morales, A. G. Roca, M. Desco and J. Ruiz-Cabello, *Chemistry – A European Journal*, 2008, 14, 9126-9130.
239. J.-C. Si, Y. Xing, M.-L. Peng, C. Zhang, N. Buske, C. Chen and Y.-L. Cui, *CrystEngComm*, 2014, 16, 512-516.
240. M. Wang, M.-L. Peng, W. Cheng, Y.-L. Cui and C. Chen, *Journal of Nanoscience and Nanotechnology*, 2011, 11, 3688-3691.
241. H. Hu, C. Zhang, L. An, Y. Yu, H. Yang, J. Sun, H. Wu and S. Yang, *Chemistry – A European Journal*, 2014, 20, 7160-7167.
242. S. K. Basiruddin, A. Saha, N. Pradhan and N. R. Jana, *The Journal of Physical Chemistry C*, 2010, 114, 11009-11017.
243. S. Dixit, M. Das, S. Alwarappan, N. L. Goicochea, M. Howell, S. Mohapatra and S. Mohapatra, *RSC Advances*, 2013, 3, 2727-2735.
244. M. Deng, N. Tu, F. Bai and L. Wang, *Chemistry of Materials*, 2012, 24, 2592-2597.
245. A. Prakash, H. Zhu, C. J. Jones, D. N. Benoit, A. Z. Ellsworth, E. L. Bryant and V. L. Colvin, *ACS Nano*, 2009, 3, 2139-2146.
246. P. Qiu, C. Jensen, N. Charity, R. Towner and C. Mao, *Journal of the American Chemical Society*, 2010, 132, 17724-17732.
247. J. Kim, J. E. Lee, J. Lee, J. H. Yu, B. C. Kim, K. An, Y. Hwang, C.-H. Shin, J.-G. Park, J. Kim and T. Hyeon, *Journal of the American Chemical Society*, 2005, 128, 688-689.
248. Y. Tian, B. Yu, X. Li and K. Li, *Journal of Materials Chemistry*, 2011, 21, 2476-2481.
249. H. Yang, H. Zhou, C. Zhang, X. Li, H. Hu, H. Wu and S. Yang, *Dalton Transactions*, 2011, 40, 3616-3621.
250. Y. Huang, T. Wei, J. Yu, Y. Hou, K. Cai and X.-J. Liang, *Molecular Pharmaceutics*, 2014, 11, 3386-3394.
251. E. D. Smolensky, H.-Y. E. Park, Y. Zhou, G. A. Rolla, M. Marjanska, M. Botta and V. C. Pierre, *Journal of Materials Chemistry B*, 2013, 1, 2818-2828.
252. R. Di Corato, A. Quarta, P. Piacenza, A. Ragusa, A. Figuerola, R. Buonsanti, R. Cingolani, L. Manna and T. Pellegrino, *Journal of Materials Chemistry*, 2008, 18, 1991-1996.
253. E. V. Shtykova, X. Huang, X. Gao, J. C. Dyke, A. L. Schmucker, B. Dragnea, N. Remmes, D. V. Baxter, B. Stein, P. V. Konarev, D. I. Svergun and L. M. Bronstein, *The Journal of Physical Chemistry C*, 2008, 112, 16809-16817.
254. J. Qin, Y. S. Jo and M. Muhammed, *Angewandte Chemie International Edition*, 2009, 48, 7845-7849.
255. M. Gonzales and K. M. Krishnan, *Journal of Magnetism and Magnetic Materials*, 2007, 311, 59-62.
256. C.-A. J. Lin, R. A. Sperling, J. K. Li, T.-Y. Yang, P.-Y. Li, M. Zanella, W. H. Chang and W. J. Parak, *Small*, 2008, 4, 334-341.
257. L. Qi and X. Gao, *ACS Nano*, 2008, 2, 1403-1410.
258. T. Pellegrino, L. Manna, S. Kudera, T. Liedl, D. Koktysh, A. L. Rogach, S. Keller, J. Rädler, G. Natile and W. J. Parak, *Nano Letters*, 2004, 4, 703-707.
259. W. W. Yu, E. Chang, J. C. Falkner, J. Zhang, A. M. Al-Somali, C. M. Sayes, J. Johns, R. Drezek and V. L. Colvin, *Journal of the American Chemical Society*, 2007, 129, 2871-2879.
260. M. Moros, B. Pelaz, P. Lopez-Larrubia, M. L. Garcia-Martin, V. Grazu and J. M. de la Fuente, *Nanoscale*, 2010, 2, 1746-1755.
261. D. P. Acharya, B. A. Moffat, A. Polyzos, L. Waddington, G. Coia, D. K. Wright, H. X. Wang, G. F. Egan, B. W. Muir and P. G. Hartley, *RSC Advances*, 2012, 2, 6655-6662.
262. D. Janczewski, N. Tomczak, Y. W. Khin, M.-Y. Han and G. Julius Vancso, *European Polymer Journal*, 2009, 45, 3-9.
263. D. Janczewski, N. Tomczak, M.-Y. Han and G. J. Vancso, *Nat. Protocols*, 2011, 6, 1546-1553.
264. E. E. Lees, T.-L. Nguyen, A. H. A. Clayton and P. Mulvaney, *ACS Nano*, 2009, 3, 1121-1128.
265. W. Y. William, C. Emmanuel, M. S. Christie, D. Rebekah and L. C. Vicki, *Nanotechnology*, 2006, 17, 4483.
266. L. M. Bronstein, E. V. Shtykova, A. Malyutin, J. C. Dyke, E. Gunn, X. Gao, B. Stein, P. V. Konarev, B. Dragnea and D. I. Svergun, *The Journal of Physical Chemistry C*, 2010, 114, 21900-21907.
267. E. V. Shtykova, A. Malyutin, J. Dyke, B. Stein, P. V. Konarev, B. Dragnea, D. I. Svergun and L. M. Bronstein, *The Journal of Physical Chemistry C*, 2010, 114, 21908-21913.
268. S. Yin, Z. Li, L. Cheng, C. Wang, Y. Liu, Q. Chen, H. Gong, L. Guo, Y. Li and Z. Liu, *Nanoscale*, 2013, 5, 12464-12473.
269. J. Park, M. K. Yu, Y. Y. Jeong, J. W. Kim, K. Lee, V. N. Phan and S. Jon, *Journal of Materials Chemistry*, 2009, 19, 6412-6417.
270. H.-M. Yang, H. J. Lee, K.-S. Jang, C. W. Park, H. W. Yang, W. D. Heo and J.-D. Kim, *Journal of Materials Chemistry*, 2009, 19, 4566-4574.
271. S. Huang, M. Bai and L. Wang, *Sci. Rep.*, 2013, 3.
272. C. Huang, K. G. Neoh, L. Wang, E.-T. Kang and B. Shuter, *Journal of Materials Chemistry*, 2010, 20, 8512-8520.
273. Z. Cheng, S. Liu, H. Gao, W. Tremel, N. Ding, R. Liu, P. W. Beines and W. Knoll, *Macromolecular Chemistry and Physics*, 2008, 209, 1145-1151.
274. H.-M. Yang, C. W. Park, P. K. Bae, T. Ahn, B.-K. Seo, B. H. Chung and J.-D. Kim, *Journal of Materials Chemistry B*, 2013, 1, 3035-3043.
275. J. Yuan, Y. Xu and A. H. E. Muller, *Chemical Society Reviews*, 2011, 40, 640-655.
276. Z. Tang and N. A. Kotov, *Advanced Materials*, 2005, 17, 951-962.
277. C. R. De Silva, S. Smith, I. Shim, J. Pyun, T. Gutu, J. Jiao and Z. Zheng, *Journal of the American Chemical Society*, 2009, 131, 6336-6337.
278. S. E. Bowles, W. Wu, T. Kowalewski, M. C. Schalnath, R. J. Davis, J. E. Pemberton, I. Shim, B. D. Korth and J. Pyun, *Journal of the American Chemical Society*, 2007, 129, 8694-8695.
279. J. Yuan, H. Gao, F. Schacher, Y. Xu, R. Richter, W. Tremel and A. H. E. Müller, *ACS Nano*, 2009, 3, 1441-1450.
280. R. L. Truby, S. Y. Emelianov and K. A. Homan, *Langmuir*, 2013, 29, 2465-2470.
281. M. S. Nikolic, C. Olsson, A. Salcher, A. Kornowski, A. Rank, R. Schubert, A. Frömsdorf, H. Weller and S. Förster, *Angewandte Chemie International Edition*, 2009, 48, 2752-2754.
282. Y. Lee, H. Lee, P. B. Messersmith and T. G. Park, *Macromolecular Rapid Communications*, 2010, 31, 2109-2114.
283. L. J. Hill and J. Pyun, *ACS Applied Materials & Interfaces*, 2014, 6, 6022-6032.
284. Y. Liu, T. C. Hughes, B. W. Muir, L. J. Waddington, T. R. Gengenbach, C. D. Easton, T. M. Hinton, B. A. Moffat, X. Hao and J. Qiu, *Biomaterials*, 2014, 35, 378-386.
285. J. Shen, C. Qin, Y. Hu, N. Li and M. Ye, *Polymer Composites*, 2010, 31, 2035-2041.

286. Y. Shan, K. Chen, X. Yu and L. Gao, *Applied Surface Science*, 2010, 257, 362-366.
287. H. Wu, G. Liu, X. Wang, J. Zhang, Y. Chen, J. Shi, H. Yang, H. Hu and S. Yang, *Acta Biomaterialia*, 2011, 7, 3496-3504.
288. H. Wu, G. Liu, Y. Zhuang, D. Wu, H. Zhang, H. Yang, H. Hu and S. Yang, *Biomaterials*, 2011, 32, 4867-4876.
289. W. Baaziz, X. Liu, I. Florea, S. Begin-Colin, B. P. Pichon, C. Ulhaq, O. Ersen, M. Soria-Sanchez, S. Zafeiratos, I. Janowska, D. Begin and C. Pham-Huu, *Journal of Materials Chemistry A*, 2013, 1, 13853-13861.
290. G. Lamanna, A. Garofalo, G. Popa, C. Wilhelm, S. Begin-Colin, D. Felder-Flesch, A. Bianco, F. Gazeau and C. Menard-Moyon, *Nanoscale*, 2013, 5, 4412-4421.
291. M. Pumera, Z. Sofer and A. Ambrosi, *Journal of Materials Chemistry A*, 2014, 2, 8981-8987.
292. J. L. Gunjekar, I. Y. Kim, J. M. Lee, Y. K. Jo and S.-J. Hwang, *The Journal of Physical Chemistry C*, 2014, 118, 3847-3863.
293. K. Yang, L. Feng, X. Shi and Z. Liu, *Chemical Society Reviews*, 2013, 42, 530-547.
294. D. R. Dreyer, S. Park, C. W. Bielawski and R. S. Ruoff, *Chemical Society Reviews*, 2010, 39, 228-240.
295. T. Liu, C. Wang, X. Gu, H. Gong, L. Cheng, X. Shi, L. Feng, B. Sun and Z. Liu, *Advanced Materials*, 2014, 26, 3433-3440.
296. W. Yin, L. Yan, J. Yu, G. Tian, L. Zhou, X. Zheng, X. Zhang, Y. Yong, J. Li, Z. Gu and Y. Zhao, *ACS Nano*, 2014, 8, 6922-6933.
297. W. Lei, D. Portehault, D. Liu, S. Qin and Y. Chen, *Nat Commun*, 2013, 4, 1777.
298. D. Golberg, Y. Bando, Y. Huang, T. Terao, M. Mitome, C. Tang and C. Zhi, *ACS Nano*, 2010, 4, 2979-2993.
299. C. Chung, Y.-K. Kim, D. Shin, S.-R. Ryoo, B. H. Hong and D.-H. Min, *Accounts of Chemical Research*, 2013, 46, 2211-2224.
300. W. S. Hummers and R. E. Offeman, *Journal of the American Chemical Society*, 1958, 80, 1339-1339.
301. J. Luo, L. J. Cote, V. C. Tung, A. T. L. Tan, P. E. Goins, J. Wu and J. Huang, *Journal of the American Chemical Society*, 2010, 132, 17667-17669.
302. H.-P. Cong, J.-J. He, Y. Lu and S.-H. Yu, *Small*, 2010, 6, 169-173.
303. W. Baaziz, L. Truong-Phuoc, C. Duong-Viet, G. Melinte, I. Janowska, V. Papaefthimiou, O. Ersen, S. Zafeiratos, D. Begin, S. Begin-Colin and C. Pham-Huu, *Journal of Materials Chemistry A*, 2014, 2, 2690-2700.
304. D. W.-P. Pang, F.-W. Yuan, Y.-C. Chang, G.-A. Li and H.-Y. Tuan, *Nanoscale*, 2012, 4, 4562-4570.
305. X. Huo, J. Liu, B. Wang, H. Zhang, Z. Yang, X. She and P. Xi, *Journal of Materials Chemistry A*, 2013, 1, 651-656.
306. Y. Zhang, B. Chen, L. Zhang, J. Huang, F. Chen, Z. Yang, J. Yao and Z. Zhang, *Nanoscale*, 2011, 3, 1446-1450.
307. W. Chen, P. Yi, Y. Zhang, L. Zhang, Z. Deng and Z. Zhang, *ACS Applied Materials & Interfaces*, 2011, 3, 4085-4091.
308. E. Peng, J. Ding and J. M. Xue, *New Journal of Chemistry*, 2014, 38, 2312-2319.
309. H. Zhang, H. Wu, J. Wang, Y. Yang, D. Wu, Y. Zhang, Y. Zhang, Z. Zhou and S. Yang, *Biomaterials*, 2015, 42, 66-77.
310. K. Yang, J. Wan, S. Zhang, Y. Zhang, S.-T. Lee and Z. Liu, *ACS Nano*, 2010, 5, 516-522.
311. X. Sun, Z. Liu, K. Welscher, J. Robinson, A. Goodwin, S. Zaric and H. Dai, *Nano Res.*, 2008, 1, 203-212.
312. W. Hu, C. Peng, W. Luo, M. Lv, X. Li, D. Li, Q. Huang and C. Fan, *ACS Nano*, 2010, 4, 4317-4323.
313. Z. Liu, J. T. Robinson, X. Sun and H. Dai, *Journal of the American Chemical Society*, 2008, 130, 10876-10877.
314. G. Gonçalves, M. Vila, M.-T. Portolés, M. Vallet-Regi, J. Gracio and P. A. A. P. Marques, *Advanced Healthcare Materials*, 2013, 2, 1072-1090.
315. A. B. Seabra, A. J. Paula, R. de Lima, O. L. Alves and N. Durán, *Chemical Research in Toxicology*, 2014, 27, 159-168.
316. J. Kim, L. J. Cote, F. Kim, W. Yuan, K. R. Shull and J. Huang, *Journal of the American Chemical Society*, 2010, 132, 8180-8186.
317. F. Zhang, E. Lees, F. Amin, P. Rivera_Gil, F. Yang, P. Mulvaney and W. J. Parak, *Small*, 2011, 7, 3113-3127.
318. Y. Matsuo, T. Miyabe, T. Fukutsuka and Y. Sugie, *Carbon*, 2007, 45, 1005-1012.
319. K. Yang, S. Liang, L. Zou, L. Huang, C. Park, L. Zhu, J. Fang, Q. Fu and H. Wang, *Langmuir*, 2012, 28, 2904-2908.
320. W. Yu, H. Xie, X. Wang and X. Wang, *Nanoscale Res Lett*, 2010, 6, 1-7.
321. Y. Sheng, X. Tang, E. Peng and J. Xue, *Journal of Materials Chemistry B*, 2013, 1, 512-521.
322. B. J. Hong, O. C. Compton, Z. An, I. Eryazici and S. T. Nguyen, *ACS Nano*, 2011, 6, 63-73.
323. H. Wen, C. Dong, H. Dong, A. Shen, W. Xia, X. Cai, Y. Song, X. Li, Y. Li and D. Shi, *Small*, 2012, 8, 760-769.
324. Y. A. Kabachii, A. S. Golub, S. Y. Kochev, N. D. Lenenko, S. S. Abramchuk, M. Y. Antipin, P. M. Valetsky, B. D. Stein, W. E. Mahmoud, A. A. Al-Ghamdi and L. M. Bronstein, *Chemistry of Materials*, 2013, 25, 2434-2440.
325. B. Jang, M. Park, O. B. Chae, S. Park, Y. Kim, S. M. Oh, Y. Piao and T. Hyeon, *Journal of the American Chemical Society*, 2012, 134, 15010-15015.
326. E. Peng, E. S. G. Choo, C. S. H. Tan, X. Tang, Y. Sheng and J. Xue, *Nanoscale*, 2013, 5, 5994-6005.
327. X. L. Liu, E. S. G. Choo, A. S. Ahmed, L. Y. Zhao, Y. Yang, R. V. Ramanujan, J. M. Xue, D. D. Fan, H. M. Fan and J. Ding, *Journal of Materials Chemistry B*, 2014, 2, 120-128.
328. J. Yuan, E. Peng and J. M. Xue, *Journal of Materials Research*, 2014, 29, 1626-1634.
329. H.-Y. Huang, S.-H. Hu, C.-S. Chian, S.-Y. Chen, H.-Y. Lai and Y.-Y. Chen, *Journal of Materials Chemistry*, 2012, 22, 8566-8573.
330. B.-S. Kim, J.-M. Qiu, J.-P. Wang and T. A. Taton, *Nano Letters*, 2005, 5, 1987-1991.
331. Y. Mai and A. Eisenberg, *Chemical Society Reviews*, 2012, 41, 5969-5985.
332. D. Cheng, G. Hong, W. Wang, R. Yuan, H. Ai, J. Shen, B. Liang, J. Gao and X. Shuai, *Journal of Materials Chemistry*, 2011, 21, 4796-4804.
333. H. Ai, C. Flask, B. Weinberg, X. T. Shuai, M. D. Pagel, D. Farrell, J. Duerk and J. Gao, *Advanced Materials*, 2005, 17, 1949-1952.
334. D. Niu, Z. Zhang, S. Jiang, Z. Ma, X. Liu, Y. Li, L. Zhou, C. Liu, Y. Li and J. Shi, *Journal of Materials Chemistry*, 2012, 22, 24936-24944.
335. J. Du and R. K. O'Reilly, *Soft Matter*, 2009, 5, 3544-3561.

336. R. J. Hickey, A. S. Haynes, J. M. Kikkawa and S.-J. Park, *Journal of the American Chemical Society*, 2011, 133, 1517-1525.
337. Q. Luo, R. J. Hickey and S.-J. Park, *ACS Macro Letters*, 2013, 2, 107-111.
338. R. J. Hickey, J. Koski, X. Meng, R. A. Riggelman, P. Zhang and S.-J. Park, *ACS Nano*, 2013, 8, 495-502.
339. R. J. Hickey, X. Meng, P. Zhang and S.-J. Park, *ACS Nano*, 2013, 7, 5824-5833.
340. R. B. Grubbs, *Nat Mater*, 2007, 6, 553-555.
341. X. L. Liu, Y. T. Wang, C. T. Ng, R. Wang, G. Y. Jing, J. B. Yi, J. Yang, B. H. Bay, L.-Y. L. Yung, D. D. Fan, J. Ding and H. M. Fan, *Advanced Materials Interfaces*, 2014, 1, n/a-n/a.
342. J. Qin, S. Laurent, Y. S. Jo, A. Roch, M. Mikhaylova, Z. M. Bhujwala, R. N. Muller and M. Muhammed, *Advanced Materials*, 2007, 19, 1874-1878.
343. C. Khemtong, O. Togao, J. Ren, C. W. Kessinger, M. Takahashi, A. D. Sherry and J. Gao, *Journal of Magnetic Resonance*, 2011, 209, 53-60.
344. J. Zeng, L. Jing, Y. Hou, M. Jiao, R. Qiao, Q. Jia, C. Liu, F. Fang, H. Lei and M. Gao, *Advanced Materials*, 2014, 26, 2694-2698.
345. L. Wang, Q. Wu, S. Tang, J. Zeng, R. Qiao, P. Zhao, Y. Zhang, F. Hu and M. Gao, *RSC Advances*, 2013, 3, 23454-23460.
346. H. Fengqin, J. Qiaojuan, L. Yilin and G. Mingyuan, *Nanotechnology*, 2011, 22, 245604.
347. J. Yu, R. Hao, F. Sheng, L. Xu, G. Li and Y. Hou, *Nano Res.*, 2012, 5, 679-694.
348. A. Roch, Y. Gossuin, R. N. Muller and P. Gillis, *Journal of Magnetism and Magnetic Materials*, 2005, 293, 532-539.
349. X. Li, H. Li, G. Liu, Z. Deng, S. Wu, P. Li, Z. Xu, H. Xu and P. K. Chu, *Biomaterials*, 2012, 33, 3013-3024.
350. T.-H. Shin, J.-s. Choi, S. Yun, I.-S. Kim, H.-T. Song, Y. Kim, K. I. Park and J. Cheon, *ACS Nano*, 2014, 8, 3393-3401.
351. O. Zurkiya and X. Hu, *Magnetic Resonance in Medicine*, 2006, 56, 726-732.
352. C. Lin, S. Cai and J. Feng, *Journal of Nanomaterials*, 2012, 2012, 9.
353. C. Khemtong, C. W. Kessinger, J. Ren, E. A. Bey, S.-G. Yang, J. S. Guthi, D. A. Boothman, A. D. Sherry and J. Gao, *Cancer Research*, 2009, 69, 1651-1658.
354. G. Zabow, S. Dodd, J. Moreland and A. Koretsky, *Nature*, 2008, 453, 1058-1063.
355. A. C. Kamps, B. L. Sanchez-Gaytan, R. J. Hickey, N. Clarke, M. Fryd and S.-J. Park, *Langmuir*, 2010, 26, 14345-14350.
356. B. L. Sanchez-Gaytan, S. Li, A. C. Kamps, R. J. Hickey, N. Clarke, M. Fryd, B. B. Wayland and S.-J. Park, *The Journal of Physical Chemistry C*, 2011, 115, 7836-7842.
357. Z. Zhou, D. Huang, J. Bao, Q. Chen, G. Liu, Z. Chen, X. Chen and J. Gao, *Advanced Materials*, 2012, 24, 6223-6228.
358. G. Huang, H. Li, J. Chen, Z. Zhao, L. Yang, X. Chi, Z. Chen, X. Wang and J. Gao, *Nanoscale*, 2014.
359. K. H. Bae, Y. B. Kim, Y. Lee, J. Hwang, H. Park and T. G. Park, *Bioconjugate Chemistry*, 2010, 21, 505-512.
360. H. Yang, Y. Zhuang, Y. Sun, A. Dai, X. Shi, D. Wu, F. Li, H. Hu and S. Yang, *Biomaterials*, 2011, 32, 4584-4593.
361. Z. Wang, J. Liu, T. Li, J. Liu and B. Wang, *Journal of Materials Chemistry B*, 2014, 2, 4748-4753.
362. Y. Zhang, G. K. Das, V. Vijayaragavan, Q. C. Xu, P. Padmanabhan, K. K. Bhakoo, S. Tamil Selvan and T. T. Y. Tan, *Nanoscale*, 2014, 6, 12609-12617.
363. F. Hu and Y. S. Zhao, *Nanoscale*, 2012, 4, 6235-6243.
364. Z. Zhou, L. Wang, X. Chi, J. Bao, L. Yang, W. Zhao, Z. Chen, X. Wang, X. Chen and J. Gao, *ACS Nano*, 2013, 7, 3287-3296.
365. X. Wang, Z. Zhou, Z. Wang, Y. Xue, Y. Zeng, J. Gao, L. Zhu, X. Zhang, G. Liu and X. Chen, *Nanoscale*, 2013, 5, 8098-8104.
366. Y. Yan, G. K. Such, A. P. R. Johnston, J. P. Best and F. Caruso, *ACS Nano*, 2012, 6, 3663-3669.
367. C. Fang and M. Zhang, *Journal of Materials Chemistry*, 2009, 19, 6258-6266.
368. X. L. Liu, H. M. Fan, J. B. Yi, Y. Yang, E. S. G. Choo, J. M. Xue, D. D. Fan and J. Ding, *Journal of Materials Chemistry*, 2012, 22, 8235-8244.
369. M. Talelli, C. J. F. Rijcken, T. Lammers, P. R. Seevinck, G. Storm, C. F. van Nostrum and W. E. Hennink, *Langmuir*, 2009, 25, 2060-2067.
370. Y.-M. Huh, Y.-w. Jun, H.-T. Song, S. Kim, J.-s. Choi, J.-H. Lee, S. Yoon, K.-S. Kim, J.-S. Shin, J.-S. Suh and J. Cheon, *Journal of the American Chemical Society*, 2005, 127, 12387-12391.
371. M. Creixell, A. C. Bohórquez, M. Torres-Lugo and C. Rinaldi, *ACS Nano*, 2011, 5, 7124-7129.
372. Y.-H. Li, T. Song, J.-Q. Liu, S.-J. Zhu and J. Chang, *Journal of Materials Chemistry*, 2011, 21, 12520-12528.
373. G. Beaune, B. Dubertret, O. Clément, C. Vayssettes, V. Cabuil and C. Ménager, *Angewandte Chemie International Edition*, 2007, 46, 5421-5424.
374. H. Xu, L. Cheng, C. Wang, X. Ma, Y. Li and Z. Liu, *Biomaterials*, 2011, 32, 9364-9373.
375. R. P. Brinkhuis, F. P. J. T. Rutjes and J. C. M. van Hest, *Polymer Chemistry*, 2011, 2, 1449-1462.
376. H. Goemann and C. Feldmann, *Angewandte Chemie International Edition*, 2010, 49, 1362-1395.
377. B. A. Kairdolf, A. M. Smith, T. H. Stokes, M. D. Wang, A. N. Young and S. Nie, *Annual Review of Analytical Chemistry*, 2013, 6, 143-162.
378. M. Haase and H. Schäfer, *Angewandte Chemie International Edition*, 2011, 50, 5808-5829.
379. *Journal of Drug Delivery*, 2012, 2012.
380. R. Di Corato, P. Piacenza, M. Musarò, R. Buonsanti, P. D. Cozzoli, M. Zambianchi, G. Barbarella, R. Cingolani, L. Manna and T. Pellegrino, *Macromolecular Bioscience*, 2009, 9, 952-958.
381. F. Ye, Å. Barrefelt, H. Asem, M. Abedi-Valugerdi, I. El-Serafi, M. Saghafian, K. Abu-Salah, S. Alrokayan, M. Muhammed and M. Hassan, *Biomaterials*, 2014, 35, 3885-3894.
382. K. Ding, L. Jing, C. Liu, Y. Hou and M. Gao, *Biomaterials*, 2014, 35, 1608-1617.
383. C. Liu, Z. Gao, J. Zeng, Y. Hou, F. Fang, Y. Li, R. Qiao, L. Shen, H. Lei, W. Yang and M. Gao, *ACS Nano*, 2013, 7, 7227-7240.
384. E. Y. Sun, L. Josephson, K. A. Kelly and R. Weissleder, *Bioconjugate Chemistry*, 2005, 17, 109-113.
385. L. Sudheendra, G. K. Das, C. Li, D. Stark, J. Cena, S. Cherry and I. M. Kennedy, *Chemistry of Materials*, 2014, 26, 1881-1888.
386. H. Chen, J. Burnett, F. Zhang, J. Zhang, H. Paholak and D. Sun, *Journal of Materials Chemistry B*, 2014, 2, 757-765.

Journal Name

387. L. Wang, J. Liu, Y. Dai, Q. Yang, Y. Zhang, P. Yang, Z. Cheng, H. Lian, C. Li, Z. Hou, P. a. Ma and J. Lin, *Langmuir*, 2014, 30, 13042-13051.
388. N. Lee and T. Hyeon, *Chemical Society Reviews*, 2012, 41, 2575-2589.
389. Y. Deng, H. Wang, W. Gu, S. Li, N. Xiao, C. Shao, Q. Xu and L. Ye, *Journal of Materials Chemistry B*, 2014, 2, 1521-1529.
390. C. Liu, Y. Hou and M. Gao, *Advanced Materials*, 2014, 26, 6922-6932.
391. B. Fadeel and A. E. Garcia-Bennett, *Advanced Drug Delivery Reviews*, 2010, 62, 362-374.
392. R. Liu, H. Y. Zhang, Z. X. Ji, R. Rallo, T. Xia, C. H. Chang, A. Nel and Y. Cohen, *Nanoscale*, 2013, 5, 5644-5653.
393. J. Bresee, C. M. Bond, R. J. Worthington, C. A. Smith, J. C. Gifford, C. A. Simpson, C. J. Carter, G. Wang, J. Hartman, N. A. Osbaugh, R. K. Shoemaker, C. Melander and D. L. Feldheim, *Journal of the American Chemical Society*, 2014, 136, 5295-5300.
394. D. E. Owens Iii and N. A. Peppas, *International Journal of Pharmaceutics*, 2006, 307, 93-102.